A Thesis submitted to the

University of Colorado

Department of Geological Sciences

in partial fulfillment of the

requirement for the degree of

Master of Science in Geology

2021

High-frequency climate variability in a Greenland ice core during the past 50 thousand years

by

Chloe Brashear

B.A., University of Colorado, 2018

Committee Members:

Dr. Tyler R. Jones

Dr. James W.C. White

Dr. Gifford H. Miller

Dr. Nicole S. Lovenduski

Dr. Robert S. Anderson

ABSTRACT

Stable isotopes of hydrogen and oxygen in polar ice cores provide information about local temperature and atmospheric circulation. We use a multi-taper method (MTM) of spectral analysis on a continuous high-resolution (i.e. mm-scale) Greenland water isotope record, recently recovered from the East Greenland Ice Core Project (EGRIP), to determine how interannual and decadal temperature variability changed throughout the past 50 thousand years. We are specifically interested in trends across the most recent glacial-interglacial transition and across millennial scale Dansgaard-Oeschger (i.e. stadial-interstadial) cycles to elucidate how large temperature changes affect variability around the mean in Greenland. To further understand global relationships in variability, we later make comparisons with mm-scale ice core records from the South Pole (SPC) and the West Antarctic Ice Sheet Divide (WDC). Our results reveal a strong coupling between mean temperature and high-frequency (i.e. 7-15 year) climate variability at EGRIP. On average, the Last Glacial Period (LGP; 11.7-50 ka bp) exhibits 2.5 times greater variability than the Holocene and within the context of the LGP, cold stadial periods are 1.5 times more variable than warm interstadial periods. We provide a plausible mechanism for the trend we observe across Dansgaard-Oeschger (DO) cycles in northeast Greenland: a larger sea ice area coupled with a more variable sea ice front may explain the increased isotopic variability during cold stadial periods. In contrast, neither Antarctic site (SPC or WDC) exhibit changes in high-frequency variability across millennial scale warm phases, known as Antarctic Isotope Maxima (AIM) events, that occur with each DO Event. While elucidating exact forcing mechanisms for observed trends in high-frequency variability is outside the scope of this study, we provide critical benchmarks and reasonable hypotheses to test in future climate modeling research.

TABLE OF CONTENTS

LIST OF ABBREVIATIONS

18O	Oxygen (8 protons, 10 neutrons, mass of 18)
ACC	Antarctic Circumpolar Current
AICC2012	Antarctic Ice Core Chronology 2012
AIM	Antarctic Isotope Maxima
CFA	Continuous Flow Analysis
CRDS	Cavity Ring-Down Mass Spectroscopy
D	Hydrogen (1 proton, 1 neutron, mass of 2)
DO	Dansgaard-Oeschger
EGRIP	East Greenland Ice Core Project
ENSO	El Niño-Southern Oscillation
GICC05	Greenland Ice Core Chronology 2005
GCM	General Circulation Model
INSTAAR	Institute of Arctic and Alpine Research
IRMS	Isotope Ratio Mass Spectrometry
LGM	Last Glacial Maximum
LIS	Laurentide Ice Sheet
LGP	Last Glacial Period
MTM	Multi-taper Method
NAO	North Atlantic Oscillation
NEGIS	North Eastern Greenland Ice Stream
NGRIP	North Greenland Ice Core Project
PDF	Probability Density Function
PSD	Power Spectral Density
SO	Southern Ocean
SPC	South Pole Ice Core
VSMOW	Vienna Standard Mean Ocean Water
WDC	West Antarctic Ice Sheet Divide Ice Core

Chapter 1: INTRODUCTION

In this study, we utilize new, high-resolution ice core records from Greenland and Antarctica to understand past climate variability. Using water isotopes, a proxy for local temperature, we interpret the amplitude of high-frequency signals in the range of interannual to decadal scales. This analysis is made possible by advances in technology that allow for continuous sampling of ice at millimeter-resolution. No other geologic record beyond ice cores allows for this level of sampling resolution extending continuously so far back in time, as much as 50,000 years before present in this study.

In many ways, our work helps elucidate not only the mean temperature history of Greenland and Antarctica, but also the variability around the mean. The latter point, variability around the mean, is actually quite complex, often misrepresented in the literature, and is rarely possible in paleoclimate studies due to a lack of data resolution. Here, we quantify variability at interannual to decadal scales, provide interpretations of our results and ultimately, set the scale for General Circulation Model studies that could elucidate the climatological drivers of the patterns we document.

1.1. Importance of Ice Cores

Paleoclimate proxies are derived from preserved geologic materials, such as rock or ice, that can be correlated with various past and present environmental parameters. This information allows scientists to understand climate prior to modern measurements and more importantly, before anthropogenic activity perturbed existing climate cycles. Common proxy indicators can be found in lake and ocean sediment cores, tree rings and coral reefs, but ice cores are unmatched in their ability to provide high detail reconstructions of paleoclimate conditions.

Polar ice sheets form layer by layer through continuous accumulation and compression of snowfall into glacial ice, effectively trapping and stratifying anything from dust particles to air bubbles. Regions of these ice sheets can grow to be several kilometers thick, creating multi-thousand-year archives of past atmospheric composition, temperature, tephra from volcanoes and more. Collectively, these variables and their behavior through time help illustrate the most accurate representation of global climate before anthropogenic interference. Deep ice core drilling is required to collect these archives and various analytical methods are used to obtain the invaluable climate information. For the purposes of this study, we discuss techniques used in meteoric water isotope analysis of polar ice cores and the importance of this science.

1.2. Water Isotopes

Together, hydrogen (H) and oxygen (O) create water. The actual composition of a water sample is more complicated because both H and O have several isotopes, or varieties of the same element differing in number of neutrons and thus, mass. Some stable isotopes of hydrogen and oxygen include ^{1}H, ^{2}H or "D", ^{16}O, ^{17}O, and ^{18}O (note: ^{17}O will not be used in this study and can be ignored). There are other isotopes that we do not consider, including those that are unstable and decay to other forms. Water molecules exist in various isotopologues, or combinations of naturally occurring isotopes. The most abundant of these is $^{1}H_2{}^{16}O$ (99.73098%), while $^{1}H_2{}^{18}O$ and $^{1}HD^{16}O$ exist in much lesser quantities (0.199978% and 0.031460% respectively) (Galewsky, 2016). These isotopologues are critical to climate science because they behave differently within the water cycle and can be used to interpret global hydrologic patterns through a mass dependent process known as isotopic fractionation (Dansgaard, 1964). This phenomenon describes the ordered movement of isotopologues during phase change and is best explained by comparison of molecular bond strengths.

1.3. Isotopic Fractionation

Energy of a molecule is constituted by several components including electronic, translational, rotational and vibrational energies. The last three of these, and primarily vibrational energy, supply modes of motion (i.e. kinetic energy) for molecular systems. In brief, this motion is inherently linked to bond strength and consequently drives differences in chemical behavior among isotopes of the same element. Vibrational energy, unlike translational and rotational, can be described using a quantum spring analogy, where the potential energy of a diatomic molecule is a function of its interatomic distance. Specifically, more massive isotopes (e.g. D or ^{18}O) possess lower vibrational energy than their less massive counterparts (e.g. ^{1}H or ^{16}O) and are therefore able to exist closer together when bonded in a molecule. This reduced interatomic distance among heavier isotopologues results in elevated potential energy which, in turn, produces stronger bonds between atoms. In other words, bonds involving more massive isotopes will be stronger and more ordered. Therefore, water molecules containing heavy isotopes are much harder to break and naturally prefer to exist in denser, lower energy states (e.g. liquid state

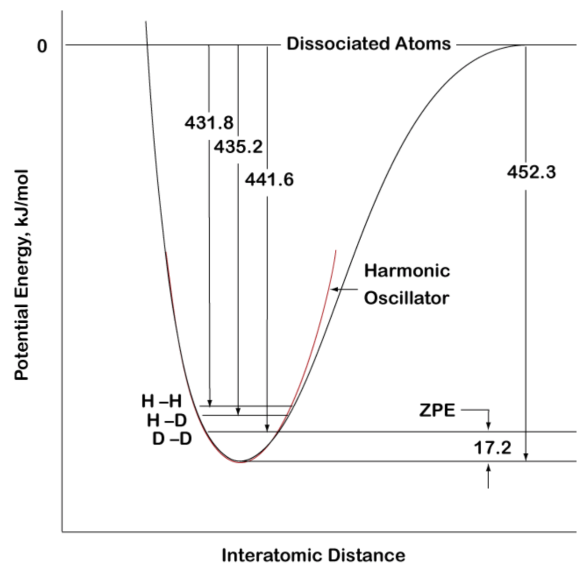

Figure 1.1: Energy diagram from molecular hydrogen; heavier isotopes of H_2 have greater potential energy due to lower interatomic distance (White, 2013)

preferred to a gaseous one) (Kendall & Caldwell, 1998). It is this quantum behavior that drives fractionation during phase change and produces observable patterns within the hydrologic cycle.

Two processes, evaporation and condensation, primarily dictate how water isotopes are fractionated within the hydrologic cycle. Fast, unidirectional processes, such as evaporation, are referred to as *kinetic* reactions because they are governed by the relative velocities at which reactants move. During kinetic fractionation, molecules with higher kinetic energy (i.e. less massive molecules) react more quickly and become physically separated from reactants. In terms of evaporation, gaseous water becomes physically separated from liquid water (Kendall & Caldwell, 1998), and light isotopologues preferentially, but not exclusively, concentrate in the less dense (i.e. gaseous) product pool (Galewsky, 2016).

Reversible processes, such as condensation, allow reactants and products to equilibrate and are thus referred to as *equilibrium* reactions. During equilibrium fractionation, forward and back reactions cause a constant redistribution of isotopes of the same element among various chemical species, and total energy of the system is minimized by the formation of stable bonds. In terms of condensation, heavy isotopes preferentially, but not exclusively, gravitate towards water molecules with stronger bonds and typically accumulate in the denser (i.e. liquid) material (White, 2013; Kendall & Caldwell, 1998).

Putting these ideas together, we can build a general framework for how water isotopes are fractionated within the hydrologic cycle. Evaporation occurs anywhere water is present and causes all atmospheric air to contain some subsaturated level of water vapor. Due to kinetic fractionation during evaporation, water vapor in the air will be isotopically lighter than the liquid surface water it came from. Cloud formation occurs when water vapor reaches saturation and condenses into visible water droplets. Because lower atmospheric temperatures have a decreased capacity for water vapor, saturation is typically achieved through convection, the tendency for warm (i.e. less dense) material to rise and cool (i.e. become more dense). Generally speaking, cloud formation occurs in equatorial regions where convection is strong due to consistent evaporation from the ocean and strong heating of the lower atmosphere via direct solar radiation. As saturation takes place, equilibrium fractionation preferentially transfers heavy isotopologues to a liquid water state. When enough condensate accumulates in the cloud, precipitation removes the isotopically heavy water from the system and ultimately causes the cloud and its subsequent condensate to become isotopically lighter and lighter as it travels away from its point of formation (Galewsky, 2016). This framework can be modeled by Raleigh Distillation discussed in section 1.5.

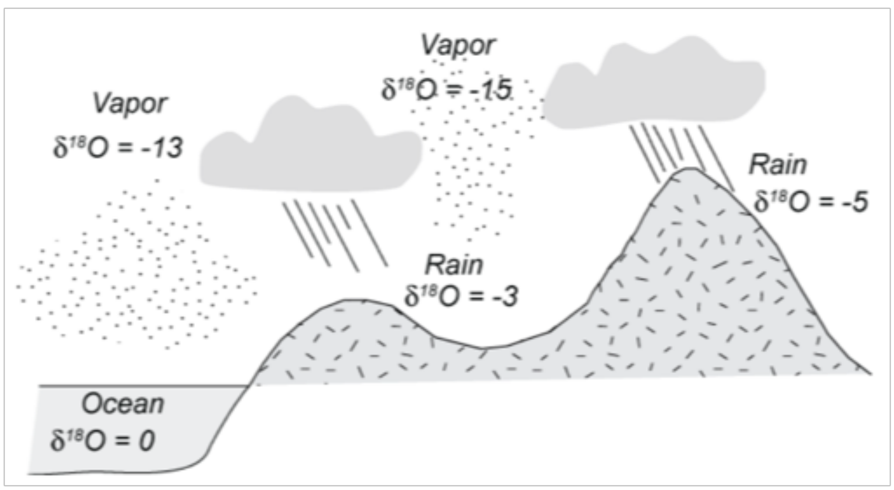

Figure 1.2: Simple visualization of fractionation effects on water isotope composition during the hydrologic cycle; Water isotopes fractionate during both evaporation and condensation causing clouds to become isotopically depleted the further they travel from the point of formation

1.4. Delta Notation

It is important to understand how isotopic fractionation is scientifically quantified using delta notation (δ). Due to the rarity of D and ^{18}O in nature, this method compares the ratio of heavy to light isotopes in a sample to that of a standard. Vienna Standard Mean Ocean Water

(VSMOW) is a common standard used in analysis of meteoric water and is defined as having an isotopic composition of 0 per mil:

$$\delta = \left[\left(\frac{R_{\text{sample}}}{R_{\text{standard}}}\right) - 1\right] \times 1000 \tag{1}$$

This comparison effectively quantifies, in per mil (i.e. parts per thousand), the relative depletion of heavy isotopes in some given water sample from that of the standard (Dansgaard, 1964). For the purposes of this study, we will use the following equations:

$$\delta D = \left[\left(\frac{D/^{1}H_{\text{sample}}}{D/^{1}H_{\text{VSMOW}}}\right) - 1\right] \times 1000 \tag{2}$$

$$\delta^{18}O = \left[\left(\frac{^{18}O/^{16}O_{sample}}{^{18}O/^{16}O_{VSMOW}}\right) - 1\right] \times 1000 \tag{3}$$

Samples with lower, more negative δ values contain fewer heavy isotopes and are said to be "depleted". Samples with higher, less negative δ values contain more heavy isotopes and are referred to as "enriched" (Galewsky, 2016). For example, a δD value of -300 per mil means the water sample is depleted in D by 300 parts per thousand compared to VSMOW.

1.5. Rayleigh Distillation

While fractionation describes the partitioning of heavy from light isotopes during phase change, Raleigh Distillation models the progressive isotopic depletion of clouds during condensation and precipitation under idealized conditions (i.e. cooling always proceeds condensate formation and that condensate is irreversibly removed upon formation). Along the path of this idealized air parcel, the ratio of heavy to light isotopes can be described by:

$$d \ln R_r = (\alpha_v^l(T) - 1) d \ln q \tag{4}$$

where R_r represents the isotopic composition of the vapor mass, $\alpha_v^l(T)$ is the temperature dependent fractionation factor and q is the water vapor mixing ratio (Galewsky, 2016). This equation can be integrated to:

$$R_r = R_0 f^{\alpha_v^l(T)-1} \quad (5)$$

where R_0 represents the initial isotopic composition of the vapor mass and f is the fraction of original vapor remaining (Gat, 1996). Figure 1.3 illustrates the Raleigh framework applied to a cooling vapor rich air parcel with $\delta^{18}O$ = -10‰ and T = 25°C, conditions typical of fresh ocean evaporation. The difference between the vapor (black line) and condensate (grey line) is a result of isotopic fractionation enriching the condensate pool by approximately 10‰. This relationship moves in lockstep until T = 0°C when precipitation changes from rainfall to snowfall. This shift increases the fractionation factor which leads to a temporary enrichment of the condensate pool, and subsequent rapid depletion of the vapor pool as temperature continues to cool. Using this model, the isotopic composition of a meteoric water sample is largely a product of each fractionation event that occurred during that cloud's movement within the hydrologic cycle *and* the average atmospheric temperature along that path. While all polar precipitation does not originate from waters of the same temperature or the same location, this model is sufficient in interpreting most observations (Dansgaard, 1964).

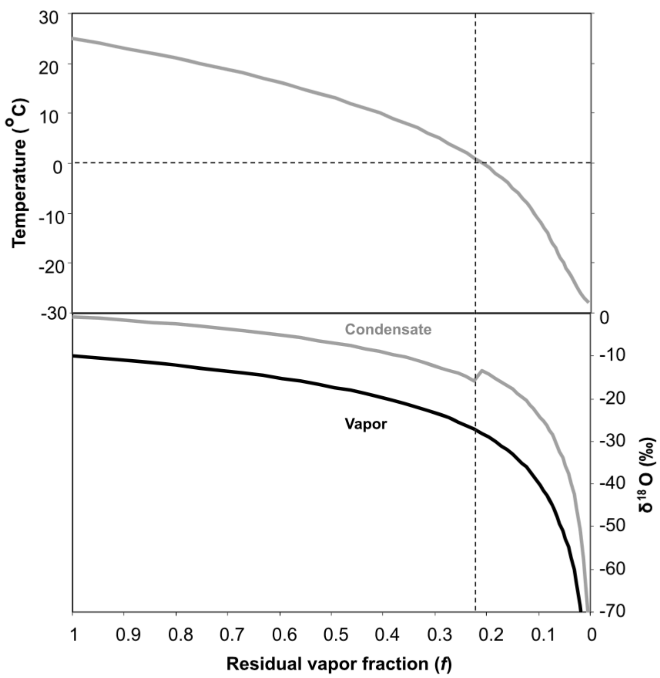

Figure 1.3: Raleigh model with initial isotopic vapor composition set to -10 ‰ and T = 25 °C

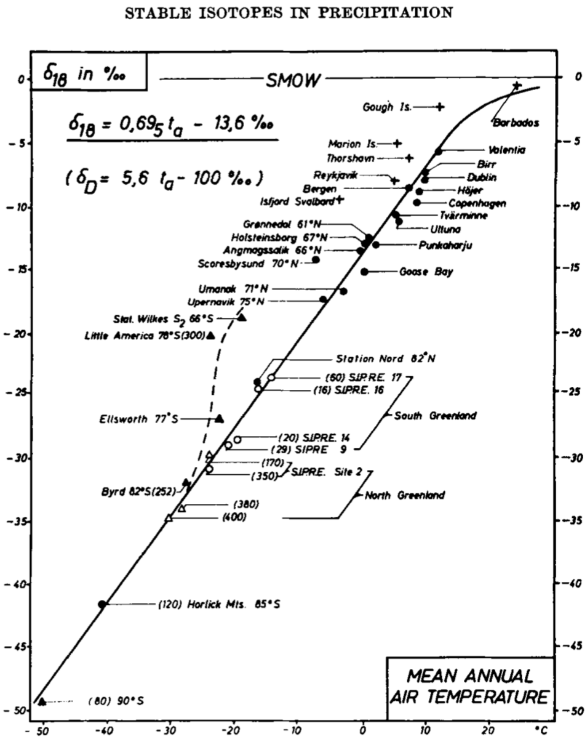

Figure 1.4: Linear relationship between mean annual temperature and mean annual isotope composition of precipitation (Dansgaard, 1964)

1.6. δ^{18}O and δD

It is important to note that the isotopic composition of an individual precipitation sample cannot directly measure condensation temperature because several real-world parameters (e.g. initial composition, thermodynamic conditions during cooling, etc.) are not modeled under Raleigh conditions. Despite this, a tight linear correlation does exist between mean annual surface air temperature and mean annual isotope composition of precipitation (δ^{18}O or δD) in mid and high latitude regions (Dansgaard, 1964). This relationship is especially well observed in Greenland and Antarctica and allows annual to millennial first order temperature to be inferred from polar ice cores (Jouzel et. al, 1997). In Greenland specifically, mean annual isotope composition of precipitation has been empirically defined as:

$$\delta D = 5.6\ T_a - 100‰ \tag{6}$$

$$\delta^{18}O = 0.69\ T_a - 13.6‰ \tag{7}$$

where T_a is the mean annual temperature at the data collection site (Dansgaard, 1964).

Because polar ice sheets very rarely experience surface melt events, any precipitation that lands in these locations is preserved and stratified. Ice cores drilled atop ice sheet domes and summits therefore offer relatively undeformed layers of precipitation which can be sampled to produce multi-thousand-year water isotope ($\delta^{18}O$ or δD) signals throughout modern geologic history. By interpreting these signals as relative temperature, we can begin to understand natural climate variability prior to modern measurements.

1.7. Climate Signals

Earth's climate system, in its entirety, is constituted by a continuum of climate signals which operate at unique frequencies and are driven by a multitude of different factors. Some signals, especially those in the high-frequency range, are easier to comprehend because they operate on timeframes that humans can experience and identify with. One such example is the annual signal, characterized by a seasonal rise and fall of temperature at mid and high latitudes and forced by Earth's 23.5° axial tilt and the disproportionate hemispheric heating it causes during orbit. In mathematical terms, the annual signal can be described as having a period of one year and a frequency of one occurrence per year.

At the opposing end of the spectrum, some signals are so low frequency that we, humans, cannot experience them in a lifetime. One such example is the long term glacial-interglacial signal driven by Earth's three major orbital movements, known as Milankovitch cycles. These include eccentricity (the shape of Earth's orbit: 100,000-year cycles), obliquity (axial tilt: 41,00-year cycles) and precession (direction of Earth's axis: 26,000-year cycles). Together, these cycles significantly affect the amount of incoming solar radiation that reaches Earth, causing variations of up to 25% (Buis, 2020). Ice core records provide strong evidence that Milankovitch cycles have triggered the start and end of glacial periods throughout the last ~800,000 years. This glacial-interglacial signal is evident in the raw water isotope signals of the oldest continuous ice cores (e.g. Vostok, Dome C)

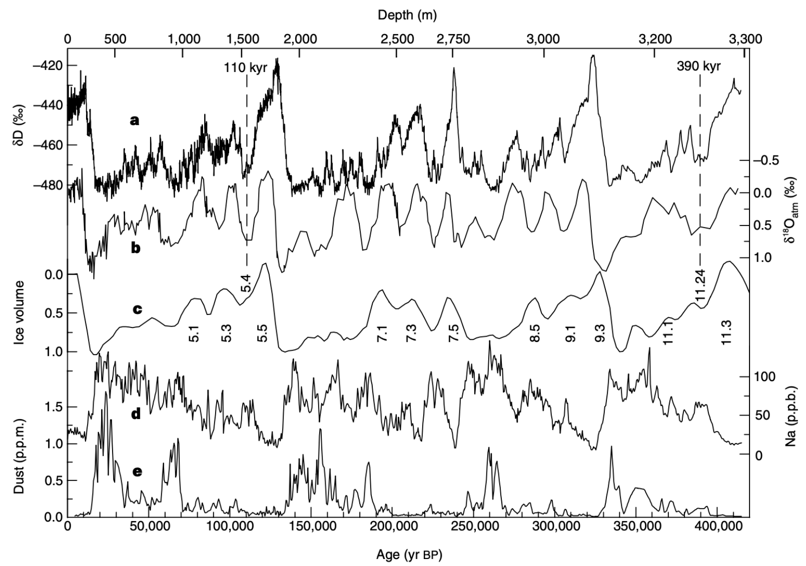

Figure 1.5: Water isotope record from Vostok ice core containing evidence of 100,000 year glacial-interglacial cycles (Petit et al., 1999)

and can be described as having period of ~100,000 years and a frequency of ~1/100,000 occurrence per year (Petit et al., 1999).

Both the annual and glacial-interglacial signals are driven primarily by *external* forcing (i.e. agents which affect climate but exist outside the climate system itself) and have been explained by Earth's orbital configuration. Between these two extreme examples exist a continuum of climate signals which are driven by a combination of *external* and *internal* forcing (i.e. agents which exist within the climate system). These signals operate on interannual, decadal, centennial and millennial cycles and can also be recorded by water isotopes in precipitation at the poles.

A significant millennial scale climate signal recorded by Greenland ice cores is the abrupt alternation between stadials (i.e. cold periods) and interstadials (i.e. warm periods), also known as Dansgaard-Oeschger (DO) Cycles, during the Last Glacial Period (LGP). This cycle is characterized by the rapid onset of a warm quasi-stable climate state, ranging from hundreds to thousands of years, and followed by a less abrupt return to baseline glacial conditions (Wolff et al., 2010). Some have argued that the stadial-interstadial cycle operates on a periodicity of 1,500 years, (Grootes & Stuiver, 1997; Schulz, 2002) although others are not convinced (Ditlevsen et al., 2007).

Further ice core evidence shows that interstadials in the northern hemisphere are in antiphase with less prominent warm periods, known as Antarctic Isotope Maxima (AIM) events, in the southern hemisphere. AIM events are characterized by gradual climatic warming that peaks approximately 200 years after the onset of abrupt DO warming, suggesting an interhemispheric redistribution of heat through the ocean during the LGP (Buizert, et al., 2015b; Blunier et al., 2001). To date the most widely accepted explanation for this phenomenon, known as the "bi-polar see saw", is a millennial scale bi-stability (i.e. fluctuation from strong to weak state) in Atlantic Meridional Overturning Circulation (AMOC). While the exact driver of this bi-stability is still contended, some suggested *internal* drivers include freshwater discharge from the Greenland ice sheet (Bond et al., 1999), increased rain in the North Atlantic (Eisenman et al., 2009), changing ice sheet mass (Zhang et al., 2014), atmospheric CO2 forcing (Zhang et al., 2017) and more.

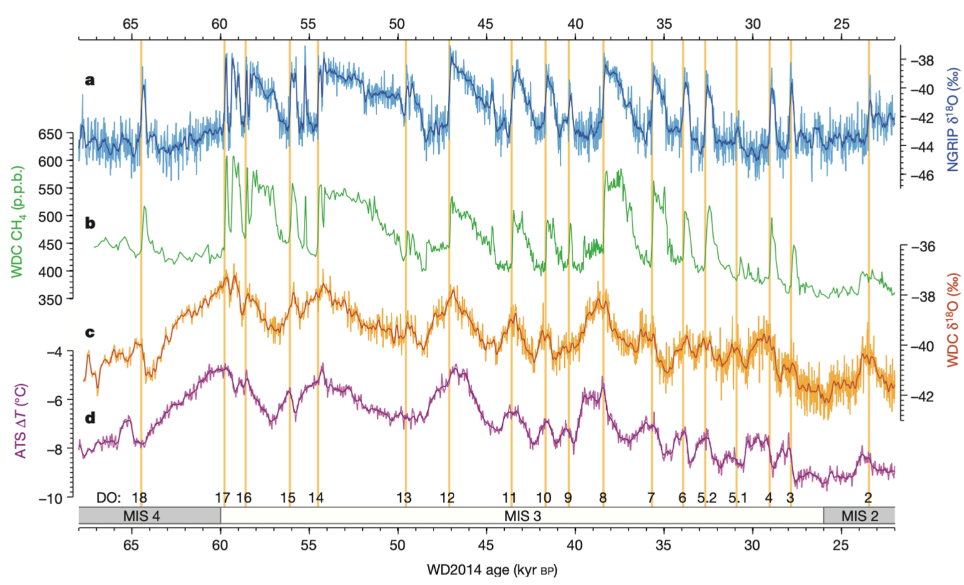

Figure 1.6: Ice core evidence from WDC and NGRIP of antiphase between DO events in the northern hemisphere and AIM events in the southern hemisphere (Buizert et al., 2015b)

Depending on a variety of factors, such as adequate ice core depth, local precipitation accumulation and sampling resolution, the continuum of climate signals can be preserved to varying degrees in water isotope signals of ice cores and examined via spectral analysis (discussed in section 1.10). In this study, we are able to analyze high-frequency climate signals, namely those in the interannual and decadal range, at our study sites well into the LGP. We are especially interested in how the strength (i.e. amplitude) of these high-frequency signals evolved over the course of larger scale, lower-frequency climate cycles, such as glacial-interglacial periods and stadial-interstadial periods in Greenland. The temporal evolution of decadal scale amplitudes can be different than that of millennial scale amplitudes, since these wavelengths can be forced by different climate dynamics, both *internal* and *external*. This notion of the "strength" of high-frequency climate cycles is central to our investigations yet has only recently begun being studied (Jones, 2018; Hughes et al., 2020) due to limitation in water isotope sampling technology.

Climate signals of all scales operate on relatively consistent cycles, as discussed above, but can differ in amplitude over time. What we mean specifically is that climate signals, especially those in the higher frequency range, exist through various large-scale climate states, with differing mean temperature conditions, and variation from the mean state can vary greatly due to a number of internal forcing mechanisms (see Figure 1.7). In this study, we interpret those changes in strength as long term "climate variability". Currently, there exists a substantial knowledge gap in this field and obtaining location specific records of high-frequency climate variability will be invaluable in elucidating drivers of global climate on all scales.

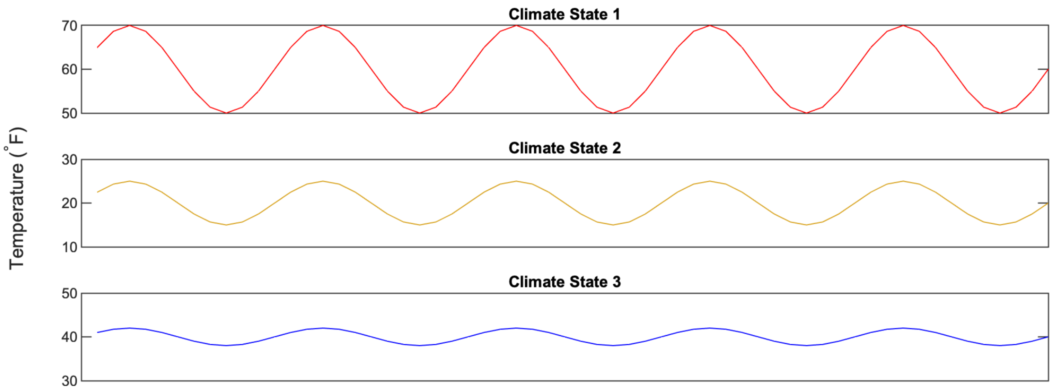

Figure 1.7: Visualization of a synthetic annual signal during three different climate states; By our definition, climate variability is strongest in climate state 1 and weakest in climate state 3

1.8. Site Descriptions

1.8.1. Greenland

This study utilizes the EGRIP (East Greenland Ice Core Project) and NGRIP (North Greenland Ice Core Project) water isotope records to delineate the evolution of high-frequency climate signals in the *northern* hemisphere throughout the past ~50,000 years. We aim to understand how climate variability changed, if at all, from the Last Glacial Period (LGP) to the Holocene and are also interested in smaller scale LGP events, such as stadial-interstadial transitions. The high-resolution (mm-scale sampling) EGRIP water isotope record coupled with spectral analysis techniques used in this study will offer new insights and circumvent limitations that have arisen with earlier Greenlandic water isotope records. The lower resolution (cm-scale resolution) NGRIP record will mainly be used to compare and verify general trends.

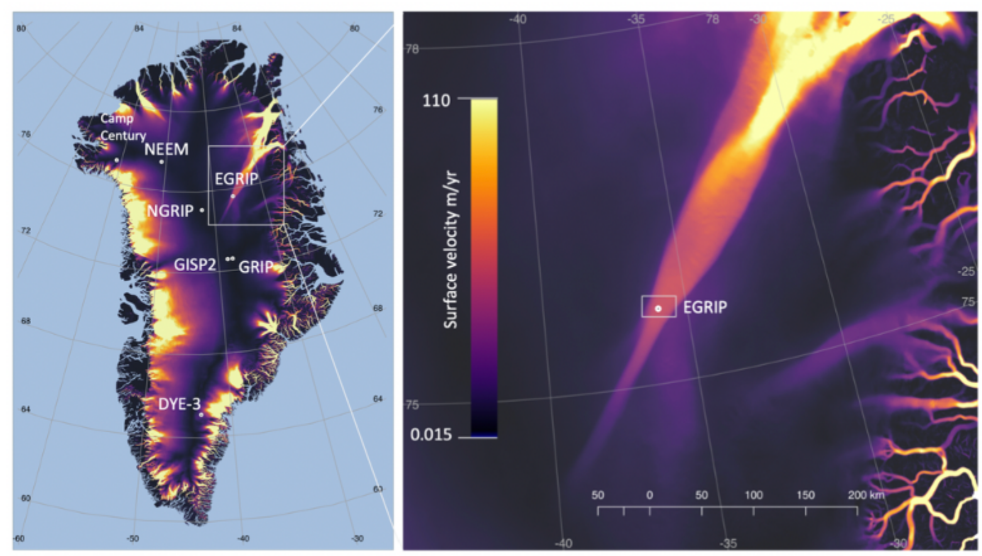

Figure 1.8: Location of EGRIP and NGRIP in relation to other Greenland ice core drilling sites; (Mojtabavi et al., 2019); IS is located on a fast moving ice stream while NGRIP is located at the ice sheet divide.

Drilling of the NGRIP ice core began in 1999 and reached bedrock in 2003. This core was drilled on a plateau of stable ice near the center of Greenland (75° 1´ N and 42° 32´ W) and resulted in a relatively undisturbed core extending 120 ka through the last ice age. Drilling of the more recent EGRIP (75° 38´ N and 35° 60´ W) ice core began in 2016 and is expected to conclude the summer of 2022. The main objective of this core is to better understand ice flow dynamics of the North East Greenland Ice Stream (NEGIS), but it will also provide various climate archives, one being a water isotope record, dating back at least halfway through the last glacial period (i.e. 50 ka BP) and likely further (Mojtabavi et al., 2019). Already, as of the writing of this thesis, data to 50 ka for EGRIP is available for climate analysis. Data obtained from both EGRIP and NGRIP serves to represent central Greenland paleoclimate dynamics. More broadly, this data can be used to better understand Arctic paleoclimate dynamics.

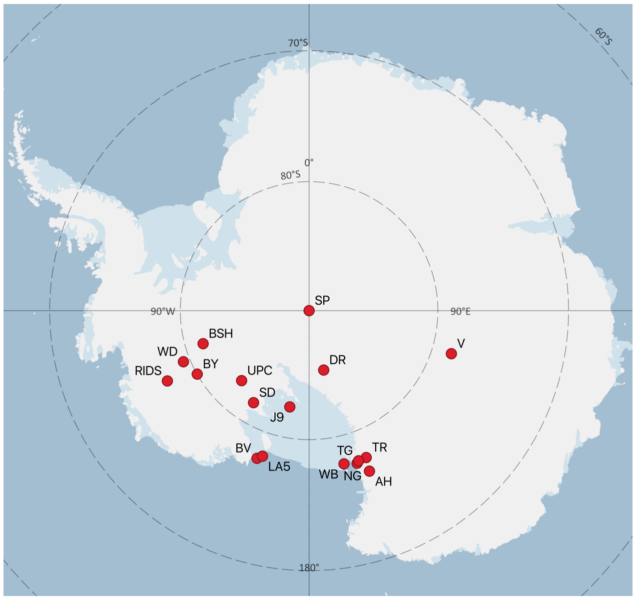

Figure 1.9: Location of West Antarctic Ice Sheet Divide Core (WD) and South Pole Core (SP) in relation to other ice core drilling sites (icecores.org)

1.8.2. Antarctica

This study also utilizes the SPC (South Pole Ice Core Project) and WDC (West Antarctic Ice Sheet Divide Ice Core) high-resolution (mm-scale sampling) water isotope records to delineate the evolution of high-frequency climate signals in the *southern* hemisphere throughout the same time frame (0-50 ka bp). We are similarly interested in how climate variability shifted from the LGP to the Holocene and across warm and cold periods in the LGP that alternate on millennial timeframes, known as Antarctic Isotope Maxima (AIM) events.

Drilling of the WDC (79° 48′ S and 112° 11′ W) ice core ran from 2006 to 2011 atop the West Antarctic Sheet Divide. This divide separates ice that flows to the Ross Sea from ice that flows towards the Weddell Sea and is known for its high annual precipitation rate (~16 cm yr^{-1}) (Fudge et al., 2017). Consequently, a key characteristic of the WDC core is its thick annual layers which have been used to inform high-resolution paleoclimate reconstructions (Buizert et al., 2015a). Due to its proximity to the Pacific Basin, WDC data can be used to extrapolate tropical Pacific paleoclimate dynamics (Jones et al, 2018).

SPC, the most recent U.S. funded deep ice core, was drilled between 2014 and 2016 at the southernmost point of our planet and is the only core drilled above 80° S that extends into the last glacial period. Although East Antarctica generally receives very little accumulation on an annual basis, the drilling site of SPC receives an uncharacteristic 8 cm of precipitation a year (Winski et al., 2018). These conditions provide a unique opportunity to understand high-frequency paleoclimate variability at the East Antarctica interior.

1.9. Ice Core Chronologies

In order to accurately contextualize climate events through time, ice core age-depth scales must be created and calibrated against existing chronologies. In the northern hemisphere, the GICC05 (Greenland Ice Core Chronology 2005), developed by Denmark's Centre for Ice and Climate, serves as a framework and reference for most recent ice core chronologies created in the last few decades, including EGRIP and NGRIP. Sections of GICC05 were derived by counting annual layers in the water isotopes (0-7.9 ka bp), chemical impurities (7.9-42 ka pb), electrical conductivity (7.9-60 ka bp) and/or visual stratigraphy (7.9-60 ka bp) records of DYE-3, GRIP and NGRIP (Svensson et al., 2008). The quality of these data sets varies with depth which is why different methods are used for certain sections of ice. The primary mode of transferring GICC05 to other Greenlandic ice cores is identification of tie points. Usually, tie points are of volcanic origin and can be found through common patterns of elevated peaks in electrical conductivity records. GICC05 was initially transferred to EGRIP by identifying 373 tie points from both NGRIP and NEEM and allowed the EGRIP age-depth scale to extend back 14.96 ka bp (Mojtabavi et al., 2019). An additional 155 tie points, although sparser, have recently been added to the EGRIP chronology, pushing this scale back to approximately 50 ka bp.

Chronologies among Antarctic ice cores have historically been less synchronized primarily due to significant variance in climate and accumulation across the continent. For instance, the AICC2012 (Antarctic Ice Core Chronology 2012) was only recently developed to address inconsistencies of up to several thousand years existing between independent eastern Antarctic chronologies (i.e. Vostok, EDC, EDML, and TALDICE) (Veres et al., 2013). The SPC and WDC sites are similar enough in accumulation levels that they have been synchronized using the WD2014 chronology. This scale was developed by counting annual layers in WDC chemical impurity and electrical conductivity records (Sigl et al., 2016) to 31 ka and by methane synchronization techniques for ages greater than 31 ka (Buizert et al., 2015a). It was transferred to SPC via 251 volcanic tie points (Winksi et al., 2019).

1.10. Spectral analysis

Chronologies allow ice core data sets to be analyzed via spectral analysis, a widely used statistical technique that calculates underlying periodicities of time series data. Spectral analysis is feasible for many temporal datasets because the independent variable, time, is assumed to be of constant interval and many dependent variables behave in a cyclical manner. Generally speaking, a spectral transform produces a function of power spectral density (PSD) vs frequency for the raw data (i.e. distribution of individual frequency components on the x-axis that can be compared by relative strength or amplitude on the y-axis). Spectral analysis is usually performed on 1D data sets, although 2D and 3D analyses can be done (Rayner, 2001).

1.10.1. Generic Example

Figures 1.10 to 1.12 demonstrate a simple 1D spectral transformation of a synthetic signal from the time domain (i.e. distribution of observations with respect to time) to the frequency domain (i.e. distribution of frequency components) via conventional Fourier analysis. In brief, this transformation tells what distinct cycles, which would otherwise be indistinguishable, are contained within the original signal, and their relative strengths. Figure 1.10 shows four sine functions, each with varying amplitudes (10, 5, 4 and 3) and frequencies (1, 1/2, 1/3 and 1/4):

- 10 * sine (2* pi * x * (1/1) + 0)
- 5 * sine (2* pi * x * (1/2) + 0)
- 4 * sine (2* pi * x * (1/3) + 0)
- 3 * sine (2* pi * x * (1/4) + 0)

When plotted individually, these attributes can be determined by counting cycles per year and using the y-axis to estimate amplitude. All four functions are added together to create one combined function in Figure 1.11, where individual amplitudes and frequencies are no longer discernable by visual examination. In Figure 1.12, a spectral analysis method translates the combined signal into its frequency components. Here, varying amplitudes and frequencies are detectable as four spikes across a new x-axis that represents a spectrum of frequencies or inversely, periods. In this example, the clearly defined spikes indicate perfect uniformity in the fluctuations of the original four sine functions.

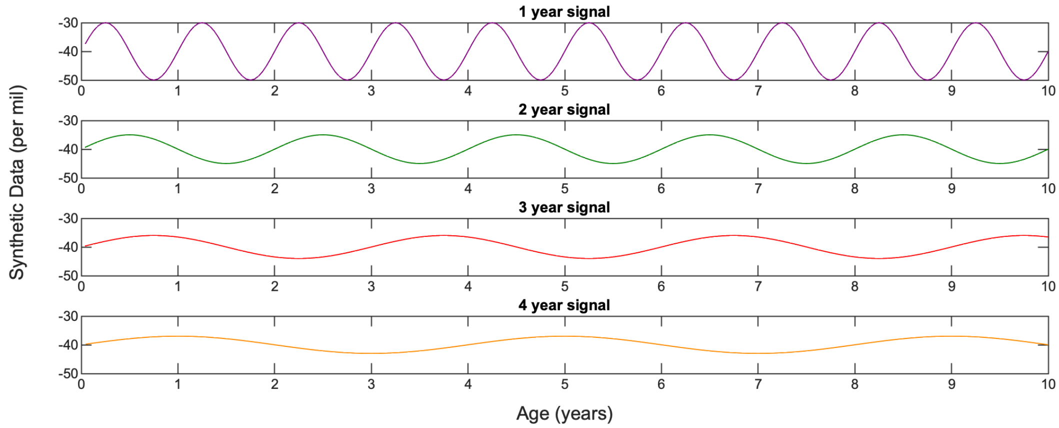

Figure 1.10: Four independent functions with frequencies of 1, 1/2, 1/3, and 1/4 occurrences per year

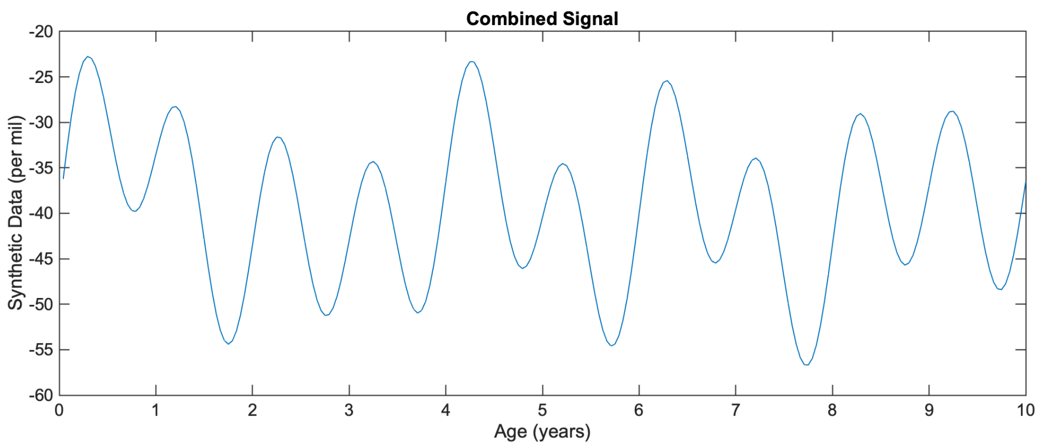

Figure 1.11: Independent functions from Figure 1.11 are added together to create a combined function

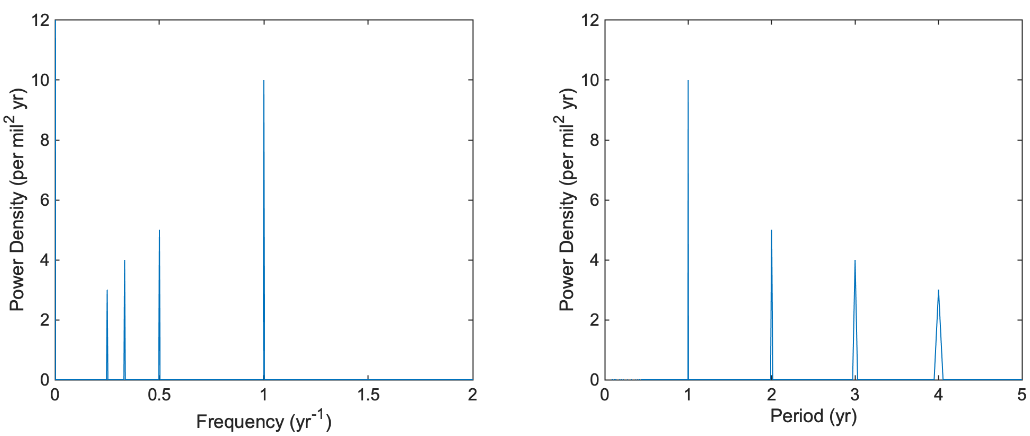

Figure 1.12: Power density of the combined function (Figure 1.11) showing frequencies of 1, 1/2, 1/3 and 1/4 occurrence(s) per year and consequent periods of 1, 2, 3 and 4 year(s)

1.10.2. Practical Examples

Real world examples are less straightforward than the above transformation because (1) human or environmental patterns are not perfectly cyclical and (2) many observations cannot be described by just few isolated frequency components, but rather a spectrum. Take, for example, temperature during June in the foothills of Boulder, CO (Figure 1.13). Although there is a clear pattern of rising and falling temperature throughout the day, the cycle is not perfectly consistent. When this signal is translated to the frequency domain (Figure 1.14), there is a strong spike to indicate the original signal most strongly fluctuates at a frequency of 30 occurrences per month (i.e. the diurnal temperature signal). The transformation also picks up on less obvious signals with lower amplitudes, showing the variable nature of cycles that exist in the real world.

In addition to local weather patterns, spectral analysis can be applied to a wide range of topics to determine underlying periodicities. For example, this type of analysis has been used in medicine to understand heart rate variability during different sleep cycles (Busek et al., 2005) and among patients with specific psychological conditions (Cohen et al., 1997; Yeragani et al., 1993). In real estate, spectral analyses have uncovered the existence of 7-year, 8-year and 3-year securitized property market cycles in the US, UK and Australia, respectively (Wilson and Okunev, 1999). For the purposes of this study, spectral analysis will help quantify the strength of Arctic and Antarctic high-frequency climate signals contained within raw and diffusion corrected water isotope data during the last ice age, subsequent deglaciation and the Holocene. Using this information, we can further understand the interplay between northern and southern climate forcing.

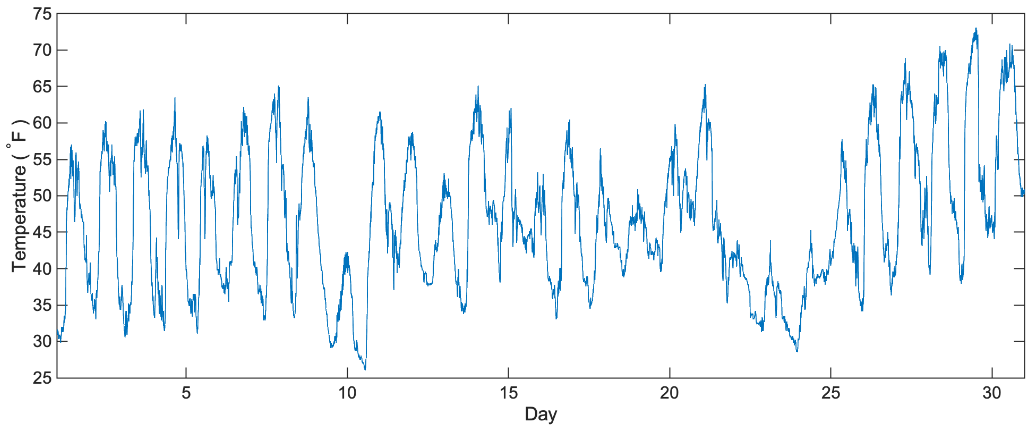

Figure 1.13: Temperature (F) in Sugarloaf, CO during June 2019

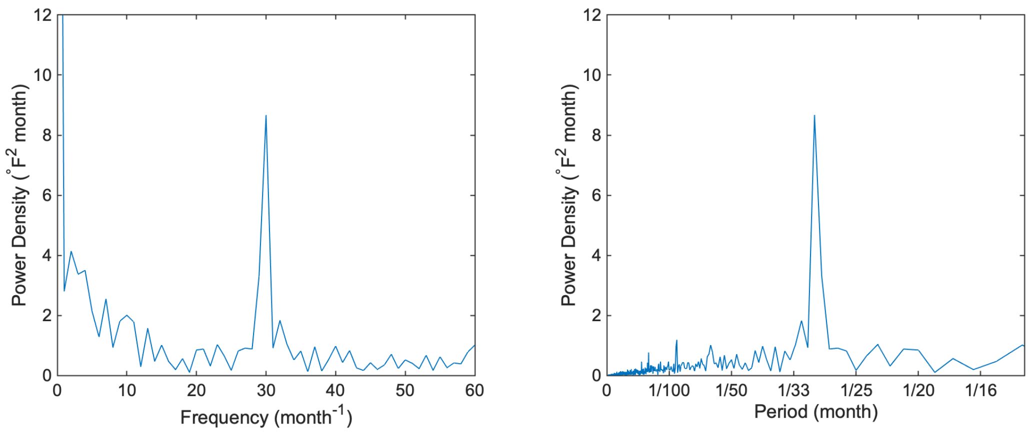

Figure 1.14: Power density of temperature in Sugarloaf, CO during the month of June; Spike at ~30 occurrence(s) per year (left) and ~1/30 month (right) indicates the diurnal temperature signal

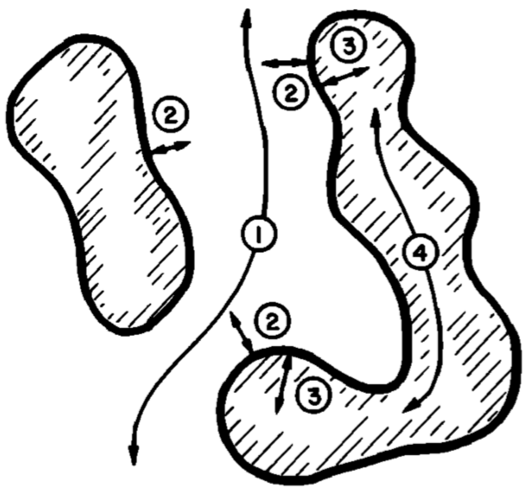

Figure 1.15: Four modes of isotopic exchange ocurring during firn diffusion (Whillans & Grootes, 1985)

1.11. Diffusion

The largest obstacle to interpreting high-frequency signals of a water isotope record is diffusion, a process by which water molecules are vertically displaced from their original position within the firn column (i.e. uncompressed snowfall in the uppermost ~50-150 meters of an ice sheet) via isotopic mixing. Firn is a porous and permeable substance, where water vapor in the atmosphere is able to move through pathways between grains of ice. Here, there are four modes of isotopic exchange occurring along temperature and pressure gradients: (1) vapor-vapor, (2) vapor-ice surface, (3) ice surface-ice interior and (4) through the ice matrix (Whillans & Grootes, 1985).

Diffusion of water molecules involving the vapor phase occurs most rapidly and effectively smooths (i.e. decreases the amplitude of) the isotopic signal that was originally deposited at the ice sheet surface (Whillans & Grootes, 1985). This mode of diffusion disproportionately dampens the high-frequency portions of a water isotope signal but is slowed considerably at the close-off depth (i.e. depth at which firn is compressed into ice and vapor pores are cut off from atmosphere) (Kahle et al., 2018). The depth at which this transformation occurs varies by location due to differences in accumulation rate and temperature but is estimated to exist at a pore density of approximately 804.3 kg/m^3 (Johnsen et al., 2000). Solid phase diffusion continues to occur below the close-off depth but is orders of magnitude slower than vapor phase diffusion (Jones et al., 2017).

Evidence of increased diffusion among high-frequency climate signals can be seen in power spectral density (PSD) plots from varying windows of time within the water isotope record. Below, the WDC water isotope record has been divided into three discrete portions: 0-10 ka bp (red), 10-20 ka pb (blue) and 20-30 ka bp (green). Each portion is converted to its frequency domain using the same spectral analysis technique and plotted together. A few indicators of high-frequency diffusion include:

1. Diffusion progressively affecting more signals at the higher frequency end in older portions of ice, creating a shoulder, or curvature on the plot
2. The progressive decline of the annual signal (period = 1 yr) in older portions of ice

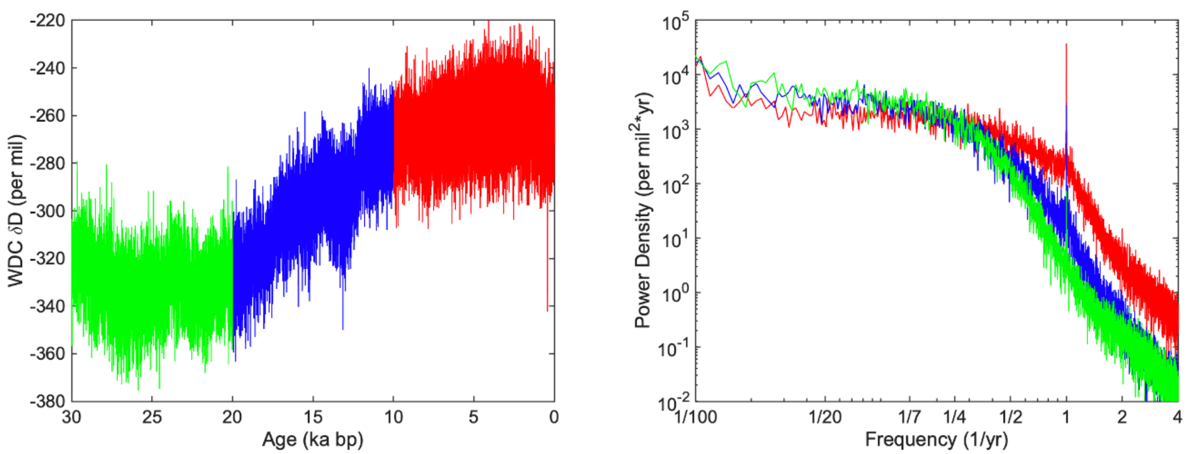

Figure 1.16: WDC δD record (left) divided into 0-10 (red), 10-20 (blue) and 20-30 (green) ka bp; respective PDF for each timeframe (right); diffusion progressively dampens higher frequencies in the water isotope signal

In this study we use a series of equations, described later in Methods, to estimate high-frequency power densities (e.g. >1/10 yr^{-1}) prior to attenuation by diffusion in order to accurately quantify the strength of high-frequency climate variability. This correction essentially flattens the shoulder, or curvature, so that accurate power densities can be estimated for frequencies within the diffused portion.

Chapter 2: METHODS

2.1. Sampling Methods (CFA-CRDS vs discrete IRMS)

Crucial to this analysis are the methodologies used in obtaining the EGRIP, SPC and WDC water isotope data. Historically, water isotope measurements, including those from NGRIP, have been taken by analyzing 3-5 centimeter discrete samples of ice through an isotope ratio mass spectrometer (IRMS). This technique produced incredibly useful early studies of ice core water isotopes (Dansgaard et al., 1969; Johnsen et al., 1972; Lorius et al., 1979) but lacks the temporal efficiency and data density needed for more detailed paleoclimate investigations. In recent years, higher precision laser absorption spectroscopy (LAS) has become the leading alternative to IRMS. This study utilizes one method of LAS known as cavity ring down laser spectroscopy (CRDS; manufactured by Picarro, Inc.) in conjunction with continuous flow analysis (CFA) techniques to create a semi-automated system (CFA-CRDS; developed at the INSTAAR Stable Isotope Lab) aimed at increasing water isotope data resolution while minimizing data collection time.

The CFA-CRDS system can be broken down into three main subsystems: the ice core melting component, the liquid-to-vapor transformer and the isotopic analyzer. The melting component holds one-meter long ice core sticks measuring approximately 1.3 cm in height and width over a melt head maintained at 14.6°C. At this temperature, the sticks typically melt at a rate of 2.5 cm per minute. The ice core melt water is filtered to remove particulates and fed into a glass vial (debubbler) where air bubbles are allowed to escape. Next, a fraction of this water is directed through a nebulizer which vaporizes the liquid sample and sends it directly into the Picarro instrument. Here, laser pulses which have been attuned to the sample's molecular fingerprint are directed into a mirrored cavity and left to decay via absorption by the vapor sample. The amount of time it takes the laser to decay, known as a "ring down" time, is then compared to the ring down time when no sample is present within the cavity. Precise D and ^{18}O concentrations are derived by the instrument in real time by comparing these two values. A lab technician is required to routinely calibrate and feed the system during data collection periods (Jones et al., 2017a).

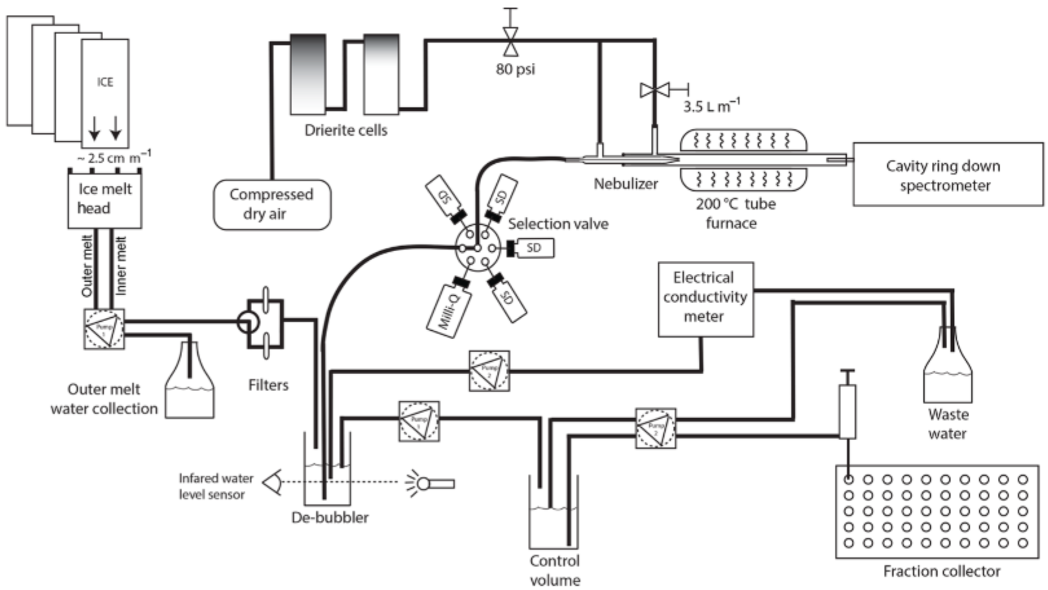

Figure 2.1: Schematic of the CFA-CRDS system used for measurement of ice core water isotopes (Jones et al., 2017a)

A key advantage of the CFA-CRDS system over traditional discrete IRMS systems is that it provides an order of magnitude increase in data density in just 1/6th the amount of time. This results in ice core water isotope records which contain the higher resolution nuances necessary for spectral analysis. These nuances may include more accurate amplitudes of high-frequency signals and/or entirely new fluctuations that may have been smoothed over by discrete IRMS sampling. Because EGRIP, SPC and WDC water isotope data has been obtained using CFA-CRDS, these cores will offer the most accurate results in terms of high-frequency climate variability.

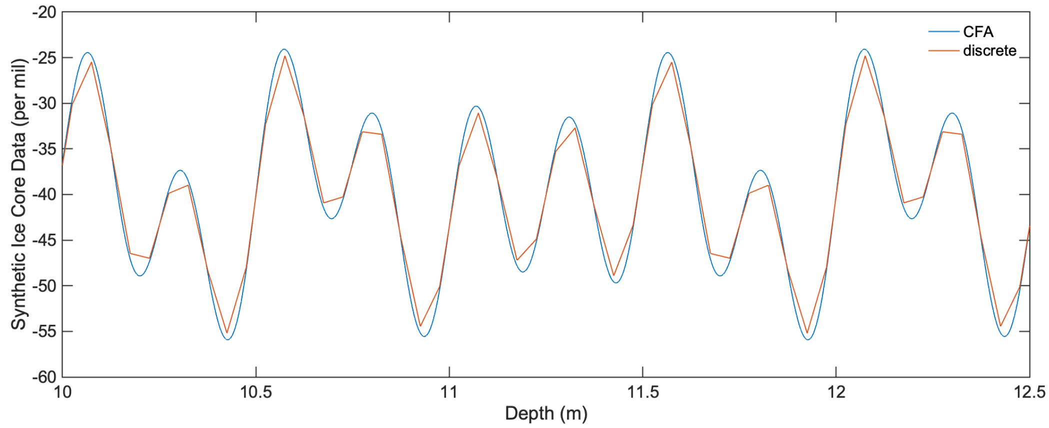

Figure 2.2: Visualization of increased data density from the CFA-CRDS system necessary for spectral analysis of high-frequency climate variability; Notice that at ~10.8 m, for example, the amplitude of the discrete signal is artificially reduced by 30% compared to the CFA.

2.2. Multi-taper Method of spectral analysis

To quantify high-frequency climate signals at our study sites, we use a multi-taper method (MTM) of spectral analysis developed by Peter Huybers and informed by Percival & Walden (1993). MTM spectral analysis is effective at overcoming many of the limitations associated with conventional non-tapered Fourier analysis, which often produces skewed and noisy realizations of the process of interest. MTM is different in that it averages many realizations of the same data using a series of Slepian tapers, or filters that emphasize varying portions of a data set, leading to smoother and less biased estimates of spectral density. This method is especially useful for non-time-locked and non-phase-locked data.

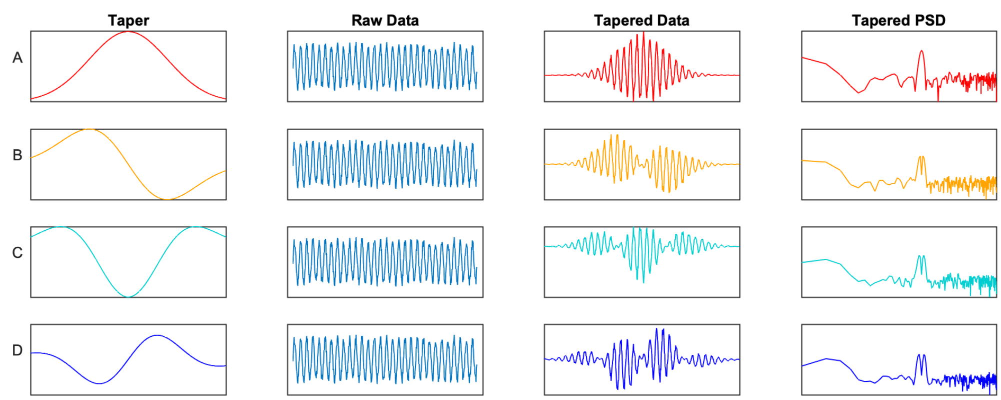

Figure 2.3: Breakdown of a generic MTM spectral analysis transformation; Tapers A, B, C, and D are applied to the same data set to produce four separate tapered functions which emphasize varying portions of the raw data

Figures 2.3-2.4 depict a generic example of MTM spectral analysis. First, a series of Slepian tapers (individually identified as tapers A, B, C and D) are applied to the same data set to produce a series of tapered data. The tapered data are then converted to their frequency domains via a Fourier transform producing four separate, but similar realizations of the original signal's spectral density. The average of these four functions produces a final MTM spectral density estimate.

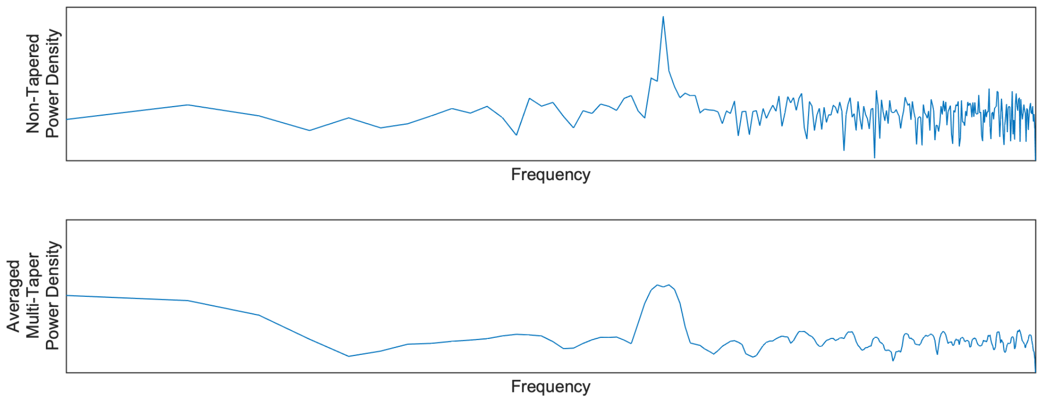

Figure 2.4: Comparison of the noisy non-tapered (top) and smooth MTM (bottom) power spectral density (PSD) functions from the same data set

Figure 2.4 compares the spectral density estimate from the above MTM analysis to that of a conventional non-tapered method. Despite using the exact same data set, these methods result in two different realizations. The MTM result offers a smoothed estimate of prominent spectral characteristics while the conventional method provides noisier detail. MTM analysis is used in this study because we are less concerned with the subtleties of individual frequency features and more so with broad trends in power density across bands of multiple frequencies.

We spectrally analyze the water isotope records from EGRIP, NGRIP, WDC and SPC in 400-year windows with a timestep of 200 years from 0-50 ka bp. A window size of 400 years provides adequate data to calculate power density spectra in the interannual to decadal frequencies of interest. For example, the 4-year signal power density estimation is based off the amplitude of 100 full cycles within a 400-year window.

2.3. Diffusion Correction

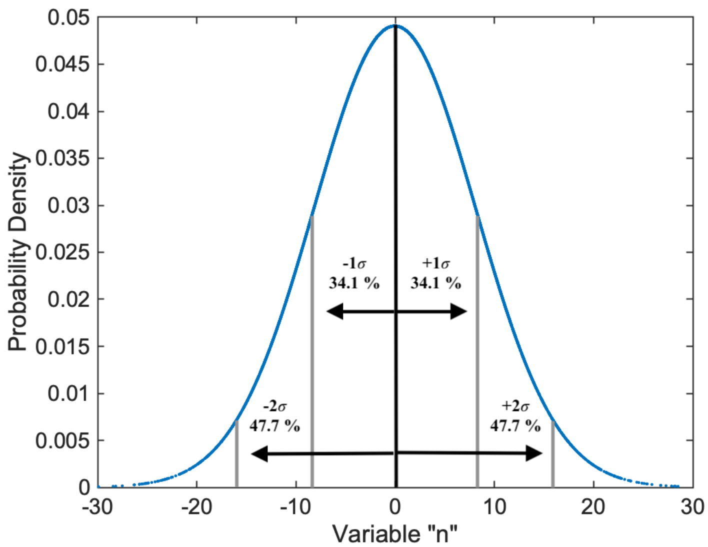

Figure 2.5: General structure of a Gaussian PDF; the standard deviation (sigma) is used to obtian standardized probability ranges

Values of cumulative mean water molecule diffusion, known as "diffusion lengths", can be estimated for windows of time or depth along a water isotope signal by evaluating dampened sections of its high-frequency spectrum (Jones et al., 2017b; Hughes et al., 2020). Using these diffusion lengths, the raw spectrum can be back-corrected to reflect original, un-diffused conditions. This technique is built upon the observation that diffusion of water molecules in firn can be well described by a Gaussian distribution.

A Gaussian distribution, sometimes referred to as a "bell curve", is a type of continuous probability distribution where, generally speaking, observations from a sample set cluster around a mean. A defining characteristic of a Gaussian distribution is its standard deviation, denoted as σ (i.e. sigma). Mathematically, the standard deviation of a data set is defined as:

$$\sigma = \sqrt{\frac{\Sigma(x-u)^2}{n}} \tag{8}$$

where x is the set of observations, u is the mean of the sample set, and n is the number of samples. In essence, the standard deviation σ is a measure of variation within a set of values. If sigma is low, observations trend close to the mean and if sigma is high, observations are spread over a wider range.

This type of distribution is often interpreted by its probability density function (PDF) which calculates the probability of a random variable falling within a specified range of values. The general form of a Gaussian PDF is:

$$f(x) = \frac{1}{\sigma\sqrt{2\pi}} e^{-\frac{1}{2}\left(\frac{x-u}{\sigma}\right)^2} \tag{9}$$

where σ is the standard deviation, x is the set of observations, and u is the mean of the sample set. Probability is determined by integrating between a specific range of x values. For example, the integral of the entire function from x_1 to x_n will always be equal to 1. This integral can be converted to a percent probability by multiplying by one hundred percent (i.e. there is a 100% chance that a random variable will fall somewhere within the range of the entire set of observations). To calculate more specific probabilities, the integral is taken between a defined range of x values. An interesting characteristic of Gaussian PDF's is that sigma can be used to obtain standardized ranges:

- where **x = mean +/- 1 σ** contains 68.2% of all observations
- where **x = mean +/- 2 σ** contains 95.5% of all observations
- where **x = mean +/- 3 σ** contains 99.7% of all observations

In other words, there exists a 68.2% chance that a random variable will fall somewhere in the range of x = mean +/- 1 standard deviation in a Gaussian distributed data set (Dasgupta & Wahed, 2014).

Many natural phenomena are well-described by Gaussian distributions, including height in a population, temperature, or for our purposes, diffusion of water molecules in firn (Johnsen et al., 2000). As stated earlier, we can estimate diffusion lengths (i.e. values of cumulative mean water molecule diffusion) for sections of an ice core by use of spectral analysis to ultimately back-correct the spectra. Diffusion lengths are equivalent to the estimated standard deviation, sigma, of water molecule diffusion and describe the maximum range that 68.2% of water molecules will travel during diffusional processes (Johnsen et al., 2000). For example, if sigma is determined to be 0.06 m for a portion of ice core, this means 68.2% of water molecules have traveled up to +/- 0.06 m from their original positions by mode of diffusion. This also means that a molecule moving 0.13 m is an extremely rare event, as it exceeds +2 sigma, and would only occur in less than ~4.5% of observations. We can also think of diffusion lengths in terms of time, as many ice core water isotope records are evaluated based on their chronologies. If a diffusion length is determined to be 1 year, this means 68.2% of water molecules traveled as far as the adjacent annual layer of snowfall, either above or below their original point of deposition. Similarly, a water molecule diffusing +/- 2.1 annual layers would be an extremely rare event, as this occurs in less than ~4.5% of observations in this portion of ice core.

To determine sigma for sections of an ice core, we must fit a Gaussian curve to the diffused portion of the spectra. For a water isotope record in the time domain (as opposed to depth), the general form of a Gaussian PDF to estimate diffusion is:

$$G(a) = \frac{1}{\sigma_a\sqrt{2\pi}} e^{\left(\frac{-a^2}{2\sigma_a^2}\right)} \tag{10}$$

where a is age and σ_a is the standard deviation (i.e. diffusion length; units of years). If this function is convolved with an isotope record of arbitrary form, the power density spectrum of the resulting signal takes on the form of:

$$P(f) = P_o(f)e^{[-(2\pi f\sigma_a)^2]} \tag{11}$$

where $P_o(f)$ is the power spectrum of the undiffused signal, f is frequency and σ_a remains the standard deviation.

We begin by identifying the frequencies at which diffusion distorts the spectra for each window and later, fit a Gaussian to these portions using equation (10). At decadal and higher frequencies (e.g. 1/10 yr^{-1} to 1/2 yr^{-1} in the Holocene), the amplitude of the signals progressively decreases at higher and higher frequencies, generally following the trace of a Gaussian curve. This is the region of the spectrum where diffusion is evident (Figure 2.6). At frequencies higher than about 1/2 yr^{-1} in the Holocene, analytical noise overwhelms the diffusion signal, creating a kink or bend in the spectrum. Due to increased diffusion in older ice, the diffused portion of the spectrum will shift to slightly lower frequencies the further back we analyze.

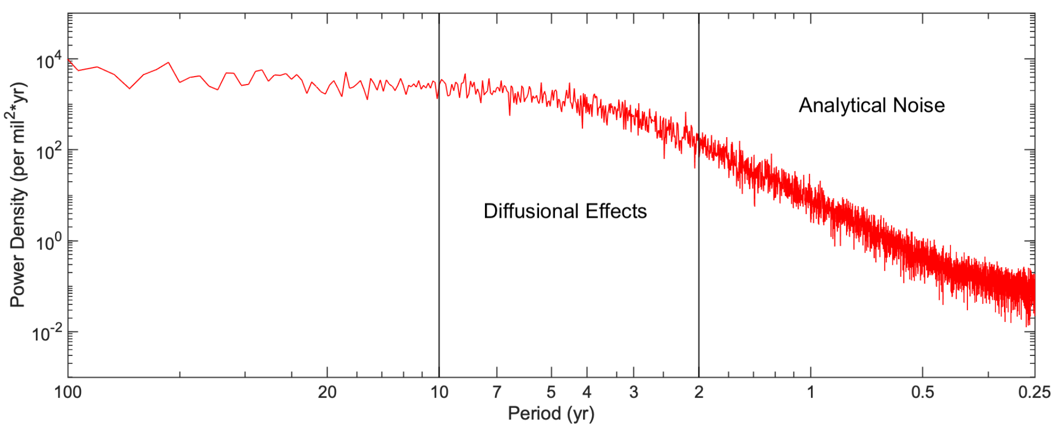

Figure 2.6: PSD of the EGRIP δD record during the Holocene (0-11.7 ka bp); the diffused interval occurs between the 2 and 10 year signals; at higher frequncies (>1/2 year^{-1}) the signal is overwhelmed by analyitical noise

Within the diffused interval, we create twelve equally spaced logarithmic bins in which data is averaged, denoted by green dots in Figures 2.9-2.10, that become reference points for regression fits. The log-binning ensures that increased data density present at higher frequencies is the spectrum does not weight the fits towards those higher frequencies, which would then skew the estimated diffusion lengths. A unique complication arises in this process at WDC. Here, annual accumulation is high enough to preserve the annual signal, which is much stronger than other signals, throughout the Holocene and as far back as 14 ka bp. For data where the annual signal is preserved within the diffusion correction interval, we exclude the period range of 0.95 -1.05 years from our sequence of logarithmically spaced points to avoid skewing our regressions. Without this exclusion, the fits would slightly underestimate diffusion length and pre-diffused spectra.

Next, we fit a Gaussian (i.e. Equation 10) to the equally spaced log bins using a least squares fitting technique. With this approach, we test a variety of regressions using a mixture of different x (frequency) and y (spectral density) values and sum the squared residuals (i.e. square of the difference between observed values provided by empirical data and fitted values provided by the model) for each fit. The regression with the lowest sum of squared residuals is deemed most optimal and is used to calculate the diffusion length, which is then used in subsequent diffusion correction calculations. This step allows for quantification of σ_a. The spectral equivalent of σ_a, denoted as σ_g, is related by:

$$\sigma_a = \frac{1}{2\pi\sqrt{2}} * \frac{1}{\sigma_g} \tag{12}$$

The diffusion length, σ_a (units of years), can also be converted to depth by the following conversion:

$$\sigma_z = \sigma_a * \lambda_{avg} \tag{13}$$

where σ_z is diffusion length (units of meters) and λ_{avg} is mean annual layer thickness (meter/year) of the interval of ice being analyzed (Jones et al., 2017b). Temporal diffusion lengths are typically related to accumulation rate, where older layers formed in the glacial period (>11 ka bp) relative to the Holocene (0-11 ka bp) will have a larger diffusion length due to decreased accumulation. Conversely, metric diffusion lengths typically decrease with age due to the dominance of increased thinning in deeper layers of ice.

Finally, we make an estimation of the power densities prior to diffusion by rearranging equation (11) so that:

$$P_o(f) = \frac{P(f)}{e^{[-(2\pi f\sigma_a)^2]}} \tag{14}$$

where $P_o(f)$ is the undiffused power spectrum, $P(f)$ is the diffused power spectrum, f is frequency and σ_a is the diffusion length in the time domain. We use $P_o(f)$ to quantify high frequency climate signals as they would have existed prior to the dampening effects of diffusion.

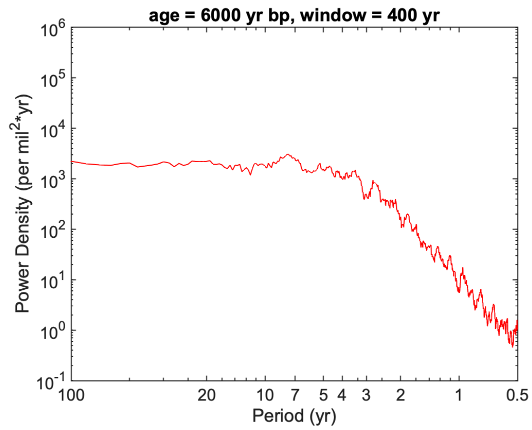

Figure 2.7: Example of a raw (i.e. non-diffusion corrected) PSD function; progressive downturn at higher frequencies is a result of attentuation by diffusion in the firn column

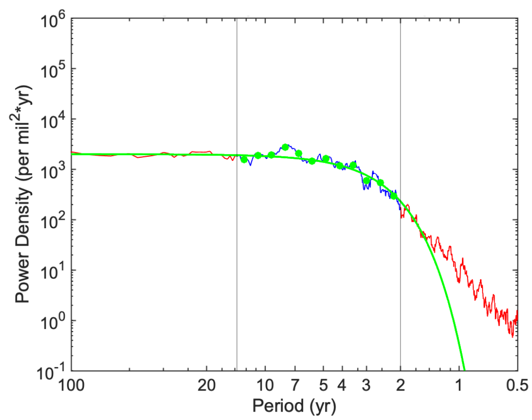

Figure 2.8: Example of the equally spaced logarithmic bins (green dots) that are used to avoid skewing Gaussian regression fits (solid green line) to higher frequencies with increased data density

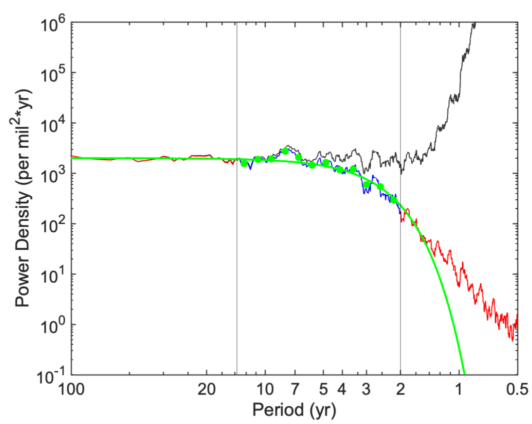

Figure 2.9: Example of a diffusion corrected PSD function (solid black line) that is used in further calculations of high-frequency variability

2.4. Quantification of Signal Strength

The diffusion corrected power density spectra, $P_o(f)$, is then used to estimate the strength of various climate signals for each 400 year window. We calculate average power density (P_{ave}) for frequency bands of interest (e.g. 4-7, 5-8, 6-9, 10-15, 15-20, and 20-30 year signals) by integrating across the frequency interval and dividing by the range:

$$\mathrm{P}_{ave} = \frac{\int_{f_a}^{f_b} \mathrm{P_o(f)}}{f_b - f_a} \tag{15}$$

where f_a and f_b are the upper and lower limits of the frequency band, respectively. This method ensures that the calculation is not weighted towards higher frequencies with increased data density. Relative strength (P_{amp}), or amplitude, is then calculated for each window as the square root of average power density (P_{ave}):

$$\mathrm{P}_{amp} = \sqrt{P_{ave}} \tag{16}$$

To normalize these amplitudes to the modern, we divide P_{amp} of each window by P_{amp} of the second most recent window in our analysis (i.e. 400 ka bp). The first most recent data point (i.e. 200 ka bp) exists in the modern firn column where diffusion has not fully progressed and thus we must normalize with an earlier timeframe. With this approach, frequency bands with relative amplitudes greater than one can be interpreted as more variable than "modern" conditions (i.e. about 400-800 years before present, which is also prior to the industrial revolution), and vice versa.

Chapter 3: RESULTS

3.1. Greenland

3.1.1. NGRIP vs. EGRIP Sampling Resolution

We are initially interested in comparing the mm-resolution water isotope data from EGRIP to the cm-resolution data from NGRIP. Specifically, we want to confirm the value of having an order of magnitude increase in data density for analysis of high-frequency climate variability to 50 ka bp. To do so, we down sample the EGRIP depth record to 5 cm, apply an age-depth scale and examine how this signal compares to the original 1 mm record (Figure 3.1).

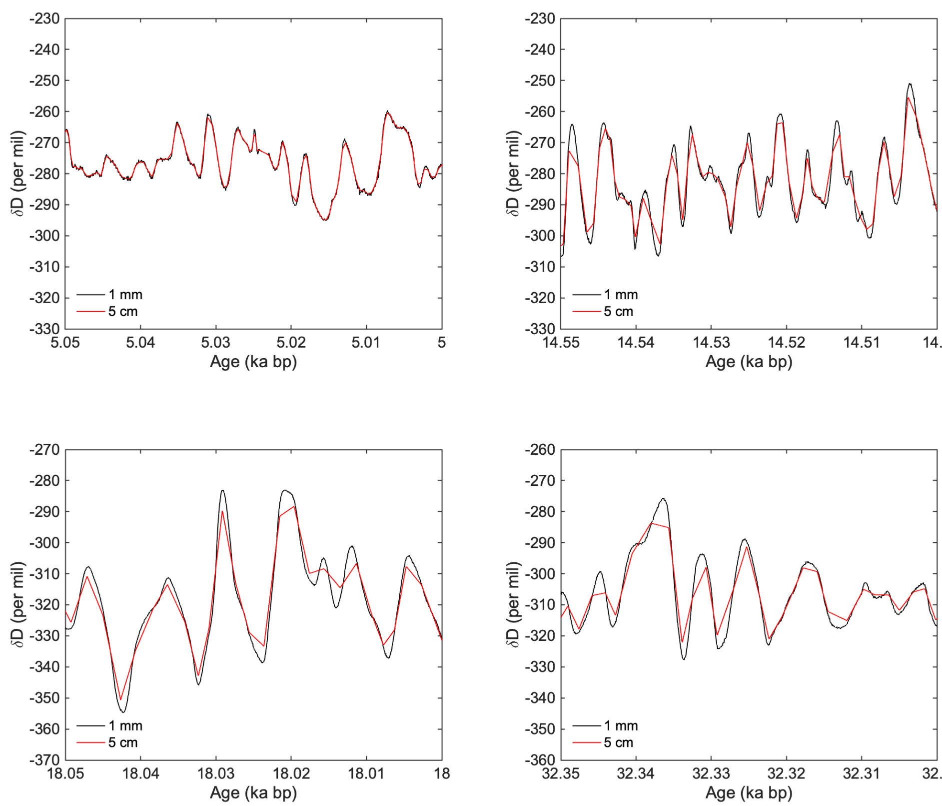

Figure 3.1: Comparison of original 1-mm scale EGRIP record (black) to downsampled 5-cm EGRIP record (red) in 50 year windows; Downsampled 5-cm record artificially reduces the amplitude of interannual and decadal fluctuations after approximately 12 ka bp

Due to increased accumulation in the Holocene compared to the glacial and minimal compaction of snowfall in the uppermost layers of the ice sheet, the original 1 mm and down-sampled 5 cm records are comparable to approximately 11.7 ka bp. After this, interannual and decadal scale fluctuations experience a decrease in amplitude in the down-sampled 5 cm record. This loss in amplitude becomes more prominent the further back in time we analyze, driven primarily by increased thinning and lower accumulation in the glacial. This suggests that results from the 5 cm NGRIP record will significantly underestimate the strength of high-frequency climate signals for the timeframe 12 to 50 ka bp.

Next, we compare relative amplitudes in the interannual and decadal range for the original 1 mm EGRIP, down-sampled 5 cm EGRIP and original 5 cm NGRIP records from 0 to 50 ka bp (Figure 3.2). We find relative strength for the interannual and decadal bands is roughly the same for all the three records from 0 to 23 ka bp. We find that the 5 cm records underestimate relative strength from 23 to 50 ka bp by approximately 25% for the 7-10 year band, 20% for the 10-15 year band and 5-10% for the 20-30 year band. From this, we determine the 5 cm NGRIP record to be inadequate for our purposes of analyzing high-frequency climate variability in Greenland during a majority of the Last Glacial Period (LGP).

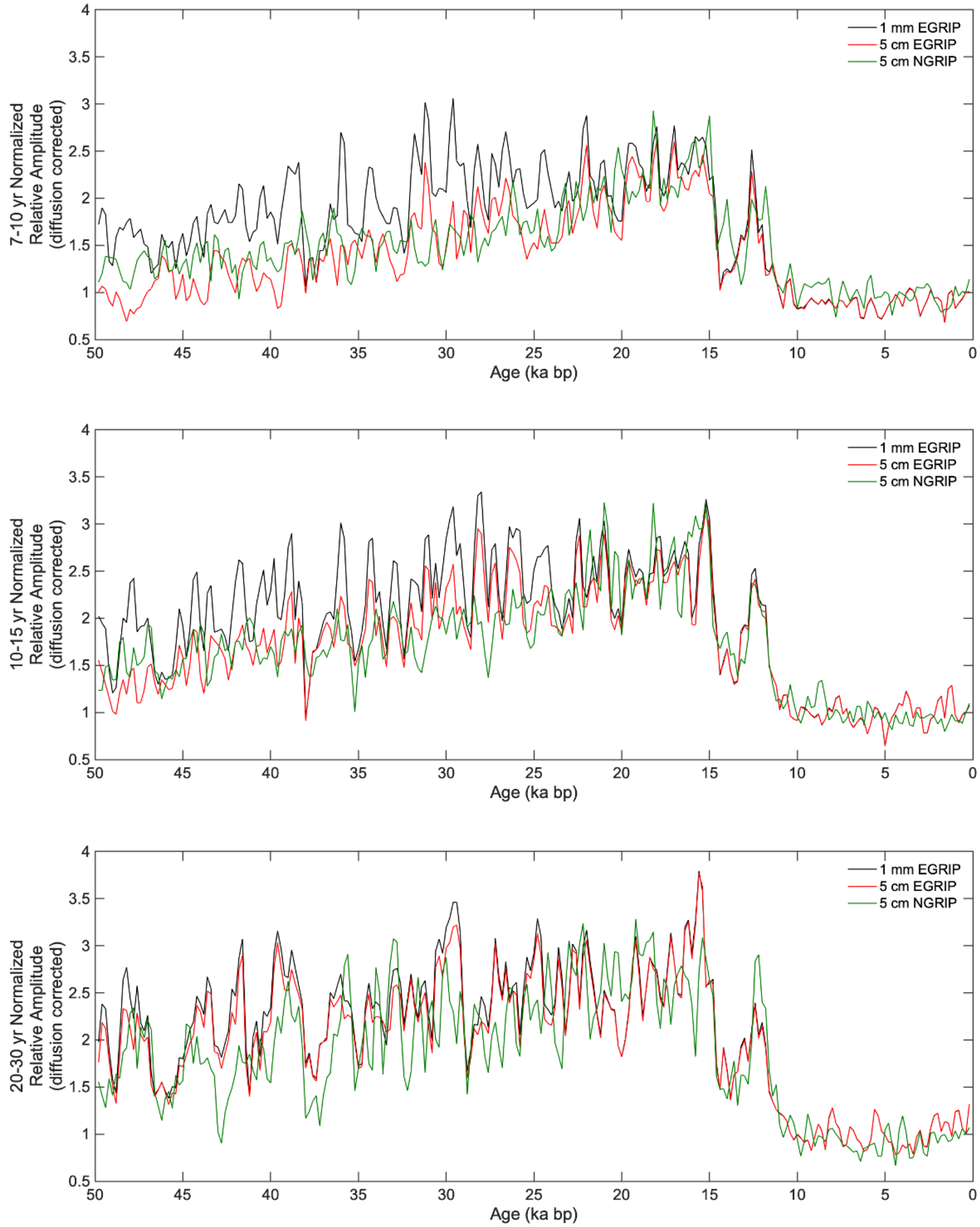

Figure 3.2: Comparison of strength of high-frequency climate variability between original 1-mm EGRIP (black), downsampled 5-cm EGRIP (red) and original 5-cm NGRIP (green) records; the cm-scale records result in underestimations of high-frequency climate variability, especially during the LGP

3.1.2. EGRIP Preliminary Analyses

Our analysis of EGRIP 1 mm and NGRIP 5 cm records shows the value of the high-resolution EGRIP data in analyzing interannual to decadal signals (7 to 30 yrs) in the LGP. Next, we determine which frequencies in the EGRIP ice core have been significantly attenuated by diffusion; we isolate the 1, 1/2, 1/3, 1/4, 1/5, 1/7 and 1/10 year^{-1} frequencies and plot raw relative amplitudes together (Figure 3.3). The 1/20, 1/30, and 1/50 year frequencies, which have undergone minimal diffusion, are included in this analysis as references.

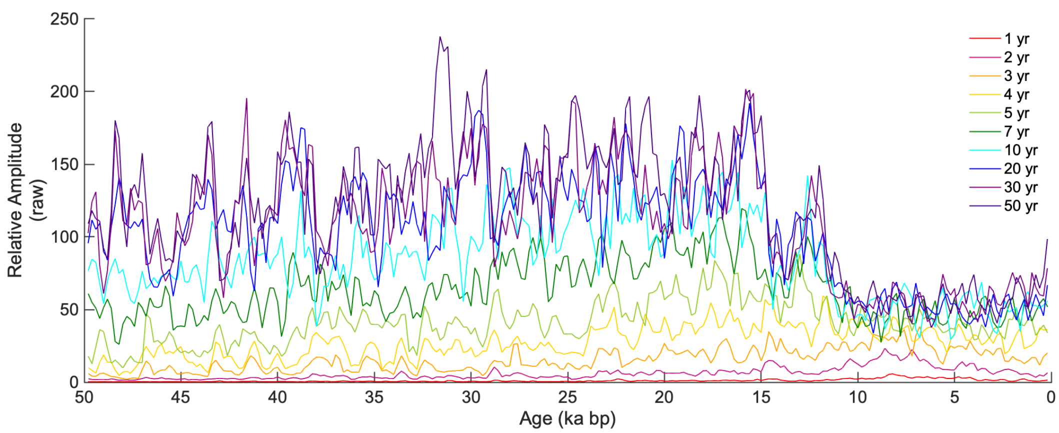

Figure 3.3: Strength of raw (i.e. non-diffusion corrected) isolated frequencies in the EGRIP δD record; Frequencies with periods of less than 7 years exhibit substantial attenuation from diffusion in the firn

We find that the annual (i.e. 1 year) signal is completely diffused away throughout the entire record and the 2-4 year periods have been significantly distorted, especially in the LGP. We are confident that climate signals greater than the 7 year period can be accurately diffusion corrected because the amplitude of the signal does not approach zero at any point over the last 50 kyr. Thus, we include periods >7 years in further analysis of climate variability at EGRIP, representing the highest-frequency analysis yet achieved on a Greenland ice core, especially in the LGP.

Next, we analyze EGRIP diffusion lengths from 0-50 ka bp to gain insight into accumulation trends (Figure 3.4). Each data point represents estimated average diffusion length in each corresponding 400 year window. On average, diffusion lengths in the time domain are around 1.2 years during the LGP and decrease 50% to 0.6 years during the Holocene.

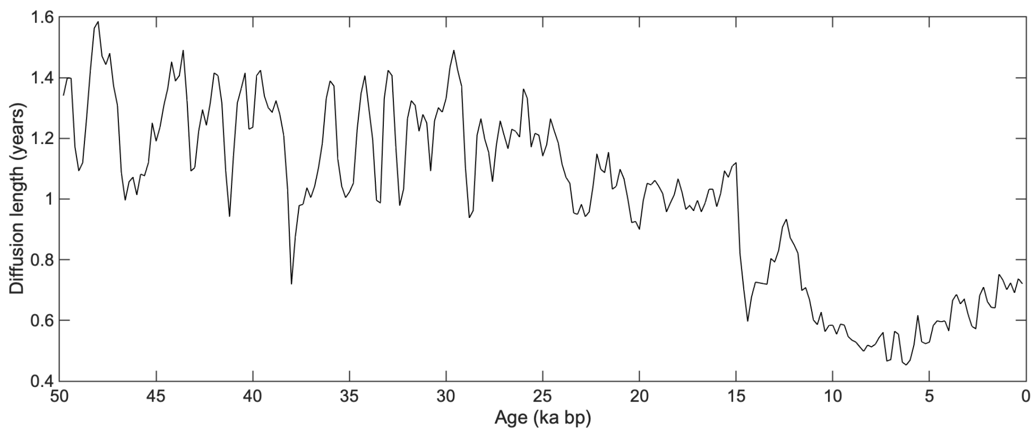

Figure 3.4: EGRIP diffusion lengths in units of years; analysis done in 400 year windows with a timestep of 200 years

We also find that EGRIP diffusion lengths track inversely with the EGRIP water isotope signal, a proxy for local temperature (Figure 3.5). During the Holocene, diffusion lengths decrease because increased accumulation make it more difficult for diffusing water molecules to cross annual layer boundaries. Conversely, decreased annual layer thickness during the LGP allows more water molecules to diffuse across annual boundaries, increasing the average diffusion length. We even see changes in diffusion length associated with the Younger Dryas (11.7-12.9 ka bp), Bølling Allerød (12.9-15 ka bp) and Dansgaard-Oeschger (DO) events.

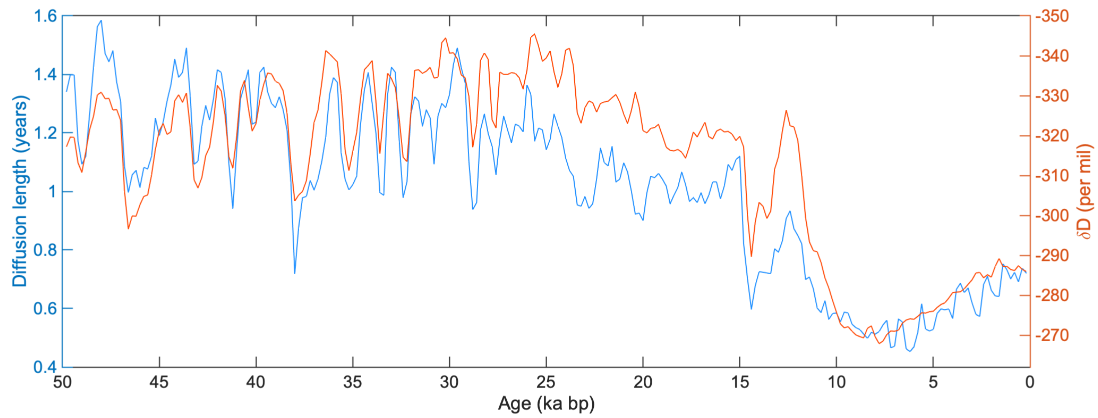

Figure 3.5: EGRIP diffusion lengths (yrs) plotted with the inverted EGRIP δD record; analysis done in 400 year windows with a timestep of 200 years; elevated diffusion lengths during the LGP are largely driven by decreased accumulation in colder temperatures

3.1.3. EGRIP Diffusion-Corrected Results

Next, we look at diffusion-corrected strength of signals at EGRIP. As mentioned before, this analysis was done in 400 year windows with a timestep of 200 years using methodologies from Jones et al., 2018. We are especially interested in how high-frequency climate variability evolved over the course of the last glacial-interglacial transition. The intervals of time that bookend this transition, the Last Glacial Period (LGP; occurring from 11.7 - 115 ka bp) and the Holocene (occurring from 0-11.7 ka bp), were characterized by substantially different climatic conditions (e.g. mean temperatures, ice extents, atmospheric compositions, etc.) and we are interested in determining if these factors affected the strength of high-frequency climate variability around mean temperature in northeastern Greenland. If so, further analysis using general circulation models (GCMs) will be necessary to elucidate which factors drive differences in variability between the LGP and Holocene.

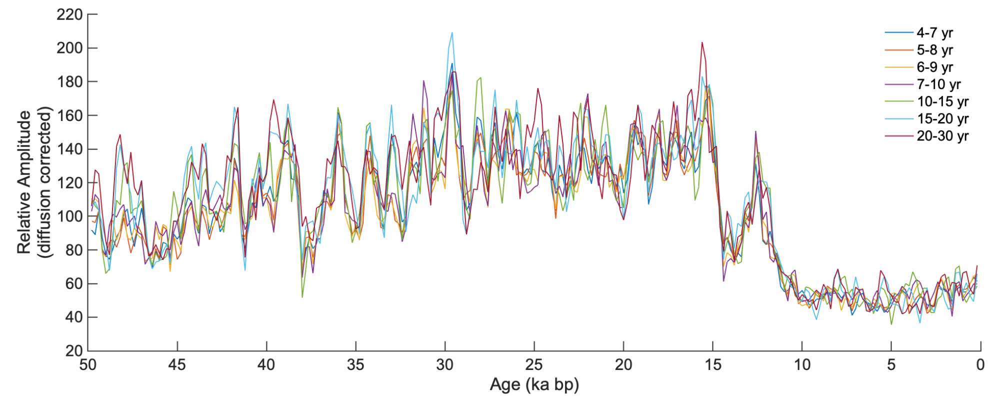

Figure 3.6: Diffusion-corrected strength of high-frequency climate variability at EGRIP (northeastern Greenland); analysis done in 400 year windows with a timestep of 200 years

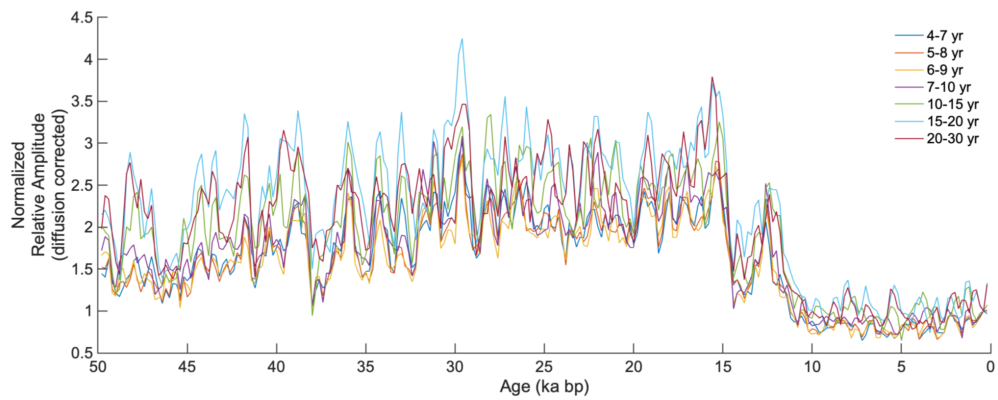

Figure 3.7: Diffusion-corrected strength of high-frequency climate variability at EGRIP (northeastern Greenland) normalized to modern conditions (i.e. 400 years bp); analysis done in 400 year windows with a timestep of 200 years

We note three distinct periods across this analysis: the Holocene from 0-12 ka bp, the last glacial maximum (LGM) from 16-32 ka bp and the early glacial from 32 ka bp and earlier. The Holocene is characterized by relatively stable reduced climate variability while the LGM experiences noisier elevated climate variability. Prior to the LGM, variability appears to gradually increase from a moderate level. Most importantly, we identify a 60% reduction in the strength of diffusion corrected high-frequency climate signals at EGRIP from the LGP to the Holocene. In other words, climate variability was approximately 2.5 times greater during the glacial period than today. This pattern is consistent across all bands analyzed. We also note that the 16.2 ka signal found in Jones, 2018 is not clearly present at EGRIP. Instead, it appears the decrease in signal strength at 15 ka bp correlates with the increase in temperature and isotopes at the start of the Bølling Allerød.

An alternative method of showing the 60% reduction in strength of climate variability across all high frequencies (interannual and decadal) is to compare the diffusion corrected spectra of the climate states occurring directly before and after this shift (Figure 3.12). We analyze 9,000 year timeframes representative of the LGM (21-30 ka bp) and Holocene (1-10 ka bp) and calculate the power density ratio of the glacial relative to the interglacial. Taking the square root of this ratio, consistent with Equation 16 in Section 2.4, yields a relative ratio of 1.6. In other words, all interannual and decadal frequencies during the timeframe 21-30 ka bp are approximately 60% greater in amplitude than those during the 1-10 ka bp period.

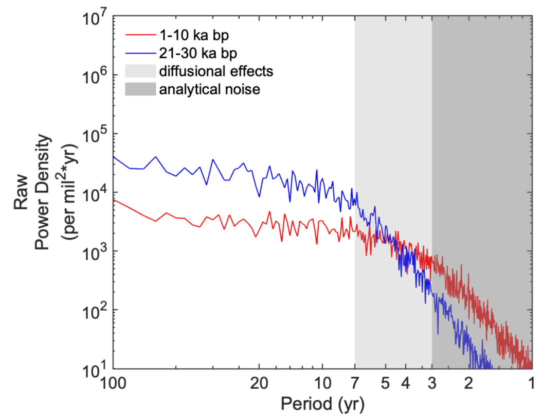

Figure 3.8: Comparison of raw LGM (blue; 21-30 ka bp) and Holocene (red; 1-10 ka bp) PSD functions

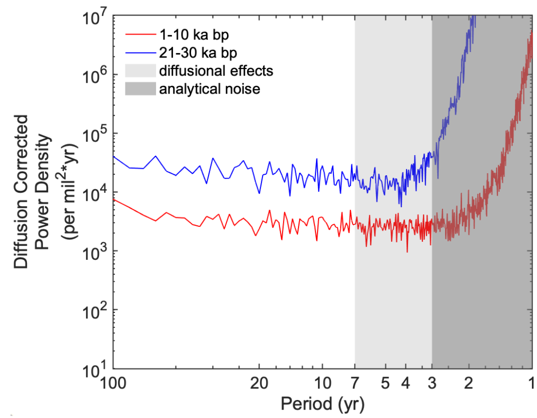

Figure 3.9: Comparison of diffusion-corrected LGM (blue; 21-30 ka bp) and Holocene (red; 1-10 ka bp) PSD functions

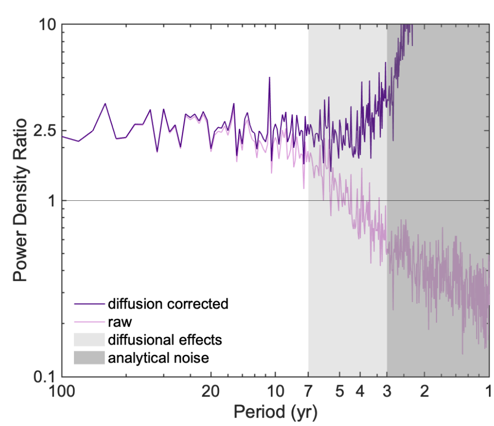

Figure 3.10: Ratio of LGM diffusion-corrected PSD relative to Holocene diffusion-corrected PSD; on average, all frequencies during the LGP exhibit 2.5 times greater variabilty compared to the Holocene

3.1.4. EGRIP Non-Diffusion-Corrected Results

Without the diffusion correction, our results would look much different. The non-diffusion corrected results only show a 60% reduction in the strength of the 15-20 and 20-30 year bands. Attenuation from diffusion among the 4-15 year bands causes varying underestimations of relative amplitude. Here, we show how important the diffusion correction is for interpreting high-frequency climate variability in polar ice cores.

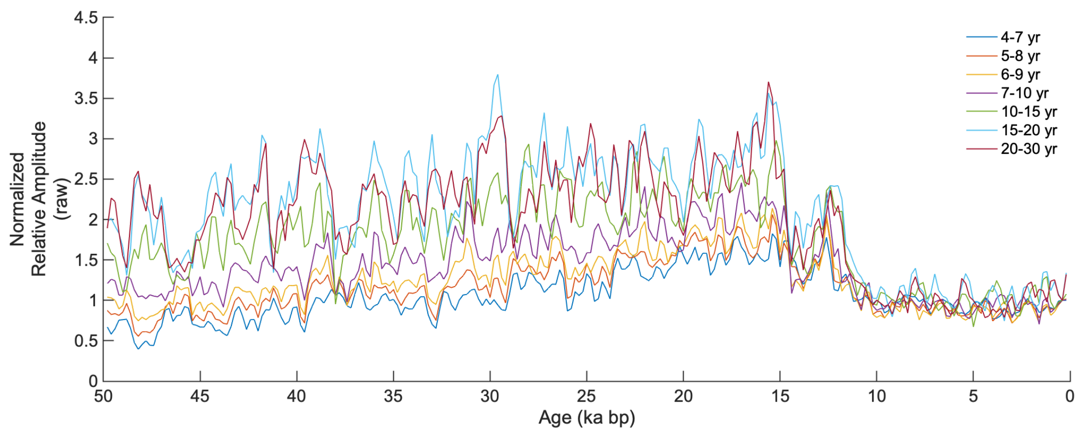

Figure 3.11: Non-diffusion-corrected strength of high-frequency climate variability at EGRIP (northeastern Greenland); analysis done in 400 year windows with a timestep of 200 years

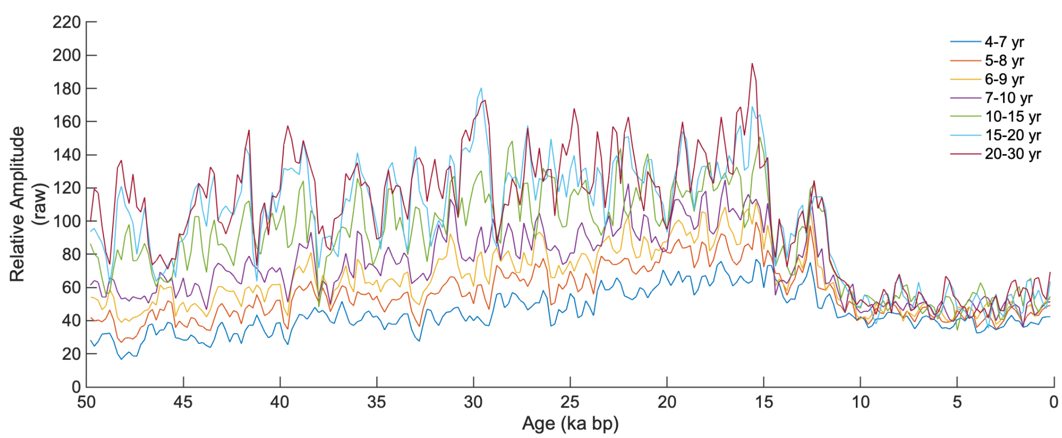

Figure 3.12:Non-diffusion-corrected strength of high-frequency climate variability at EGRIP (northeastern Greenland) normalized to modern conditions (i.e. 400 years bp); analysis done in 400 year windows with a timestep of 200 years

3.1.5. EGRIP Uncertainty

Next, we aim to understand how reliable our interpretation of climate variability is by evaluating amplitude uncertainty for frequency bands of interest. For each 400 year window in the EGRIP record, we convert our original spectra to the natural log of power density vs frequency squared and fit a linear regression (solid red line in Figure 3.13) using a least squares method to the diffused interval. This step mimics the Gaussian fit described in Section 2.4. Uncertainty bounds are determined by creating maximum and minimum slopes (dashed green lines in Figure 3.13) between +/- one standard deviation of the linear regression (dashed red lines in Figure 3.13). These slopes represent the largest and smallest diffusion lengths within one standard deviation of our regression for that window. Finally, we use these slope values in our diffusion correction and quantification of signal strength (Section 2.4) equations to determine amplitude uncertainty bounds for interannual and decadal frequency bands (e.g. 4-7, 5-8, 6-9, 10-15, 15-20, and 20-30 year signals) through time.

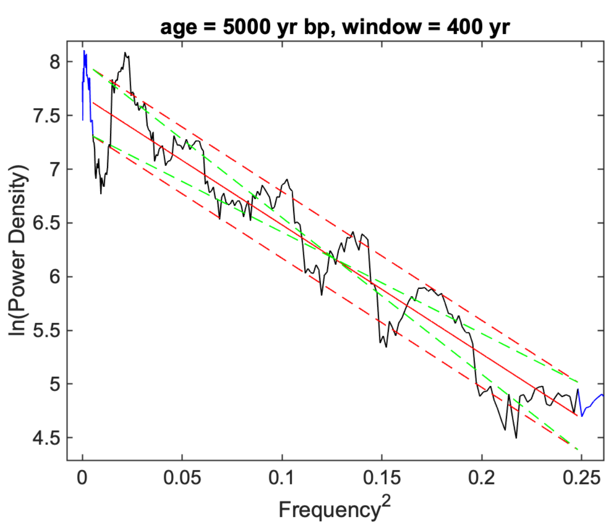

Figure 3.13: Example of uncertanity estimate determined by fitting a linear regression to the ln(power density) vs frequency^2 for each 400 year window;

Uncertainty is negligible for all frequency bands during the Holocene which allows us to confidently interpret high-frequency climate variability on both interannual and decadal scales during this timeframe. During the LGP, there is increased uncertainty in estimates of relative strength for the 4-7 year band and little to no uncertainty for the 10-15, 15-20 and 20-30 year bands. Despite this, the magnitude of uncertainty is small relative to the magnitude of high-frequency climate variability fluctuations across the glacial-interglacial transition and millennial scale Dansgaard-Oeschger (DO) events. Thus, we also feel confident in interpreting interannual and decadal scale climate variability during the Last Glacial Period (LGP).

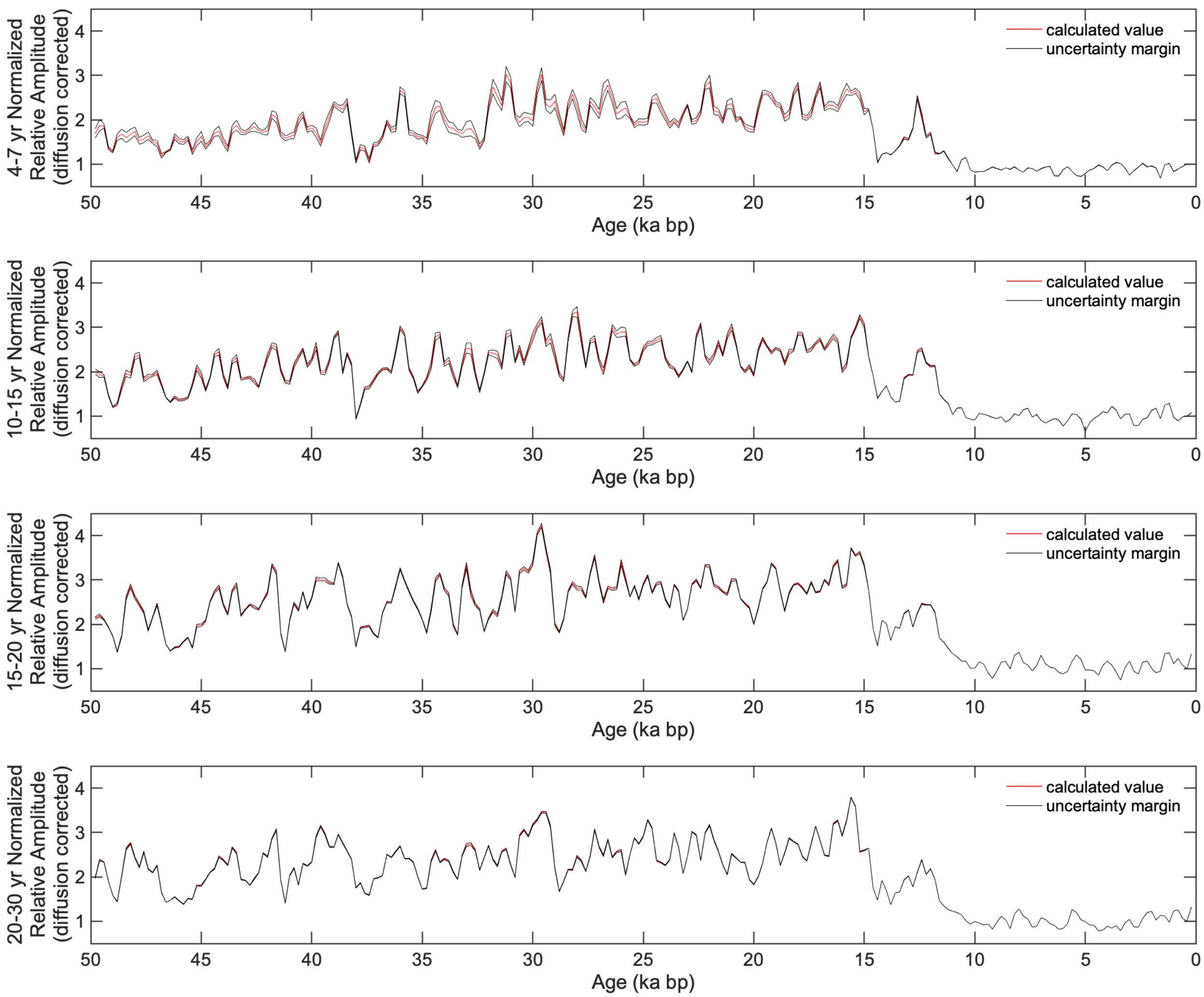

Figure 3.14: Uncertainty estimates for the 4-7, 10-15, 15-20 and 20-30 year bands at EGRIP; all bands show little uncertainty in the Holocene; greatest uncertainty in the LGP occurs among the 4-7 year band but still allows for interpretation of interannual climate variability throughout millennial scale transitions

Event	Start (yr BP)	End (yr BP)	Duration (yr)
Holocene	11,703	0	11,703
GS-1 (Younger Dryas)	12,896	11,703	1,193
GI-1 (Bølling-Allerød)	14,692	12,896	1,796
GS-2.1	22,900	14,692	8,208
GI-2.1	23,020	22,900	120
GS-2.2	23,200	23,020	180
GI-2.2	23,340	23,200	140
GS-3	27,540	23,340	4,200
GI-3	27,780	27,540	240
GS-4	28,600	27,780	820
GI-4	28,900	28,600	300
GS-5.1	30,600	28,900	1,700
GI-5.1	30,840	30,600	240
GS-5.2	32,040	30,840	1,200
GI-5.2	32,500	32,040	460
GS-6	33,360	32,500	860
GI-6	33,740	33,360	380
GS-7	34,740	33,740	1,000
GI-7	35,480	34,740	740
GS-8	36,580	35,480	1,100
GI-8	38,220	36,580	1,640
GS-9	39,900	38,220	1,680
GI-9	40,160	39,900	260
GS-10	40,800	40,160	640
GI-10	41,460	40,800	660
GS-11	42,240	41,460	780
GI-11	43,340	42,240	1,100
GS-12	44,280	43,340	940
GI-12	46,860	44,280	2,580
GS-13	48,340	46,860	1,480
GI-13	49,280	48,340	940
GS-14	49,600	49,280	320
GI-14	51,500	49,600	1,900

Table 3.1: Chronology of Greenland stadial (GS) periods and interstadial (GI) periods throughout the past 50 ka (Rasmussen et al., 2014)

3.1.6. EGRIP Millennial Scale Dansgaard-Oeschger (DO) Event Analysis

Now we switch our focus to how the strength of high-frequency climate variability evolved over the course of millennial scale interstadial (i.e. DO) events in Greenland. Above is a reference table of the interstadial periods (denoted as 'GS' and colored red) and stadial periods (denoted as 'GI' and colored blue) that punctuated the Last Glacial Period to 50 ka bp (Rasmussen et al., 2014). As in the glacial-interglacial comparison, we are similarly interested in understanding if mean temperature change during stadial-interstadial transitions resulted in changes to high-frequency climate variability.

We isolate 400 year windows at the onset of both warming (interstadial) and cooling (stadial) events in Greenland, consistent with the timing of these events given in Buizert et al. (2015a), and calculate the diffusion corrected relative strength of various high-frequency bands (e.g. 7-10, 10-15, 15-20 and 20-30) for each window. Because many DO events in the late glacial period (15-32 ka bp) are shorter than 400 years, we cannot use them in this analysis and instead focus on interstadial events that occur between 32 and 50 ka bp. Specifically, these are DO events 5.2-14. The sole interstadial that is shorter than our ideal window size of 400 years is DO 9 (duration of 260 years) which will cause results from this event to be skewed toward the background glacial state.

We find a striking pattern at EGRIP. By and large, Greenland interstadial periods exhibit lower climate variability than stadial counterparts in almost all cases. The 7-10 year band shows a 25% margin between stadial and interstadial amplitudes while the 10-15, 15-20 and 20-30 year bands show a 50% margin, on average. Additionally, stadial periods in the decadal range (i.e. 10-15, 15-20 and 20-30 year bands) always exhibit higher variability than interstadial periods. The only excursion from this pattern occurs during the DO 9 window which, as stated above, is weighted to the background glacial climate state. Later, we investigate whether this trend (that warm periods are characterized by lower high-frequency climate variability) is also evident in Antarctic millennial scale AIM events.

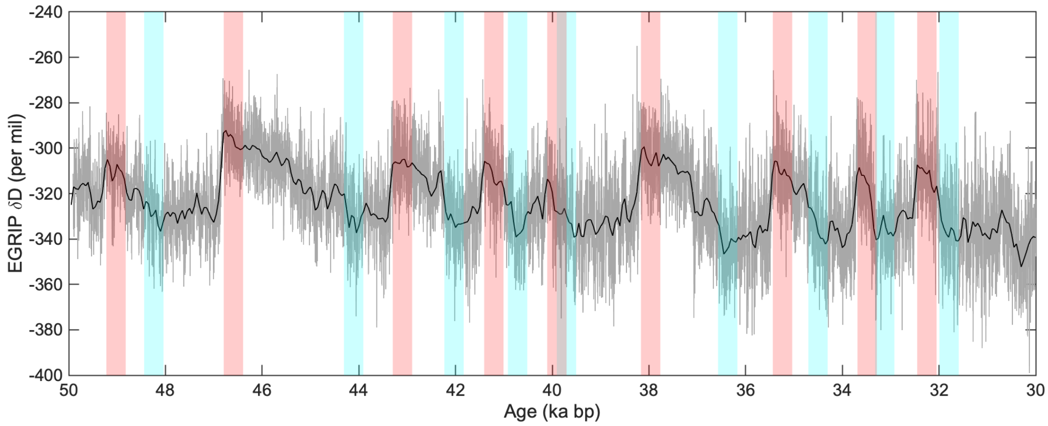

Figure 3.15: Raw EGRIP δD record (light grey) overlaid with moving average (black) for 30-50 ka bp; red shaded areas indicate 400 year window at start of warming (i.e. interstadial) period while blue shaded areas indicate 400 year window at start of cooling (i.e. stadial) period

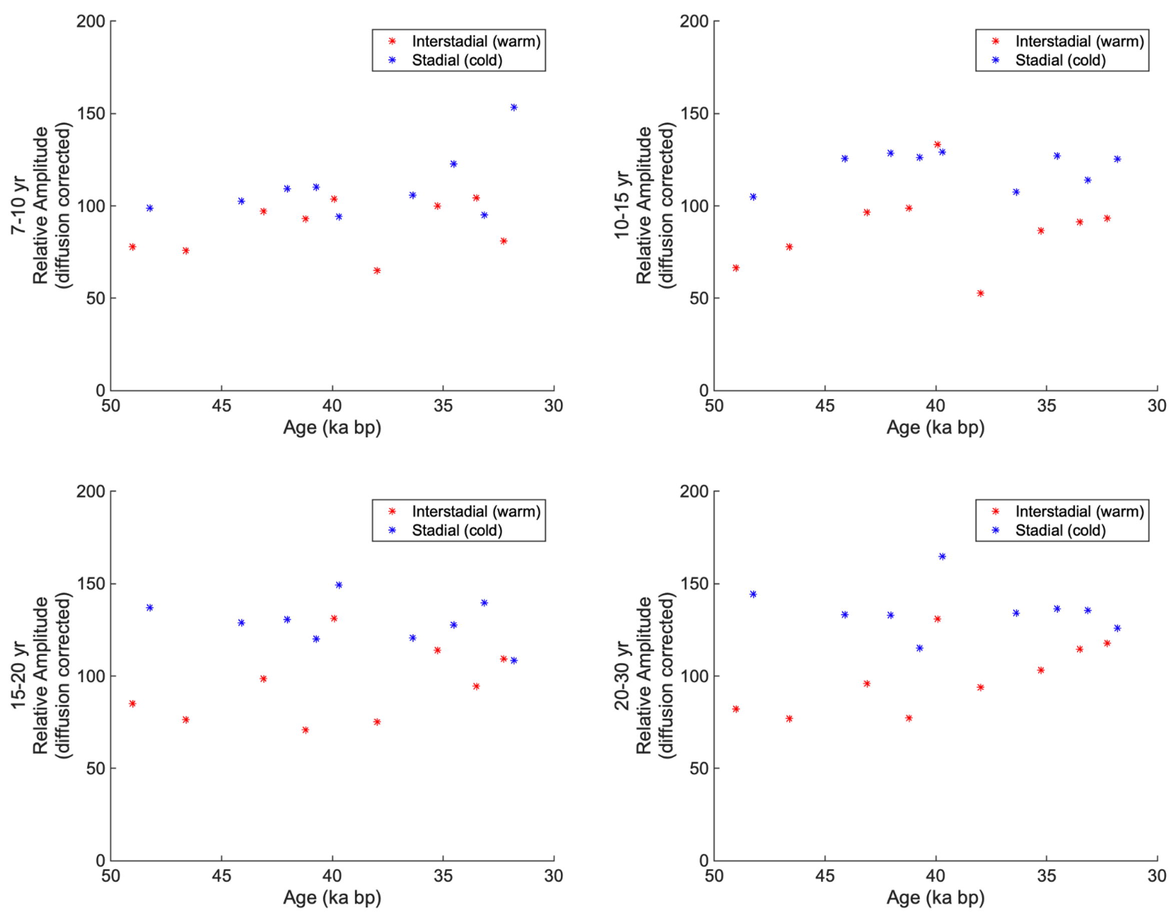

Figure 3.16: Relative strength of EGRIP high-frequency climate variabilty for the interstadial (red dots) and stadial (blue dots) periods outlined in Figure 3.15

After establishing a strong relationship between the strength of high-frequency climate signals and millennial scale events in Greenland, we perform a higher resolution analysis to further elucidate precise changes in climate variability during stadial-interstadial transitions. Specifically, we are interested in determining if changes in high-frequency variability occur as abruptly as Dansgaard-Oeschger (DO) temperature shifts and how these two variables (mean temperature and variability around mean temperature) move in relation to one another. We use 400 year windows with a sliding timestep of 50 years from 10-50 ka bp at EGRIP. This analysis encompasses DO events 1 through 13. In the plots below, dark red vertical lines designate the DO Event abrupt warming while light red intervals represent the entire subsequent interstadial period, as defined in Rasmussen et al. (2014). Data points represent diffusion corrected relative amplitudes for each frequency band.

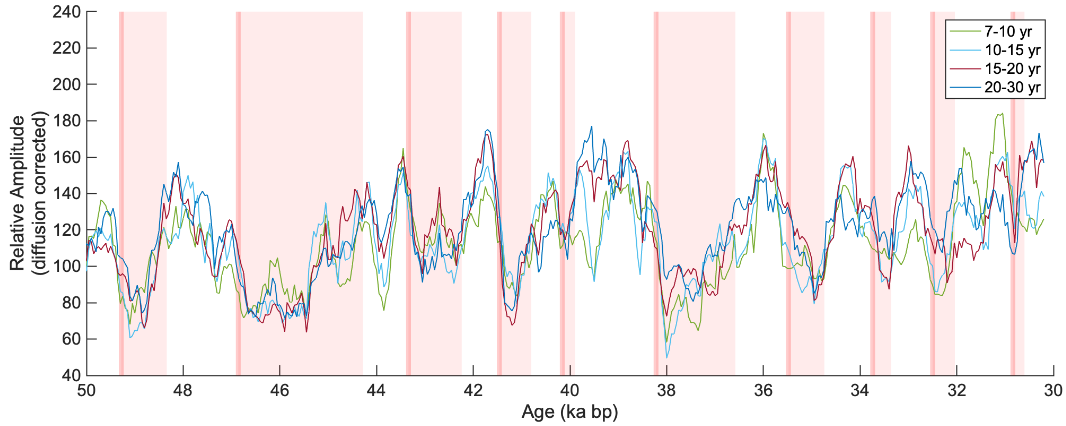

Figure 3.17: High resolution (i.e. 400 year window; 50 year timestep) analysis of high-frequency climate variability at EGRIP for DO events 5.1-13

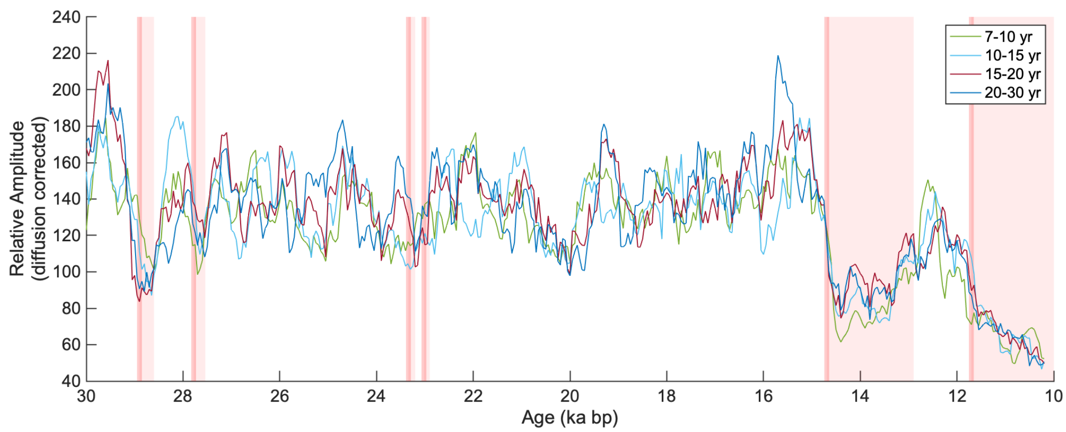

Figure 3.18: High resolution (i.e. 400 year window; 50 year timestep) analysis of high-frequency climate variability at EGRIP for DO events 1-4

Approximately 0.5-1 ka prior to abrupt warming, variability begins to decrease from maximum levels and remains low through about the first half of each interstadial period. Relative strength more rapidly increases during the last half of the interstadial and continues increasing until maximum variability is reached approximately halfway through each stadial. Although this cycle is evident for most DO events, exceptions do exist (e.g. DO 8 and 12). Thus, we cannot definitively say there is a common pattern that holds for all events, but there are many commonalities. In general, the strength of climate variability in Greenland tracks with background temperature, as indicated by this analysis.

3.2. Interhemispheric Comparisons

3.2.1. WDC and SPC Diffusion-Corrected Results

Now we aim to understand how findings from northeast Greenland compare to those from both East and West Antarctica. First, we establish general trends in climate variability for both Antarctic locations to 50 ka bp. This analysis was performed as described in Methods sections 2.1-2.4 for 400 year windows with a timestep of 200 years. It is important to note that the scale on the following plots is different than the one from our EGRIP results.

Prior spectral analysis of the WDC water isotope record shows a 50% reduction in the strength of interannual and decadal signals (e.g. 3-7 & 4-15 year bands) at 16.2 ka bp (Jones et al., 2018b). Climate model simulations attribute this shift to an increase in teleconnection between the tropical Pacific Basin and West Antarctica, ultimately forced by a reduction in the size of the Laurentide Ice Sheet. In this study, we corroborate the 16.2 ka signal among the 4-7, 5-8, 6-9, 7-10 and 10-15 year bands. We also find that the signal is less pronounced among the 15-20 and 20-30 year bands relative to the modern.

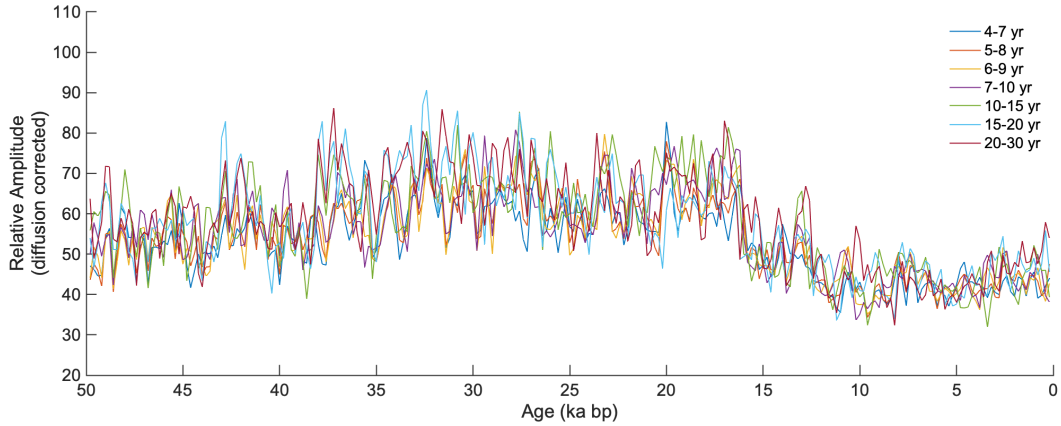

Figure 3.19: Diffusion-corrected strength of high-frequency climate variability at WDC (West Antarctica); analysis done in 400 year windows with a timestep of 200 years

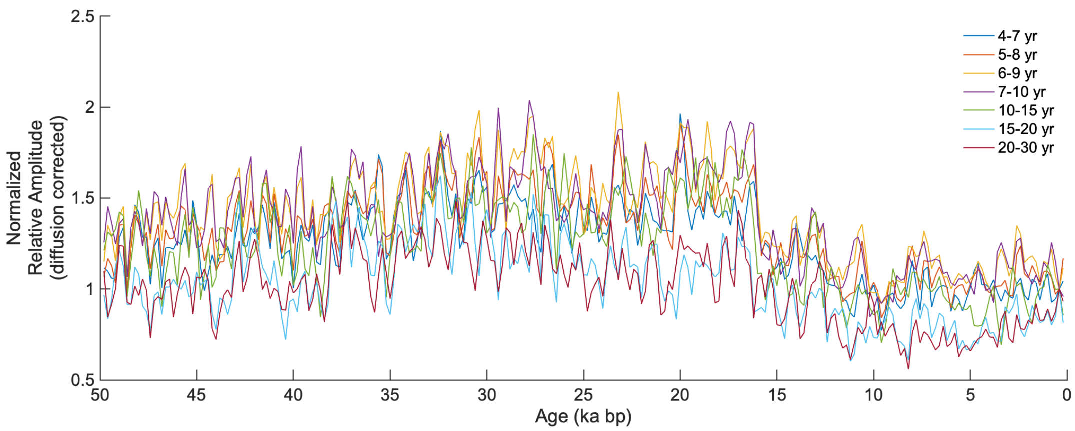

Figure 3.20: Diffusion-corrected strength of high-frequency climate variability at WDC (West Antarctica) normalized to modern conditions (i.e. 400 years bp); analysis done in 400 year windows with a timestep of 200 years

Our results from SPC are substantially different. We find little in the strength of high-frequency climate signals throughout the last 50 ka bp. There is potentially a slight decrease around 11 ka but data noise makes it difficult to definitively confirm any shift.

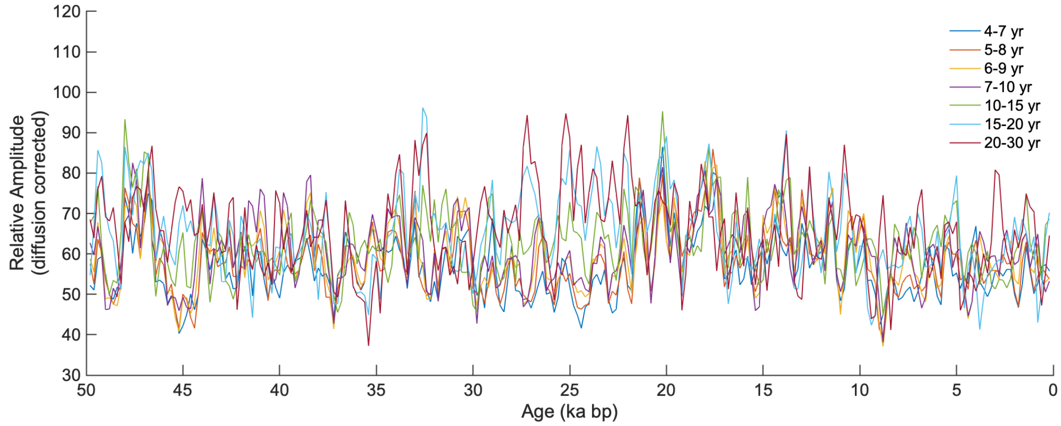

Figure 3.21: Diffusion-corrected strength of high-frequency climate variability at SPC (East Antarctica); analysis done in 400 year windows with a timestep of 200 years

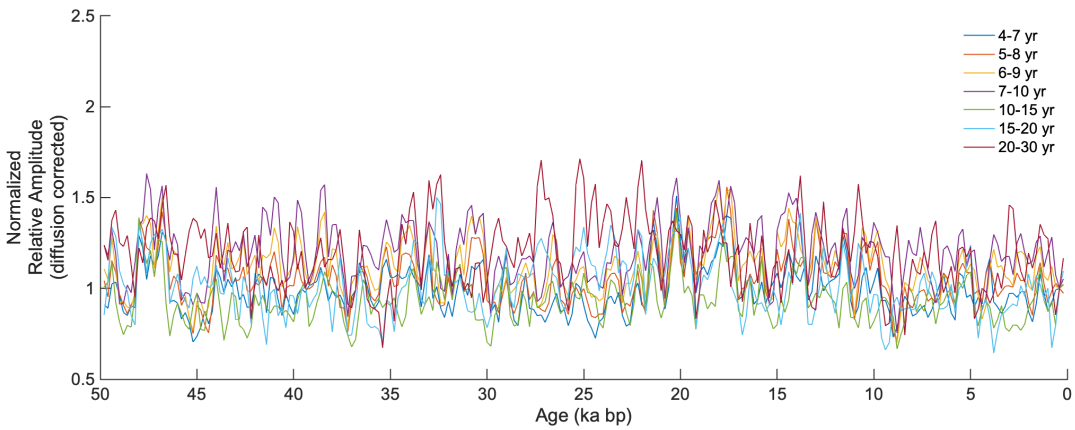

Figure 3.22: Diffusion-corrected strength of high-frequency climate variability at SPC (East Antarctica) normalized to modern conditions (i.e. 400 years bp); analysis done in 400 year windows with a timestep of 200 years

3.2.2. Interhemispheric Ratios of High-Frequency Climate Variability

Next, we compare the strength of high-frequency signals at EGRIP, WDC and SPC on the same scale to better understand geographically driven climatology. We analyze the interannual (7-10 year) and decadal (10-15 year) bands only. Each data point represents non-normalized diffusion corrected amplitude of climate variability.

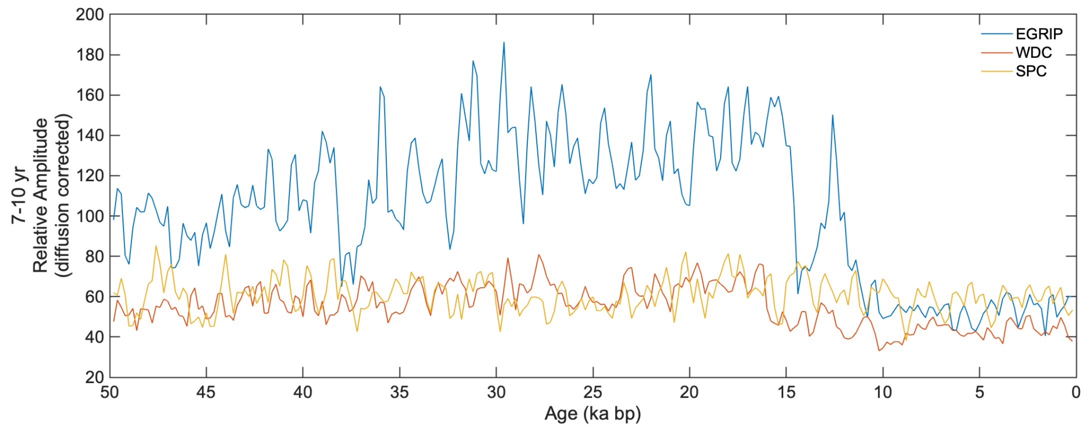

Figure 3.23: Non-normalized strength of interannual (i.e. 7-10) year band for EGRIP, WDC, and SPC from 0-50 ka bp

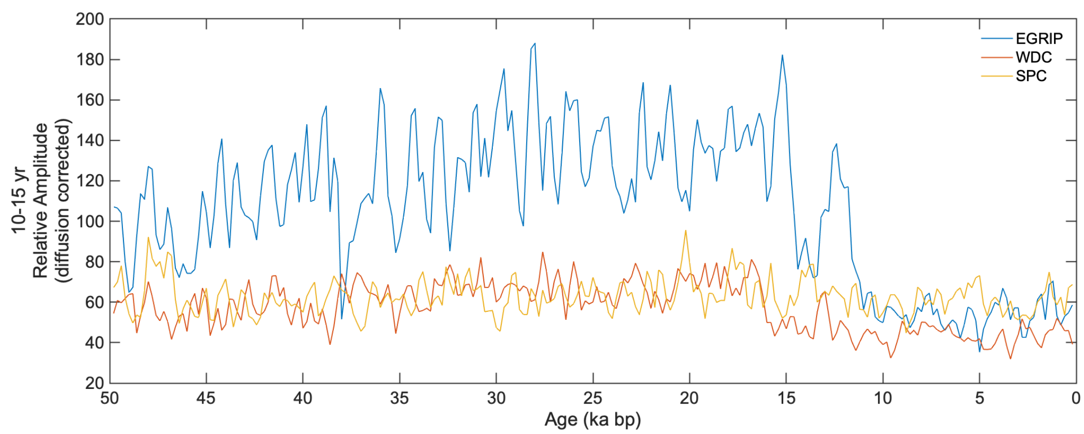

Figure 3.24: Non-normalized strength of decadal (i.e. 10-15) year band for EGRIP, WDC, and SPC from 0-50 ka bp

From this comparison, we identify a substantial difference in the strength of high-frequency climate variability between the northern and southern hemisphere, especially during the last glacial period (LGP). From visual inspection, WDC and SPC exhibit similar climate variability conditions throughout the glacial period but diverge slightly during the Holocene. Conversely, climate variability at EGRIP is significantly stronger during the glacial period but drops to levels comparable to SPC during the Holocene.

We quantify these differences in climate variability by calculating the ratio of non-normalized relative amplitudes for combinations of locations. The general form of this calculation takes the form:

$$R_{A-B} = \frac{site\ A\ relative\ amplitude\ (i)}{site\ B\ relative\ amplitude\ (i)} \tag{17}$$

where $R_{A\text{-}B}$ stands for ratio of site A relative to site B and i means index. A ratio of 1 suggests equal strength of climate variability for the two sites analyzed. A ratio greater than 1 suggests stronger variability for site A and vice versa. Table 3.2 describes average ratios for the LGP and Holocene while Figure 3.25 shows the temporal evolution of ratios throughout the past 50 ka bp. EGRIP exhibits climate variability 2-times stronger than both WDC and SPC during the glacial period. In the Holocene, EGRIP exhibits the same climate variability as SPC, but slightly (1.3-times) greater variability than WDC.

	Glacial Relative Amplitude Ratio	Holocene Relative Amplitude Ratio
$R_{EGRIP\text{-}WDC}$	2	1.2
$R_{EGRIP\text{-}SPC}$	2	1
$R_{WDC\text{-}SPC}$	1	0.8

Table 3.2: Average non-normalized interannual and decadal amplitude ratios (isotope domain)

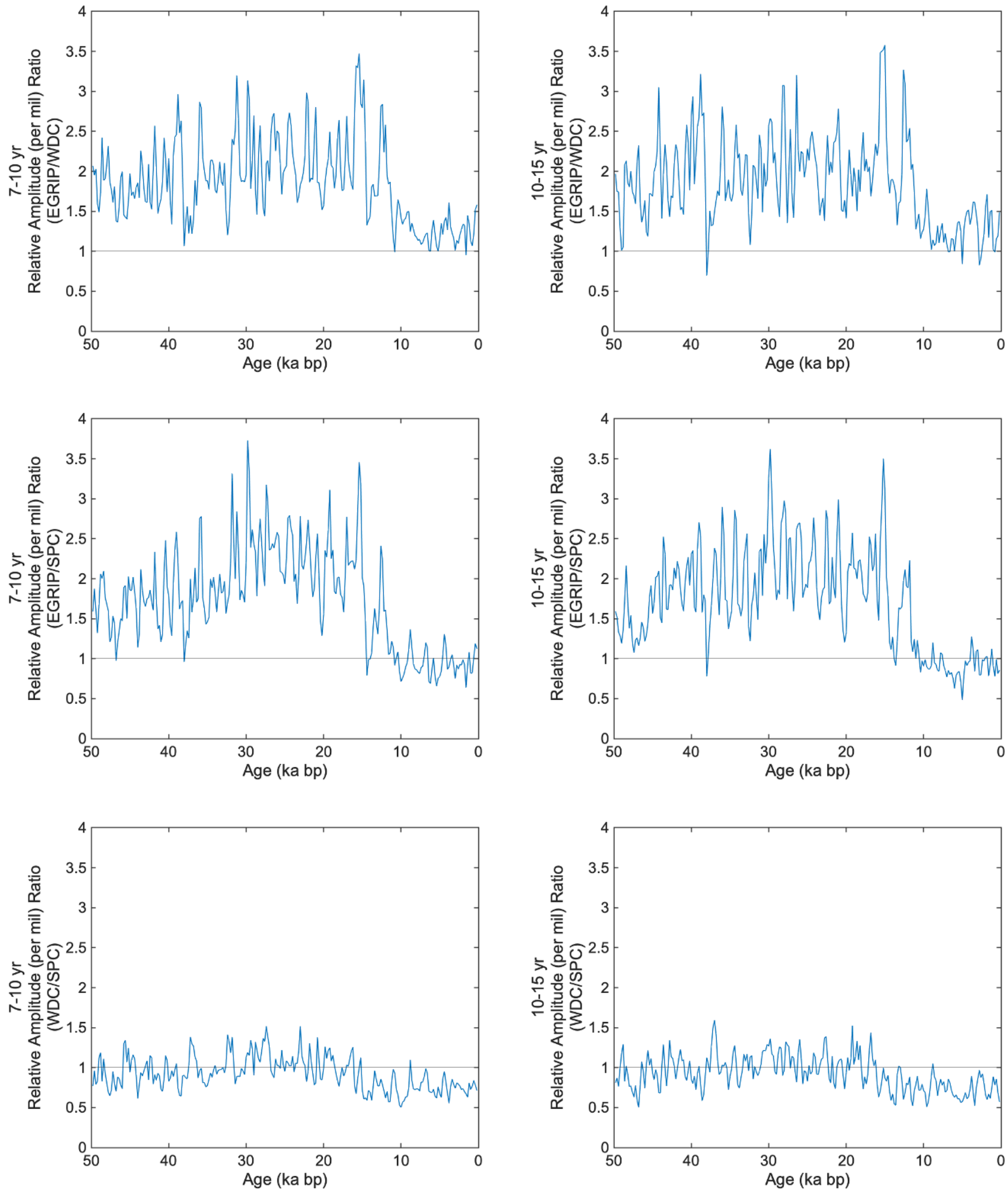

Figure 3.25: Temporal evolution of non-normalized interannual and decadal amplitude ratios (isotope domain)

The ratios described above were calculated based on the strength of climate variability inferred from diffusion corrected water isotope records. As explained in Section 1.6, the water isotope record is a proxy for temperature, but the rate at which isotopes and temperature scale changes spatially. For instance, a change of 40 per mil δD during the Holocene in central Greenland may translate to a temperature increase of approximately 10 degrees C, but a similar change in isotopes at the South Pole does not equate to the same degree of warming. Additionally, isotope and temperature may scale at different rates throughout time for the same location due to a variety of factors (e.g. seasonality of precipitation, cloud properties, etc.) (Cuffey, 2016). Therefore, the ratios calculated above are not necessarily representative of the relationship between northern and southern hemisphere temperature variability.

To correct for these inconsistencies, we calculate updated ratios based on site specific isotope-temperature scales, outlined below:

	Glacial Isotope-Temperature Scale (‰D/°C)	Holocene Isotope-Temperature Scale (‰D/°C)
EGRIP+	4.2	6.4
WDC++	8.3	8.3
SPC+++	7.9	7.9

Table 3.3: Site specific isotope-temperature scales for EGRIP, WDC and SPC

+Kindler et al., 2014
++Markle & Steig in review, 2021
+++Kahle in review, 2021

The above scales use a combination of water isotope analysis, firn modeling and borehole thermometry to reconstruct how temperature changed in relation to δD and δ18O signatures identified in ice cores. Antarctic scales do not change substantially from the last glacial to the Holocene, but those in Greenland do. For EGRIP, we use the Holocene scale for 0-11.6 ka bp and the glacial scale for 11.6-50 ka bp. The general form of this new calculation takes the form:

$$R_{A-B} = \frac{site\ A\ relative\ amplitude\ (i)/S_A}{site\ B\ relative\ amplitude\ (i)/S_B} \tag{18}$$

where S_A and S_B represent the isotope-temperature scales for site A and B, respectively. Updated average ratios are found in Table 3.4 while the ratio timeseries are found in Figure 3.26.

	Glacial Relative Amplitude Ratio w/ Isotope-Temp Scale	Holocene Relative Amplitude Ratio w/ Isotope-Temp Scale
EGRIP/WDC	4.5	1.5
EGRIP/SPC	4.5	1
WDC/SPC	1	0.7

Table 3.4: Average non-normalized interannual and decadal amplitude ratios (temperature domain)

We show that EGRIP experienced 4.5 times greater temperature variability during the last glacial period than both SPC and WDC, which exhibit comparable conditions. During the Holocene, EGRIP exhibits comparable variability to SPC, but is slightly more (1.5 times) variable than WDC.

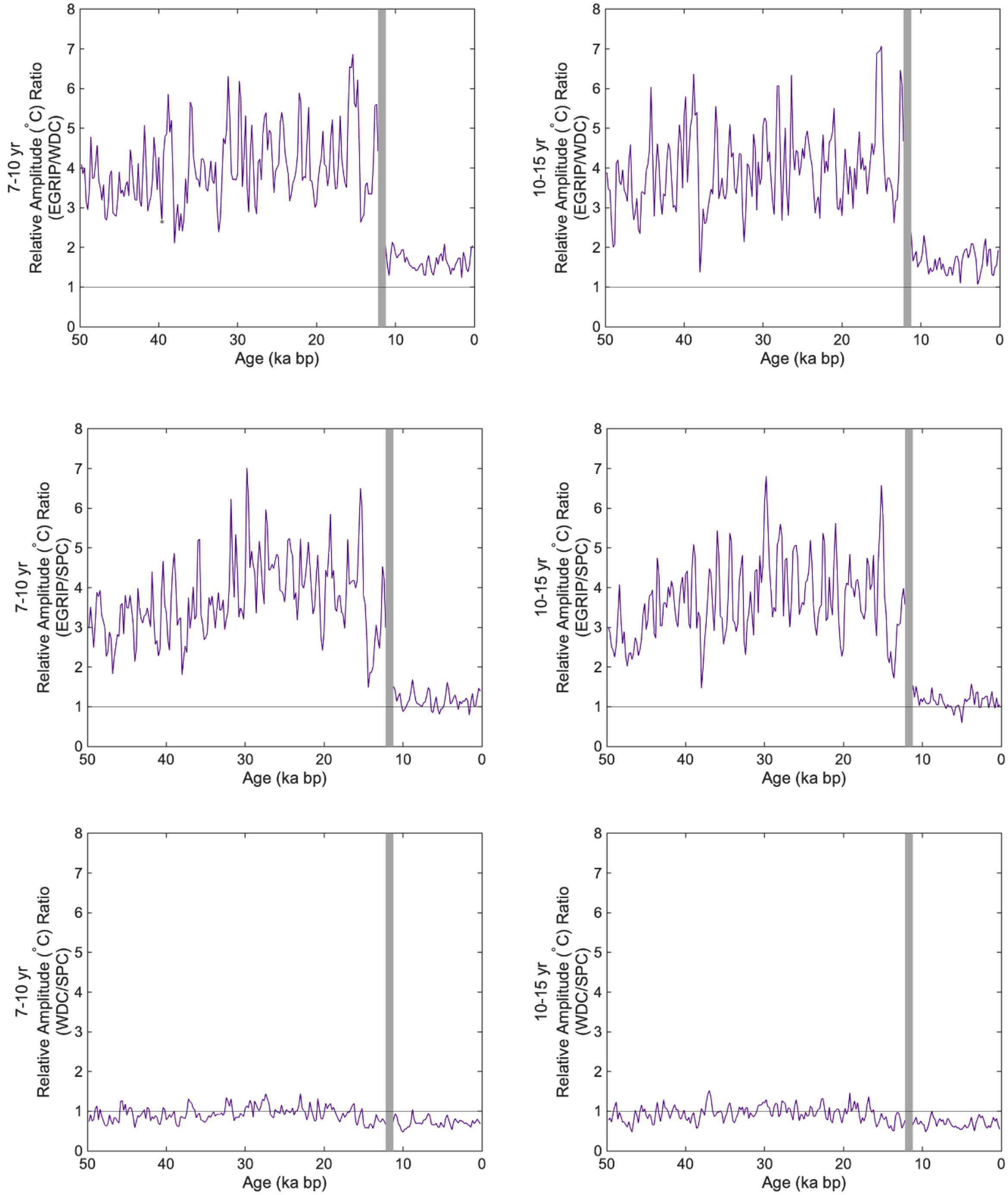

Figure 3.26: Temporal evolution of non-normalized interannual and decadal amplitude ratios (isotope domain)

3.2.3. WDC and SPC Millennial Scale Antarctic Isotope Maxima (AIM) Event Analysis

Next, we analyze how high-frequency climate variability changed across millennial scale AIM and non-AIM periods in Antarctica. As established above, EGRIP exhibits lower variability during warm interstadial periods and greater variability during cold stadial periods. We want to determine whether this trend is specific to northeastern Greenland or also evident at SPC and WDC.

Due to the heat transport mechanism known as the bi-polar seesaw, DO events in the northern hemisphere are in antiphase with AIM events in the southern hemisphere. By synchronizing the WDC and NGRIP water isotope records using high-resolution methane measurements, Buizert et al. (2015b) determined that Greenland warming precedes Antarctic cooling by 218 +/- 92 years while Greenland cooling precedes Antarctic warming by 208 +/- 96 years. We use this chronology to determine 400 year Antarctica cooling and warming windows based off of our EGRIP DO analysis in Section 3.1.6. Specifically, we subtract 218 +/- 92 years or 208 +/- 96 years from the onset of Northern Hemisphere cooling and warming phases outlined in Buizert et al. (2015a) to determine Antarctic warming and cooling phases, respectively.

In contrast to our EGRIP results, there is no relationship between the strength of high-frequency climate variability and the timing of warm (i.e. AIM) and cool (i.e. non-AIM) phases in both East and West Antarctica. This result is evident among all frequency bands analyzed.

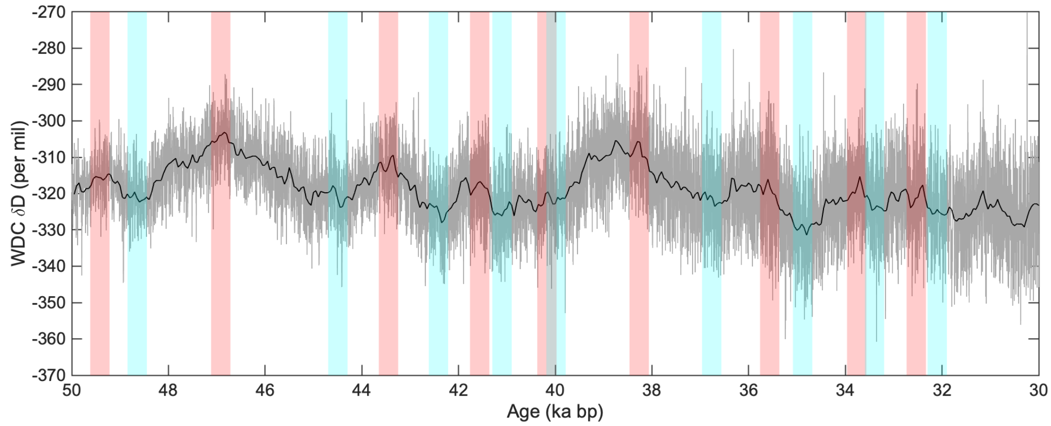

Figure 3.27: Raw WDC δD record (light grey) overlaid with moving average (black) for 30-50 ka bp; red shaded areas indicate 400 year window during warm (i.e. AIM) period while blue shaded areas indicate 400 year window during cold (i.e. non-AIM) period

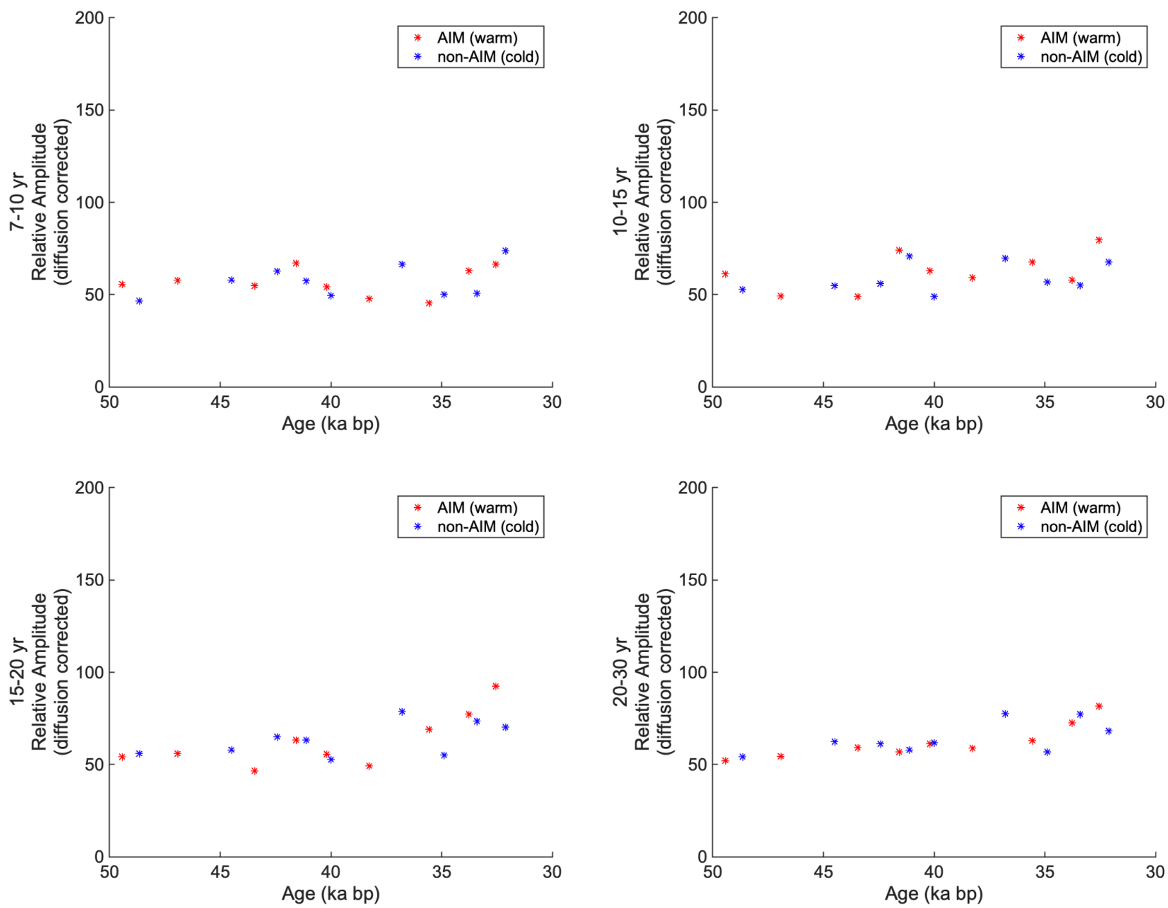

Figure 3.28: Relative strength of WDC high-frequency climate variabilty for the AIM (red dots) and non-AIM (blue dots) periods outlined in Figure 3.15

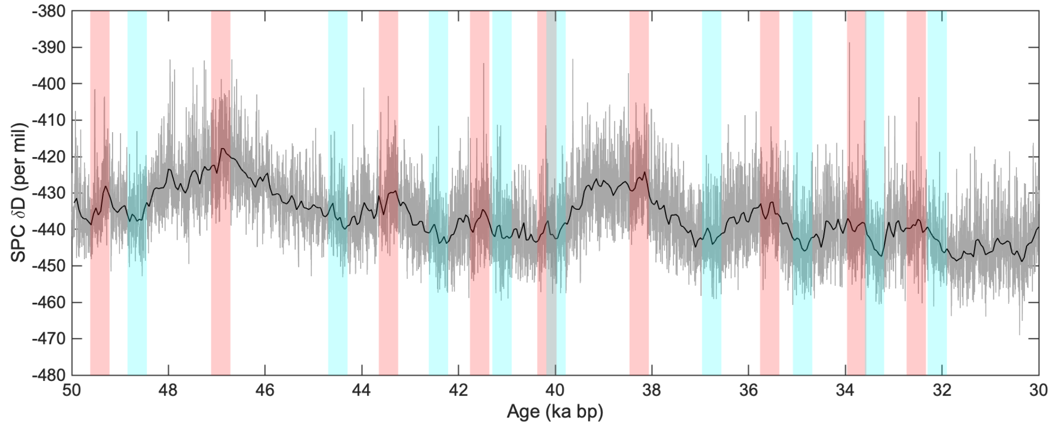

Figure 3.29: Raw SPC δD record (light grey) overlaid with moving average (black) for 30-50 ka bp; red shaded areas indicate 400 year window during warm (i.e. AIM) period while blue shaded areas indicate 400 year window during cold (i.e. non-AIM) period

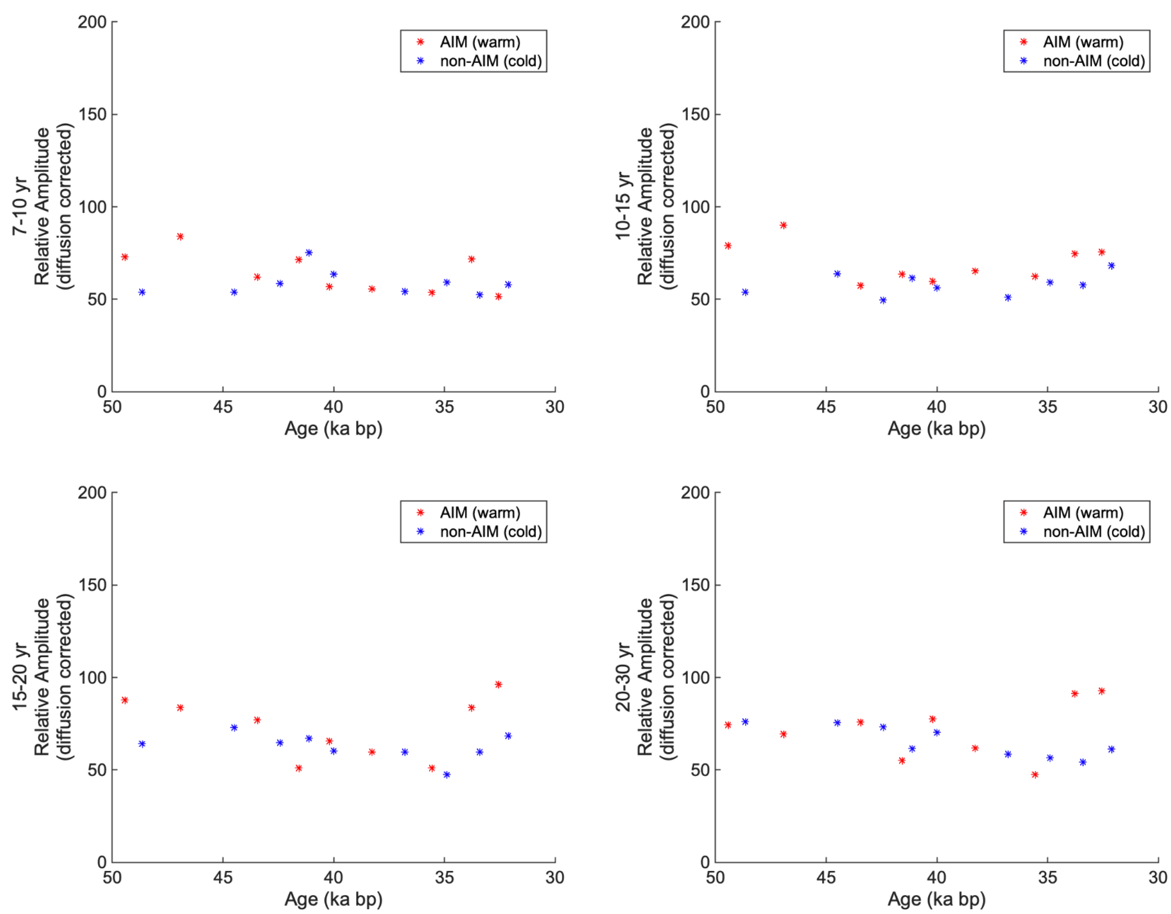

Figure 3.30: Relative strength of SPC high-frequency climate variabilty for the AIM (red dots) and non-AIM (blue dots) periods outlined in Figure 3.15

3.2.4. Interhemispheric Trends in High-Frequency Climate Variability

Finally, we are motivated to understand how the background climate state affects climate variability across all three study sites. We use the water isotope record as an estimate of background temperature (because temperature reconstructions are not yet available for EGRIP) and compare this to our records of normalized high-frequency climate variability (7-10, 10-15 and 20-30 year bands). We distinguish climate states by grouping data in five timeframes:

- Holocene: 0-11.7 ka bp
- Younger-Dryas: 11.7-12.9 ka bp
- Bølling Allerød: 12.9-14.7 ka bp
- Northern Hemisphere interstadial periods: consistent with Rasmussen et al. (2014)
- Northern Hemisphere stadial periods: consistent with Rasmussen et al. (2014)

In this analysis, water isotopes (i.e. temperature) are plotted on the x-axis as the independent variable and normalized relative amplitudes are plotted on the y-axis as the dependent variable. Essentially, this analysis compares mean temperature to high-frequency climate variability around the mean in 400 year windows for each location. Once plotted, we fit a linear regression to the data to determine r^2 (which measures variance explained by the model) and p values (which determine if results are statistically significant) for each site. A high r^2 value (>0.7) means the model explains a super majority of observations while a low p value (<0.05) means the observations effectively reject the null hypothesis, which states there is no relationship between the variables being compared. For our purposes, high r^2 and low p values infer that strength of high-frequency climate variability relates to the background climate state, and vice versa.

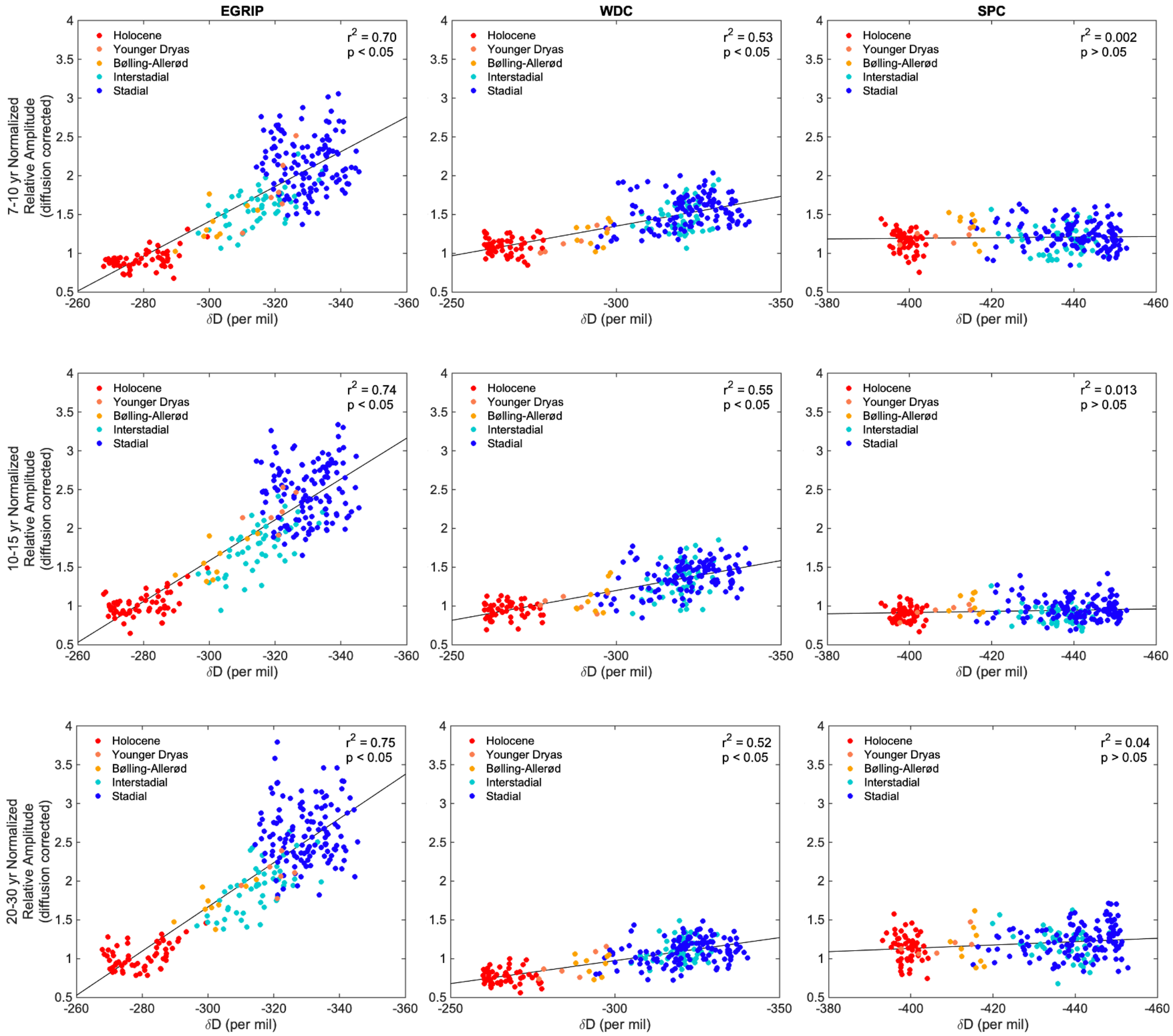

Figure 3.31: Relationship between mean temperature and variability around mean temperature for EGRIP, WDC and SPC; data is grouped by Holocene (red), Younger Dryas (pink), Bølling-Allerød (orange), NH interstadial periods (light blue) and NH stadial periods (dark blue).

	Average R^2 value	P value
EGRIP	0.73	<0.05
WDC	0.53	<0.05
SPC	0.018	>0.05

Table 3.5: Average R^2 and P values from Figure 3.31 for EGRIP, WDC and SPC

We find a strong relationship between climate variability and mean temperature at EGRIP ($r^2 = 0.73$), a mild relationship at WDC ($r^2 = 0.53$) and essentially no relationship at SPC ($r^2 = 0.018$). These results suggest high-frequency climate variability in Greenland is strongly coupled with mean temperature while Antarctic high-frequency climate variability is largely independent of temperature change.

Another way to visualize the plots in Figure 3.31 is to create Probability Density Functions (PDFs) for each cluster of data (i.e. Holocene, deglaciation, interstadial and stadial periods). This approach displays how much climate variability deviates from mean variability during each timeframe for all three locations. EGRIP exhibits relatively little deviation from mean conditions during the Holocene and significantly greater deviation during the Last Glacial Period (LGP). WDC exhibits a similar trend to EGRIP, in that deviation from mean conditions is greater during the LGP, but the magnitude of dispersion is smaller for both the Holocene and LGP compared to EGRIP. SPC exhibits little to no change in deviation from mean conditions from the Holocene to the LGP, thus making it the most stable site.

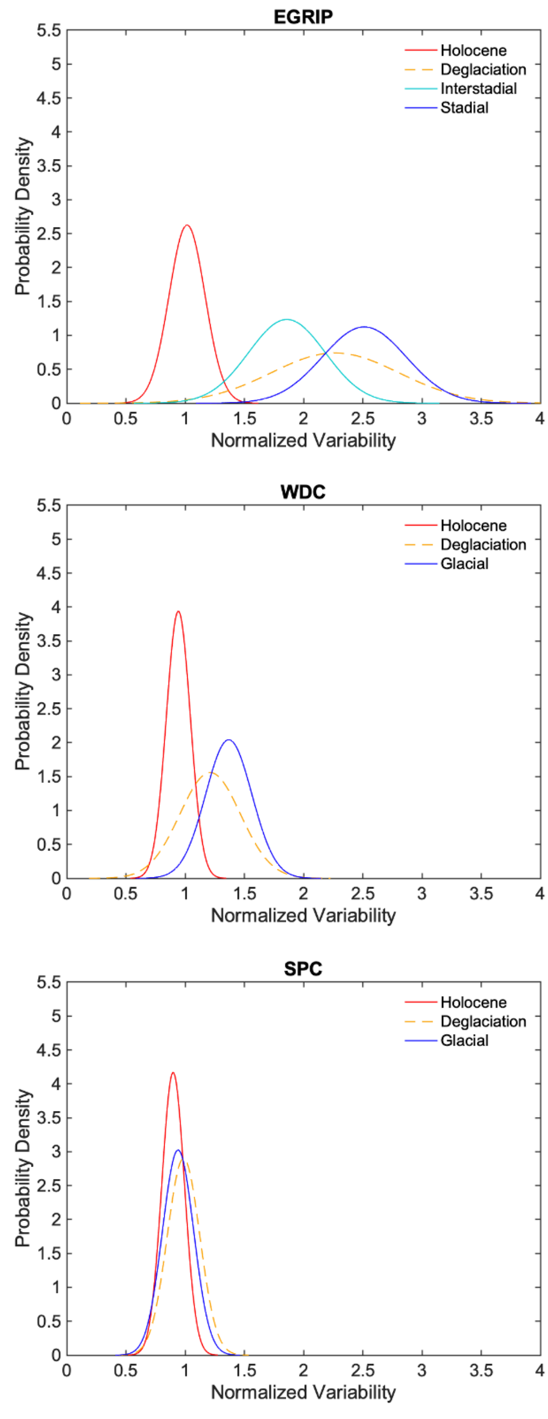

Figure 3.32: PDFs of Holocene (red) and LGP (blue) data groupings from Figure 3.31; greater spread across x-axis indicates increased deviation from mean climate variability conditions

Chapter 4: DISCUSSION

4.1. Misconceptions about Climate Variability

Climate variability research focuses on anomalies occurring beyond the scale of single weather events and broadly speaking, attempts to quantify deviation from the mean state of a climatic record (e.g. temperature or precipitation) over some given amount of time, typically on the scale of months to years. For the past several decades, environmental variables such as humidity, temperature and precipitation have been monitored more frequently than ever, making modern analyses of high-frequency (i.e. sub-annual, annual and interannual scale) climate variability geographically widespread and robust. Looking towards the future, scientists are interested in whether global warming is causing increased climate variability, partly characterized by more extreme weather events, and if so, how society will adapt to changing conditions (Huntingford et al., 2013; Karl et al., 1995). Addressing this problem not only requires an evaluation of conditions in a warming world, but a comprehensive understanding of high-frequency climate variability prior to anthropogenic interference.

The two primary barriers to creating this seamless record of past to present climate variability is the availability of high-resolution data and scale of interpretation (i.e. the interpretation of climate based on the range of frequencies analyzed). The issue of data resolution arises because some geologic records, such as ocean sediment and rock cores, cannot be sampled at sub-annual, interannual or even decadal resolution throughout the last glacial period and ice cores have only recently been resolved on these scales with CFA analysis (Jones, 2018a). Thus, a plethora of information exists surrounding centennial and millennial scale paleoclimate variability because lower resolution records are inherently representative of lower frequency events (Buizert et al., 2015b; Schulz et al., 2004). Additionally, because it is generally assumed that most paleoclimate records provide information on the millennial scale, it is not uncommon to find academic article titles missing a descriptor of the scale of climate variability analyzed, which we believe leads to misconceptions in climate science. In an extreme example, Rehfeld et al. 2018 provides evidence for a reduction in temperature variability by a factor of 73 from the LGP to the Holocene in Greenland but does not explicitly state the scale analyzed in the title, abstract or introduction. Further reading reveals quantification of variability was determined by calculating variance between the 500 and 1,750 year spectral periods. To the casual reader, this point may go unnoticed and conclusions could be reached that are not consistent with reality. Further, what the authors have done is calculate temperature variability that is largely skewed towards the background glacial climate state which, as stated previously, is characterized by large millennial-scale abrupt warmings known as DO Events. As we show in this study, the reduction in variability on interannual to decadal scales in northeast Greenland changes by only a factor of 4 in the temperature domain (or a factor of 2.5 in the isotope domain) from the LGP to the Holocene. This is significantly different than the factor of 73 given by Rehfeld et al., 2018 and highlights the importance of clearly indicating the scale of interpretation when analyzing climate variability of the past.

Even with high-resolution records, such as cm or mm resolved ice cores, the scale of interpretation is highly dependent on the methodologies used to quantify climate variability. For example, variability can be measured several ways, such as the relative magnitude of some signal, as we show in this study using spectral analysis, or as the relative dispersion of data using a moving standard deviation. Because climate operates on a continuum of frequency components, we argue that non-frequency dependent methodologies, such as the standard deviation, are problematic in that they unavoidably skew measurements of variability to the strongest resolvable frequencies in the data. The figures below outline a simple situation in which standard deviation and strength of signal are not interchangeable, and thus measuring variability using these two methodologies will result in two different interpretations of climate.

In Figure 4.1, we define a synthetic temperature signal comprised of four sinusoidal functions with frequencies of 1/4, 1/7, 1/10 and 1/100 year^{-1} and amplitudes of 7, 4, 10 and 30 °F, respectively. Here, centennial scale variability is strongest and overwhelms the higher frequency signals with lower amplitudes. When a non-frequency dependent measurement (i.e. standard deviation) of variability is calculated, we see that it is weighted towards the large amplitude of the sine wave with frequency of 1/100 year^{-1}. Thus, even though variability exists at higher frequencies, the standard deviation does not reliably represent the strength of that high-frequency climate variability. This thought experiment shows the importance of considering the strength of individual frequencies using spectral techniques, rather than considering the standard deviation of the full signal.

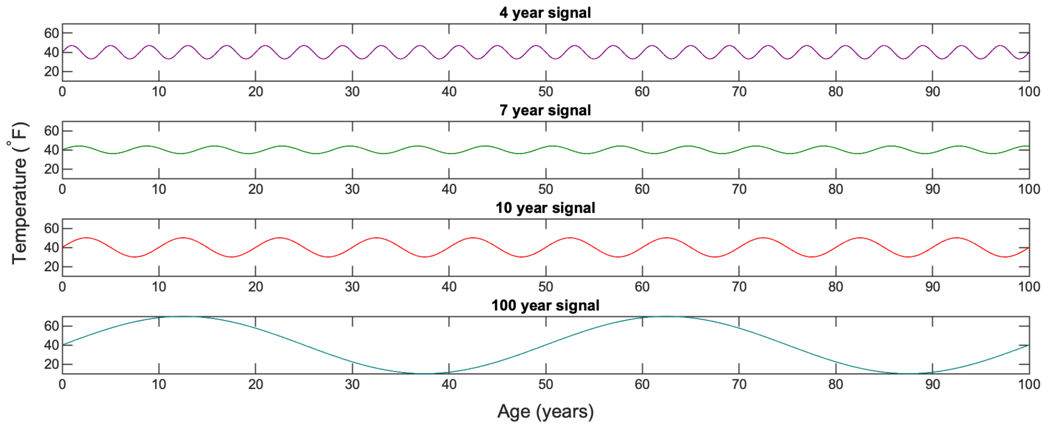

Figure 4.1: Four independent functions with frequencies of 1/4, 1/7, 1/10 and 1/100 year^{-1} and amplitudes of 7, 4, 10 and 30 °F, respectively

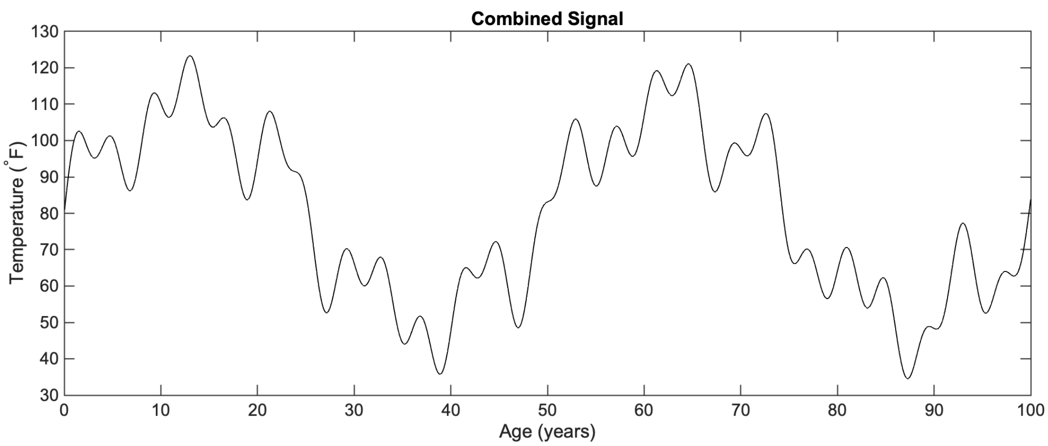

Figure 4.2: Synthetic temperature signal created by combining the four independent signals in Figure 4.1

	Amplitude (°F)	Standard Deviation (°F)
4 year signal	7	4.9
7 year signal	4	2.8
10 year signal	10	7.0
100 year signal	30	21.2
Combined signal	n/a	23.1

Table 4.1: Comparison of frequency dependant amplitude vs non-frequency dependant standard deviation for the signals in Figures 4.1-4.2

Similarly, we can show in Figure 4.3 that standard deviations of ice core water isotope data are not necessarily representative of the strength of high-frequency climate variability, as defined in this study. Here, we calculate the standard deviation of raw isotope data in 400 year windows with a timestep of 200 years and compare this to our calculations of relative amplitude for the 10-15 year band (which is analyzed with the same window size and timestep). While these metrics agree relatively well for EGRIP, albeit with some discrepancies at millennial scales, both WDC and SPC show broad disagreement. For this reason, the standard deviation is not reliable for interpretation of high-frequency climate variability in our records, even if the data set is resolved at annual, interannual or decadal scales.

The combination of CFA analysis of water isotopes and spectral analysis techniques used in this study effectively overcomes the issues outlined above by 1) capturing data on interannual and decadal scales, 2) disentangling a multitude of frequency components captured in the data set and 3) isolating the scale of climate variability most useful to current initiatives. From this, we create records of high-frequency climate variability in Greenland and Antarctica that can be used to benchmark existing general circulation models and improve future predictions of climate change at these locations.

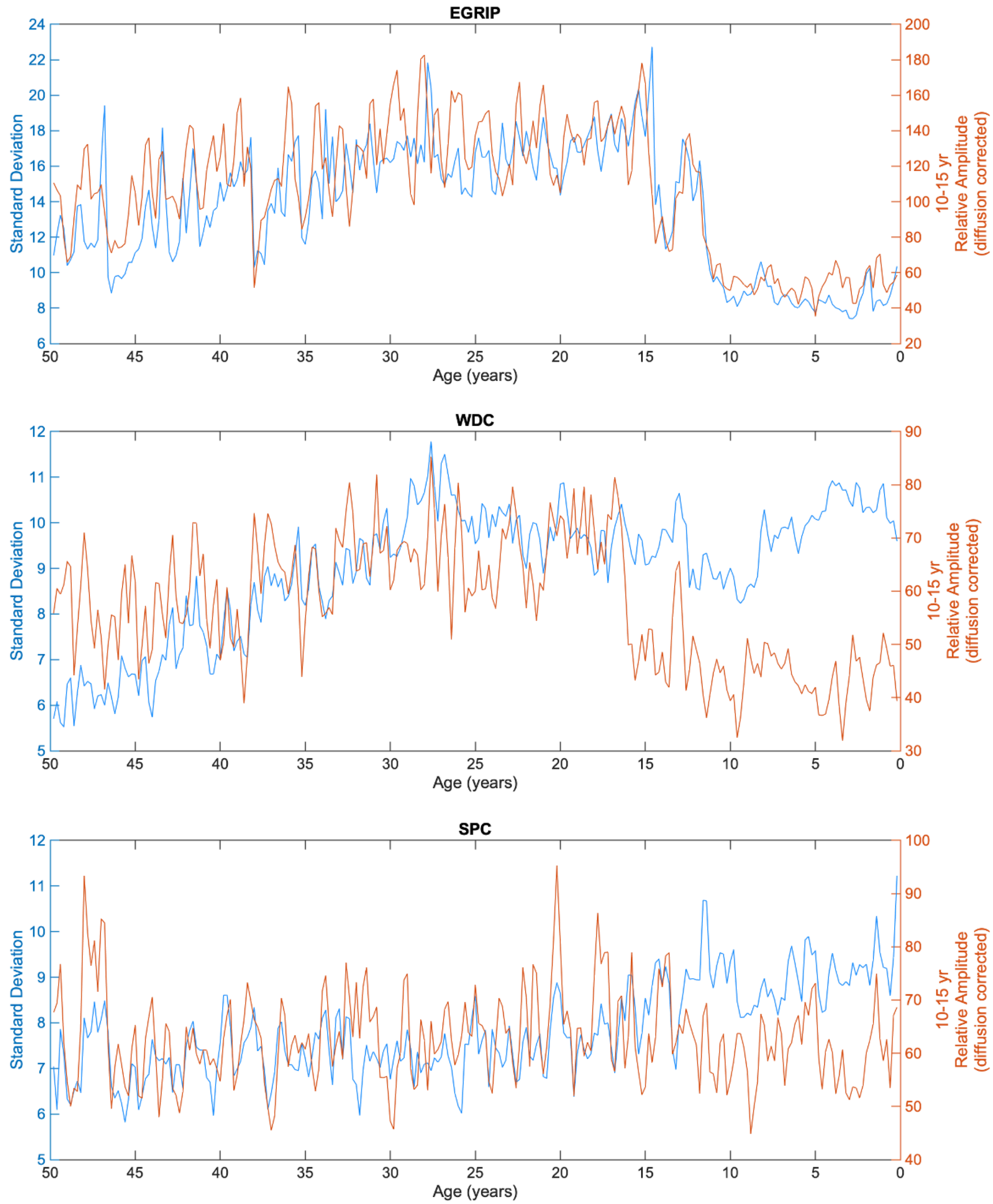

Figure 4.3: Standard deviation of raw δD record vs strength of decadal (i.e. 10-15 year band) climate variability for EGRIP, WDC, and SPC; analysis done in 400 year windows with a timestep of 200 years

4.2. Greenland

4.2.1. NGRIP vs EGRIP Sampling Resolution Comparison

The utility of temporally high-resolution data has been proven in recent studies (e.g. Jones et al. 2018, Jones et al. in review, 2021). In short, the ability to analyze interannual, annual, and seasonal climate variability is unlocking novel insights into the climate system and pushing the boundaries of our ability to reconstruct climate using global circulation models. In this thesis, we quantified the improvement in estimations of the amplitude of frequency bands (e.g. 10-15 yr variability) by comparing two records with different temporal sampling resolutions of 5 cm (NGRIP) and 1 mm (EGRIP). Glacial ice at EGRIP originates upstream of the current drilling camp near NGRIP, thus comparisons of frequency band amplitudes between the two cores tell us whether an artificial loss in amplitude for the 5 cm NGRIP record can skew results. Initially, we hypothesized that spectral analysis of the 5 cm resolution NGRIP water isotope record would result in underestimations of high frequency climate variability (i.e. in the 7-15 year bands where diffusion most strongly attenuates signals), especially further back in the record (e.g. at ages >30 ka bp) where annual layers in the ice have thinned substantially compared to younger ice.

We confirmed this hypothesis by comparing results from the original 1 mm EGRIP record to the original 5 cm NGRIP record. We found the 5 cm NGRIP record is compromised at ages greater than about 30 ka bp, resulting in lower estimates of frequency-band amplitudes than the mm-resolved EGRIP record. We further confirmed this to be true by also testing a 5 cm down-sampled EGRIP record; this test showed the same results (Figure 3.2). In effect, the lower sampling resolution at NGRIP tends to "cut-off" or "sample-across" the peaks and troughs of the record, artificially reducing the amplitudes of high-frequency signals. Because the EGRIP 1 mm sampling provides about 10 to 20 data points per year (depending on the extent of thinning), we can say that it is the first Greenland record capable of capturing uncompromised and continuous interannual and decadal climate variability well into the last glacial period (LGP). Using our results from EGRIP, we present preliminary hypotheses for the trends identified in traces of the amplitude of high-frequency climate variability and ultimately provide a road map for further research in the field of high-frequency polar climate variability modeling.

4.2.2. EGRIP Glacial-Interglacial Trends in Climate Variability

We find that northeastern Greenland, on average, experienced a 60% reduction in the strength of high-frequency climate variability (7-15 year band) from the Last Glacial Maximum (LGM; occurring from 16-27 ka bp and coinciding with the greatest extent and height of North American land ice during the LGP) to the Holocene (0-11 ka bp). Prior to the LGM (> 27 ka), the margin between glacial and Holocene climate variability was about 30% narrower. Because the topography of the Laurentide Ice Sheet (LIS; which covered present-day Canada and the northern USA) was highest during the LGM (~700 meters thick), we speculate that atmospheric circulation anomalies resulting from the presence of the LIS could be responsible for increased variability from 16-27 ka bp. There is already precedent for the LIS altering ocean-atmosphere circulation throughout the entire Pacific Basin, ranging from the Aleutian Low Pressure area in the North Pacific, to the tropical Pacific and as far away as West Antarctica (Jones e al., 2018). There is no reason to think the same did not occur, at least in part, in the North Atlantic Basin. Researchers in the modeling community are interested in this idea, but as of the writing of this thesis, no model runs have been published (Pers. Comm., Roberts, W.H.G., 2021). Although the field of high-frequency climate variability modeling is new and relatively incomplete, the results in the study offer a benchmark for future testing.

4.2.3. EGRIP Millennial-Scale (DO Event) Trends in Climate Variability

While long-term trends in the amplitude of high-frequency climate variability in northeast Greenland (on the order of 10 kyr or longer), or trends occurring across the last glacial-interglacial cycle, may have more to do with the topography of the Laurentide Ice Sheet (as discussed above), the multi-millennial trends in the glacial period occurring across Dansgaard-Oeschger cycles likely have a different set of forcing mechanisms. As a starting point, we initiated communication with climate scientist William H. G. Roberts (based in Northumbria, England) to discuss General Circulation Model (GCM) expectations. Existing HadCM3 model outputs, albeit older and unpublished as of the writing of this thesis, suggest northeast Greenland would exhibit decreased high-frequency climate variability during stadial (i.e. cold) periods, compared to interstadial (i.e. warm) periods, due to a lower latitude sea ice front pushing storm tracks further south and thus decreasing atmospheric circulation anomalies in the North Atlantic and in the vicinity of northeast Greenland (Pers. Comm., Roberts, W.H.G., 2021). In effect, the sea ice would act as a buffer for high-frequency variability. Our findings, that high-frequency climate variability was actually 50% stronger during stadial periods, is the opposite of the model expectation. This discrepancy shows that additional GCM runs are necessary to understand the forcing mechanisms and boundary conditions that could give rise to the empirical observations we present in this thesis.

Other model simulations are more in agreement with our findings. Maykut et al. (1971) finds that extensive sea ice acts as an insulating barrier between the ocean and atmosphere at high latitudes. In the absence of sea ice, the high heat capacity of the ocean effectively moderates ambient temperatures by providing a source of heat to the atmosphere. In other words, climates characterized by low sea ice extent experience less volatile temperature fluctuations, and vice versa. This line of thought can potentially be used to explain our results. The Last Glacial Period (LGP) was characterized by persistent sea ice coverage over the Arctic Ocean, while lower latitudes were subject to seasonal changes in sea ice. Reconstructions suggest that sea ice extended as far as 40° north along the coast of North America and to 55° north in the central and eastern Atlantic Ocean during the coldest times (Brennen et al., 2013). Thus, we know the sea ice extent on average extended to much lower latitudes during the glacial period as compared to the Holocene. We also have biomarker proxy evidence (Hoff et al. 2016) that suggests sea ice extended to much lower latitudes during cold stadial periods and retreated during warm interstadials. In a simplistic sense, this may account for our observations, in that removing the moderating effect of the ocean on atmospheric dynamics leads to greater temperature variability in cold stadial periods.

We also propose the idea that not only was sea ice more extensive, but that the sea ice front was more variable (i.e. moving north and south over many degrees of latitude from one year to the next) during stadial phases. This could occur due to increased solar radiation at lower latitudes driving a bimodal effect on the thin and fragile sea ice front where 1) growth occurs at colder, higher latitudes and 2) recession occurs in the presence of warmer, lower latitude temperatures. In theory, fluctuations in the sea ice front would also cause fluctuations in source-to-sink (i.e. evaporative source to precipitation site) temperature gradients, thus increasing variability in the isotopic signature of precipitation, as we find in this study. Although there are no proxy records capable of reconstructing sea ice variability on interannual to decadal scales, we suggest this scenario as a potential test in both temperature and isotope enabled GCMs. It is important to note that isotope variability, which we evaluate in this study, and local temperature variability at an ice core site may not be equivalent. For example, after calibrating a more variable sea ice front, a temperature enabled GCM may produce no changes in high-frequency variability during the LGP in Greenland, while an isotope enabled model produces the signal we describe in Section 3.1.6. This potential outcome may suggest that the trend we find (i.e. cold stadial periods exhibit greater variability) is largely a product of increased variability in source to sink temperature gradients of precipitation and water vapor (from the sea ice front moving more degrees of latitude in the north-south direction), despite temperature remaining relatively stable over EGRIP. This scenario would beg the question: at what scale (i.e. sub-annual, interannual, decadal, centennial, etc.) do isotope and temperature variability become decoupled in central Greenland? Further modeling research is required to answer this question.

To explain our observations, that temperature variability was larger during stadial periods at EGRIP, we hypothesize that 1) sea ice extended further south on average and 2) the sea ice extent experienced greater north-south variability from year-to-year during cold stadial periods. Either mechanism, or a combination of both, can in theory account for our observations. Yet, this scenario does not consider regional dynamics, such as atmospheric pressure anomalies, Rossby waves, or teleconnections, that may shift and change due to sea ice cover. Thus, new HadCM3 model runs are required to explicitly test sea ice extent and sea ice variability from year to year, under varying boundary conditions for orbital forcing, greenhouse gases, and ice sheet topography/albedo. It is also possible that new HadCM3 model runs will uncover other forcing mechanisms, for example, that connections to lower latitudes may be driving North Atlantic dynamics. As our observations are a first order discovery, a large amount of work is necessary to fully understand the results.

Even more interesting than stadial-interstadial comparisons is the temporal evolution of changes in high-frequency climate variability across Dansgaard-Oeschger (DO) warming events. From our high-resolution (i.e. 400 year window, 50 year timestep) evaluation of climate variability during the LGP, we find that on average variability decreases prior to abrupt DO warming by 0.5 - 1 ka bp. This information offers unprecedented insight into the forcing mechanisms of abrupt climate change that punctuated the LGP.

A simple, but incredibly useful framework for analyzing abrupt climate change, proposed by Alley et al., 2003, likens the climate system to an upright canoe. The climate system, as well as the canoe, will remain largely stable so long as no drastic changes are made. Despite this, both systems are capable of exhibiting threshold behavior, wherein reaching an adequate intensity of change results in a rapid transition to some new state. With this framework, abrupt change requires a trigger (or initial modification to the system), an amplifier (which intensifies the trigger and causes total change to cross some threshold), a globalizer (which spreads abrupt change across Earth) and finally a source of persistence (which holds the system in a new stable state). In the case of the upright canoe, a trigger could be someone leaning too far over the edge, while friction between the boat and the person acts as an amplifier. The canoe flipping with the person still inside acts a globalizer and finally, resistance of the canoe to being flipped back over would be the source of persistence.

Although applying this framework to the climate system is much less straightforward, it offers a useful starting point for testing preliminary hypotheses about what causes abrupt climate change. In terms of the Greenlandic abrupt climate change cycles, known as Dansgaard-Oeschger (DO) cycles, the most widely accepted hypotheses involve an amplifying bi-stability (i.e. fluctuation between weak and strong states) in the Atlantic Meridional Overturning Circulation (AMOC), potentially triggered by freshwater forcing from ice rafting events or increased precipitation (Ganopolski & Rahmstorf, 2001; Bond et al., 1999; Eisenmann et al., 2009). Despite significant efforts to bolster this theory, much uncertainty exists surrounding potential trigger mechanisms. For example, freshwater influx via large scale ice rafting events, known as Heinrich events, can only explain a fraction of the DO cycles observed in Greenland ice core water isotope records (Bond et al., 1993). For this reason, we propose an alternative framework for abrupt DO cycles, using evidence in this study, that builds upon a relatively new, but increasingly popular theory that rapid expansion and contraction of thick ice shelves and thin sea ice in the North Atlantic can explain the abrupt temperature shifts observed in DO cycles (Boers et al., 2018; Li et al., 2005; Petersen et al., 2013)

The model simulation in which our results agree the most (proposed by Boers et al., 2018) is as follows. Entering glacial conditions from the last interglacial period, North Atlantic (NA) ice shelf and sea ice extent are set to zero and AMOC is in a strong baseline state. As temperatures cool, NA ice cover gradually increases as an ice shelf forms off eastern Greenland. After a certain ice cover threshold is reached, an enhanced ice-albedo feedback causes sea ice to rapidly expand in the NA which in turn, creates an insulating barrier (as discussed in Maykut et al., 1971) between the ocean and atmosphere. The sea ice barrier traps oceanic heat brought north by a strong AMOC and warms NA subsurface water (T_{NAW}), preventing it from becoming dense and sinking. This weakens AMOC and eventually (i.e. several hundred years later) causes a gradual warming in the Southern Hemisphere. When T_{NAW} reaches a certain threshold, sea ice destabilizes and rapidly breaks apart and releases the buildup of oceanic heat to the atmosphere, rapidly increasing T_G. This abrupt change marks the onset of a Dansgaard-Oeschger (DO) cycle. Once subsurface waters cool considerably, AMOC switches back to a strong baseline state and the process starts over again.

The two-step structure of DO cooling back to stadial conditions in Boers et al. (2008) is explained by 1) a slow growing ice shelf off eastern Greenland in the first phase and 2) rapid sea ice expansion via positive feedback loops in the second phase. In our study, stadial periods are characterized by weak but relatively stable climate variability in the first phase (i.e. slow growing ice shelf formation) followed by an abrupt increase in high-frequency climate variability during and after the second phase (i.e. rapid sea ice expansion). We suggest that the rise in high-frequency variability around T_G (mean Greenlandic atmospheric temperature) during the second cooling phase can potentially be explained by 1) increased sea ice cover and 2) increased north-south variability in sea ice coverage. A combination of these two factors creates a vast and fluctuating sea ice cover during stadial periods that could in theory drive drastic fluctuations in source-to-sink (i.e. evaporative source to precipitation site) temperature gradients, which directly affect the isotopic signatures of precipitation.

However, we find a discrepancy in the timing between abrupt T_G warming at the onset of a DO event and the shift from strong to weak temperature variability during the ensuing interstadial period. The Boers model suggests that NH ice cover (i.e. sea ice and ice shelf cover) essentially disintegrates immediately at the onset of abrupt warming. This is somewhat consistent with Steffensen et al. (2008) which shows that abrupt change during the LGP occurred in just a few years using the NGRIP deuterium excess record, a proxy for Greenland moisture source. Conversely, we show that high-frequency climate variability in Greenland begins to decrease about 0.5-1 ka prior to abrupt warming and sea ice disintegration, creating an inconsistency between our hypothesis and the Boers model. It is possible that mean sea ice extent and sea ice variability become decoupled during this timeframe and that sea ice front variability (i.e. north-south movement over many degrees of latitude) acts as a primary driving mechanism for the results we present in this study. In this case, the model appropriately captures mean NA ice extent, but is unable to resolve decreasing high-frequency sea ice variability that potentially drives our signal. It is also possible that our results are forced by other factors, but additional studies would be required to disentangle such mechanisms.

Overall, our results lend evidence in support of the Boers et al. (2018) hypothesis that rapid expansion and contraction of thick ice shelves and thin sea ice in the North Atlantic can explain the rapid temperature shifts observed during the LGP in Greenland. If we apply this hypothesis to the Alley et al. (2003) framework for abrupt climate change, increasing North Atlantic subsurface water temperature (T_{NAW}) acts as a trigger for abrupt DO warming, a stark rebuttal to other leading theories that suggest DO cycles are triggered by freshwater forcing from land ice or precipitation. We support this theory with 1) evidence from Maykut et al. (1971) that extensive sea ice can cause more volatile atmospheric temperature fluctuations and 2) our own hypothesis that sea ice was increasingly variable at greater mean extents during the LGP, leading to more variable source-to-site temperature gradients in polar precipitation. The single caveat to our hypothesis is evidence to suggest sea ice variability and sea ice extent may have become decoupled 0.5 - 1 ka prior to abrupt DO warming. Further research will be required to understand forcing mechanisms for this discrepancy.

4.3. Antarctica

4.3.1. WDC and SPC Glacial-Interglacial Trends in Climate Variability

Prior high-resolution studies of West Antarctic climate (Jones et al., 2018) found a 50% reduction in the amplitude of interannual climate signals at 16.2 ka bp. This change was ultimately caused by an abrupt decrease in the size of the Laurentide ice sheet and subsequent shifts in Pacific Basin climate dynamics. In the modern, SPC and WDC share a common moisture source: the Pacific Basin (Sodemann and Stohl, 2009). Assuming this common dynamic held in the past, we initially hypothesized that the 16.2 ka signal present at WDC would also be evident at SPC, but significantly dampened because this area is far more isolated thus, fewer storm tracks would reach interior Antarctica.

While the magnitude of high-frequency climate variability is similar for WDC and SPC during the LGP, we found that the 16.2 ka signal at SPC is either not present or heavily masked by noise (see Figure 3.21). In the case that the 16.2 change is not present, this must mean climate dynamics between WDC and SPC were decoupled in the LGP. In the case that the 16.2 signal is simply overwhelmed by noise, then our initial hypothesis (that the signal would be evident at SPC, but significantly dampened due to the isolation from the moisture source) is supported. Delineating exact forcing mechanisms for these results is outside the scope of this study, but empirical evidence we provide can be used to benchmark existing general circulation models.

4.3.2. WDC and SPC Millennial-Scale (AIM Event) Trends in Climate Variability

While the topography of the Laurentide Ice Sheet may drive glacial-interglacial climate variability at both WDC and SPC, trends of high-frequency climate variability over millennial scale warming events known as Antarctic Isotope Maxima (AIM) events are likely forced by a different mechanism. We find that both Antarctic study sites, WDC and SPC, experience little to no change in the strength of high-frequency climate variability over the course of warm AIM and cold non-AIM periods. This is intriguing in that mean Antarctic temperature changes substantially (1-3 degrees C; Pedro et al., 2018) during these transitions but high-frequency variability around the mean does not.

We hypothesize that more oceanic stability in the Southern Ocean (SO), compared to the North Atlantic, during the LGP could explain our results. Recent studies provide evidence that the strength and mean position of the Antarctic Circumpolar Current (ACC), which flows clockwise between 45° and 55° around Antarctic, was either unchanged (Matsumoto et al., 2001) or stronger (Mazaud et al., 2010) during the Last Glacial Period, compared to modern day. The ACC is driven by prevailing westerly winds and transports approximately 130 million Sv (m^3 s^{-1}) of deep, intermediate and surface water between the three ocean basins (e.g. Indian, Atlantic and Pacific) that surround Antarctica (Rintoul et al., 2001). We hypothesize consistent strength in the ACC potentially hindered the formation of sea ice to lower latitudes in the Southern Ocean during the LGP, thus decreasing 1) mean sea ice extent and 2) high-frequency sea ice variability around the mean.

Reconstructions of mean sea ice extent in the Southern Ocean during the Last Glacial Period (LGP) may support this hypothesis. Collins et al. (2011) found that the Antarctic winter sea ice front, at its maximum extent, reached approximately 53° S (only a 3° advance from its modern limit) between 23.5-25 ka bp and that the summer sea ice front reached as far as 55° S (or a 12° advance from its modern limit) sometime between 23.5-30 ka bp. With this, the spatial difference between winter and summer sea ice extents, referred to as the seasonal sea-ice zone, was substantially smaller during the LGP than in the Holocene. These findings are relatively in line with Allen et al. (2011) and CLIMAP Project Members (1976, 1981) although others (Gersonde et al., 2004) argue these reconstructions overestimate summer sea ice extents. It is possible that a combination of strong westerly winds and a powerful Antarctic Circumpolar Current (ACC) hindered ultra-extensive sea ice formation around Antarctica during the LGP, especially during cold winter periods, thus creating a more stable sea ice cover and reducing the seasonal sea-ice zone. Our results, that WDC and SPC exhibit consistent high-frequency climate variability during the LGP despite millennial scale changes in mean temperature, could possibly be explained by a less extensive and relatively stable sea ice cover (compared to the North Atlantic during the LGP) that 1) moderates atmospheric temperature fluctuations and 2) reduces variability in source-to-sink (i.e. evaporative source to precipitation site) temperature gradients which directly affect the isotopic signatures used in this study.

One caveat is that the Collins et al. (2011) reconstructed maximums were determined to pre-date the Last Glacial Maximum, but it is unclear whether these extents persisted throughout the timeframe (i.e. 30-50 ka bp) of our millennial scale (AIM event) high-frequency analysis. As mentioned in Section 4.2.3, there are no proxy records capable of accurately reconstructing sea ice variability on interannual to decadal scales, but we find it reasonable to test our hypothesis in a general circulation model (GCM) by altering sea ice boundary conditions in the Southern Ocean during the LGP.

4.4. Interhemispheric Comparisons

4.4.1. Glacial-Interglacial Trends in Climate Variability

Prior to obtaining results, our simple null hypothesis was that EGRIP and WDC would experience comparable strengths in high-frequency climate variability during the LGP and

Holocene due to their similar latitudinal positioning. Using the line of thought that SPC variability would be slightly dampened (discussed in Section 4.3.1) compared to WDC, we also initially hypothesized that EGRIP would have slightly greater variability than SPC throughout the past 50 ka.

We disproved these null hypotheses, finding that in the isotope domain EGRIP exhibits high-frequency climate variability about twice the magnitude of WDC and SPC during the LGP. In the temperature domain, this translates to 4.5 greater high-frequency variability at EGRIP during the LGP. Due to a substantial knowledge gap in high-frequency climate variability modeling, we can only suggest potential explanations for these results. We hypothesize the topography of the Laurentide Ice Sheet is (LIS) imparted atmospheric anomalies on all three sites during the LGP, but the magnitude and occurrence of anomalies was greatest at EGRIP, perhaps due to its proximity to the LIS, and weakest at SPC due to the isolated nature of this site.

We know from Jones et al. (2018) that during the Last Glacial Maximum (LGM), the LIS imparted greater high-frequency variability on WDC through increased teleconnection between the tropical Pacific Basin and West Antarctica. We conclude this effect is only vaguely evident in the SPC record due to the geographic separation between this site and the oceanic processes of West Antarctica. Model testing is required to confirm or refute this hypothesis. On the contrary, we hypothesize that the LIS greatly affected climate dynamics at EGRIP by imparting a physical (e.g. 700 meters tall) barrier to atmospheric circulation that may have driven increased atmospheric anomalies in the nearby North Atlantic Basin. This hypothesis also requires model testing but proposes a starting point for future high-frequency variability research focused on the LGM.

4.4.2. Millennial-Scale Trends in Climate Variability

We observe significant differences between Greenland and Antarctic trends of high-frequency climate variability across millennial scale temperature shifts that punctuated the LGP. At EGRIP, cold stadial periods exhibit approximately 50% greater variability than warm interstadial phases and at WDC and SPC, there is no discernable difference in the strength of variability between warm AIM phases and the cold non-AIM counterparts. This trend is summed up well by Figure 3.31. We hypothesize different geographies surrounding Greenland and Antarctica ultimately cause these distinct trends in isotopic variability during the LGP by controlling the capacity for sea ice to expand and retract.

As discussed in Section 4.3.2, the Antarctic Circumpolar Current (ACC) is driven by prevailing westerly winds at approximately 50° S. Westerly winds are substantially stronger in the Southern Hemisphere, compared to the Northern Hemisphere, because there are few physical barriers, such as continents, that can interrupt the flow of air. The result is a steady and strong oceanic current that transports water at most depths and effectively creates a barrier between warm water at mid latitudes and cold water at southern high latitudes. We hypothesize this phenomenon may have hindered extensive sea ice cover during cold phases of the LGP (e.g. maximum extent at 53° S), thus reducing the seasonal sea ice zone. The could in theory explain the stable strength of high-frequency climate variability at WDC and SPC that we observe across AIM Events during the LGP.

In contrast, the North Atlantic Ocean, which is surrounded by land, experiences reduced wind and less oceanic turbulence relative to the South Ocean. We hypothesize this characteristic allowed sea ice to 1) grow to much lower latitudes (i.e. maximum extent at 40° S) during cold phases of the LGP and 2) fluctuate more in the presence of warm, lower latitude temperatures, thus imparting increased variability on source-to-sink temperature gradients and the magnitude of atmospheric temperature fluctuations. Together, these factors may explain our observations of unstable high-frequency isotopic variability in northeastern Greenland across DO cycles.

Chapter 5: CONCLUSION

In this study, we provide the first reconstruction of high-frequency (i.e. interannual to decadal scale) climate variability in Greenland throughout the past 50 thousand years. We focus on trends across long wavelength transitions, such as glacial-interglacial shifts and millennial scale Dansgaard-Oeschger cycles during the Last Glacial Period (LGP). We find that on average, the LGP exhibits 2.5 times greater variability than the Holocene and within the context of the LGP, cold stadial periods are 1.5 times more variable than warm interstadial periods. In essence, interannual and decadal climate variability in Greenland is highly sensitive to shifts in mean temperature (see Figure 3.31). These results offer unprecedented insight into Northern Hemisphere climate dynamics and can be used to benchmark existing general circulation models (GCMs). We also provide two key modeling questions to test. Did the topography of the Laurentide Ice Sheet increase mean isotopic variability in northeast Greenland during the Last Glacial Maximum (LGM) as compared to the Holocene via atmospheric anomalies in the North Atlantic? Additionally, could an extensive and fluctuating sea ice cover surrounding Greenland during the LGP impart greater interannual and decadal variability in the isotopic signature of precipitation across DO Events?

Another pivotal result in this study is that both Antarctic sites (WDC and SPC) exhibit no change in high-frequency climate variability across millennial-scale warm Antarctic Isotope Maxima (AIM) phases, in stark contrast to the Northern Hemisphere results. From this, we propose the question to modelers: Could a less extensive and more stable sea ice cover surrounding Antarctica during the LGP result in consistent interannual and decadal climate variability across AIM Events despite significant changes in mean temperature?

With this study, we hope to motivate GCM research that answers our questions about high-frequency climate variability and the mechanisms that result in such distinct interhemispheric trends. Targeted sea ice models may assist in this endeavor by clarifying the relationship between mean sea ice extent and variability of the sea ice front on interannual and decadal scales throughout different climate states in the Northern and Southern Hemispheres. Another useful tool may be evaluating high-resolution sea salt sodium records from coastal ice cores as a proxy for sea ice extent and decadal variability (Rankin et al., 2002; Rhodes et al., 2018). If it is determined that our hypotheses about sea ice are incorrect, then modeling efforts should focus on teleconnection mechanisms as a potential cause of our observed trends in high-frequency climate variability. It is also possible that the cause is something we have not thought of and in that case, we must let science take its course.

Looking forward, we suggest analysis of high-resolution water isotope records from geographically diverse regions of Greenland and Antarctica to further investigate how latitude or proximity to oceanic processes affects high-frequency climate variability in polar regions. Three future projects may provide this insight include the upcoming Hercules Dome ice core project in East Antarctica, the South Dome ice core in south Greenland and mm-scale resampling of the GISP2 ice core which is stored at the National Science Foundation Ice Core Facility (NSF-ICF).

BIBLIOGRAPHY

Allen, C. S., Pike, J., & Pudsey, C. J. (2011). Last glacial–interglacial sea-ice cover in the SW Atlantic and its potential role in global deglaciation. *Quaternary Science Reviews*, *30*(19), 2446–2458. https://doi.org/10.1016/j.quascirev.2011.04.002

Alley, R., Marotzke, J., Nordhaus, W., Overpeck, J., Peteet, D., Pielke Sr, R., Pierrehumbert, R., Rhines, P., Stocker, T., Talley, L., & Wallace, J. (2003). Abrupt Climate Change. *Science (New York, N.Y.)*, *299*, 2005–2010. https://doi.org/10.1126/science.1081056

Álvarez-Solas, J., Montoya, M., Ritz, C., Ramstein, G., Charbit, S., Dumas, C., Nisancioglu, K., Dokken, T., & Ganopolski, A. (2011). Heinrich event 1: An example of dynamical ice-sheet reaction to oceanic changes. *Climate of the Past*, *7*(4), 1297–1306. https://doi.org/10.5194/cp-7-1297-2011

Blunier, T., & Brook, E. J. (2001). Timing of Millennial-Scale Climate Change in Antarctica and Greenland During the Last Glacial Period. *Science*, *291*(5501), 109–112. https://doi.org/10.1126/science.291.5501.109

Boers, N., Ghil, M., & Rousseau, D.-D. (2018). Ocean circulation, ice shelf, and sea ice interactions explain Dansgaard–Oeschger cycles. *Proceedings of the National Academy of Sciences*, *115*(47), E11005–E11014. https://doi.org/10.1073/pnas.1802573115

Bond, G., Broecker, W., Johnsen, S., McManus, J., Labeyrie, L., Jouzel, J., & Bonani, G. (1993). Correlations between climate records from North Atlantic sediments and Greenland ice. *Nature*, *365*(6442), 143–147. https://doi.org/10.1038/365143a0

Bond, G. C., Showers, W., Elliot, M., Evans, M., Lotti, R., Hajdas, I., Bonani, G., & Johnson, S. (1999). The North Atlantic's 1-2 Kyr Climate Rhythm: Relation to Heinrich Events, Dansgaard/Oeschger Cycles and the Little Ice Age. In *Mechanisms of Global Climate Change at Millennial Time Scales* (pp. 35–58). American Geophysical Union (AGU). https://doi.org/10.1029/GM112p0035

Brennan, C. E., Meissner, K. J., Eby, M., Hillaire-Marcel, C., & Weaver, A. J. (2013). Impact of sea ice variability on the oxygen isotope content of seawater under glacial and interglacial conditions. *Paleoceanography*, *28*(3), 388–400. https://doi.org/10.1002/palo.20036

Buis, A. (2020, February 27). *Milankovitch (Orbital) Cycles and Their Role in Earth's Climate*. Climate Change: Vital Signs of the Planet. https://climate.nasa.gov/news/2948/milankovitch-orbital-cycles-and-their-role-in-earths-climate

Buizert, C., Adrian, B., Ahn, J., Albert, M., Alley, R. B., Baggenstos, D., Bauska, T. K., Bay, R. C., Bencivengo, B. B., Bentley, C. R., Brook, E. J., Chellman, N. J., Clow, G. D., Cole-Dai, J., Conway, H., Cravens, E., Cuffey, K. M., Dunbar, N. W., Edwards, J. S., … WAIS

Divide Project Members. (2015). Precise interpolar phasing of abrupt climate change during the last ice age. *Nature*, *520*(7549), 661–665. https://doi.org/10.1038/nature14401

Buizert, C., Cuffey, K. M., Severinghaus, J. P., Baggenstos, D., Fudge, T. J., Steig, E. J., Markle, B. R., Winstrup, M., Rhodes, R. H., Brook, E. J., Sowers, T. A., Clow, G. D., Cheng, H., Edwards, R. L., Sigl, M., McConnell, J. R., & Taylor, K. C. (2015, February 5). *The WAIS Divide deep ice core WD2014 chronology – Part 1: Methane synchronization (68–31 kaBP) and the gas age–ice age difference*. Copernicus Publications.

Busek, P., Vanková, J., Opavsky, J., Salinger, J., & Nevsimalova, S. (2005). Spectral analysis of heart rate variability in sleep. *Physiological Research / Academia Scientiarum Bohemoslovaca*, *54*, 369–376

Choi, J.-G., Olsen, M. D., Kwansa, F. A., & Tse, E. C.-Y. (1999). Forecasting industry turning points: The US hotel industry cycle model. *International Journal of Hospitality Management*, *18*(2), 159–170. https://doi.org/10.1016/S0278-4319(99)00011-0

CLIMAP Project Members (1976), The surface of the Ice-age Earth, Science, 191, 1131–1137, doi:10.1126/science.191.4232.1131.

CLIMAP Project Members (1981), Seasonal reconstruction of the Earth's surface at the last glacial maximum, http://www.ncdc.noaa.gov/paleo/ metadata/noaa-ocean-2516.html, World Data Cent of Paleoclimatology, Boulder, Colo.

Cohen, H., Kotler, M., Matar, M. A., Kaplan, Z., Miodownik, H., & Cassuto, Y. (1997). Power spectral analysis of heart rate variability in posttraumatic stress disorder patients. *Biological Psychiatry*, *41*(5), 627–629. https://doi.org/10.1016/S0006-3223(96)00525-2

Collins, L. G., Pike, J., Allen, C. S., & Hodgson, D. A. (2012). High-resolution reconstruction of southwest Atlantic sea-ice and its role in the carbon cycle during marine isotope stages 3 and 2. *Paleoceanography*, *27*(3). https://doi.org/10.1029/2011PA002264

Cuffey, K. M., Clow, G. D., Steig, E. J., Buizert, C., Fudge, T. J., Koutnik, M., Waddington, E. D., Alley, R. B., & Severinghaus, J. P. (2016). Deglacial temperature history of West Antarctica. *Proceedings of the National Academy of Sciences*, *113*(50), 14249–14254. https://doi.org/10.1073/pnas.1609132113

Dansgaard, W. (1964). Stable isotopes in precipitation. *Tellus*, *16*(4), 436–468. https://doi.org/10.1111/j.2153-3490.1964.tb00181.x

Dansgaard, W., Johnsen, S. J., Moller, J., & Langway, C. C. (1969). One Thousand Centuries of Climatic Record from Camp Century on the Greenland Ice Sheet. *Science*, *166*(3903), 377–380. https://doi.org/10.1126/science.166.3903.377

Dasgupta, A., & Wahed, A. (2014). Chapter 4—Laboratory Statistics and Quality Control. In A. Dasgupta & A. Wahed (Eds.), *Clinical Chemistry, Immunology and Laboratory Quality Control* (pp. 47–66). Elsevier. https://doi.org/10.1016/B978-0-12-407821-5.00004-8

Ditlevsen, P. D., Andersen, K. K., & Svensson, A. (2007). The DO-climate events are probably noise induced: Statistical investigation of the claimed 1470 years cycle. *Climate of the Past*, *3*(1), 129–134. https://doi.org/10.5194/cp-3-129-2007

Eisenman, I., Bitz, C. M., & Tziperman, E. (2009). Rain driven by receding ice sheets as a cause of past climate change: RAIN AS A CAUSE OF CLIMATE CHANGE. *Paleoceanography*, *24*(4). https://doi.org/10.1029/2009PA001778

EPICA Community Members. (2006). One-to-one coupling of glacial climate variability in Greenland and Antarctica. *Nature*, *444*(7116), 195–198. https://doi.org/10.1038/nature05301

Galewsky, J., Steen-Larsen, H. C., Field, R. D., Worden, J., Risi, C., & Schneider, M. (2016). Stable isotopes in atmospheric water vapor and applications to the hydrologic cycle. *Reviews of Geophysics*, *54*(4), 809–865. https://doi.org/10.1002/2015RG000512

Ganopolski, A., & Rahmstorf, S. (2001). Rapid changes of glacial climate simulated in a coupled climate model. *Nature*, *409*(6817), 153–158. https://doi.org/10.1038/35051500

Gat, J. (1996). Oxygen and hydrogen isotopes in the hydrologic cycle. *Annual Review of Earth and Planetary Sciences*, *24*, 225–262. https://doi.org/10.1146/annurev.earth.24.1.225

Gersonde, R., Crosta, X., Abelmann, A., & Armand, L. (2005). Sea-surface temperature and sea ice distribution of the Southern Ocean at the EPILOG Last Glacial Maximum—A circum-Antarctic view based on siliceous microfossil records. *Quaternary Science Reviews*, *24*(7), 869–896. https://doi.org/10.1016/j.quascirev.2004.07.015

Grootes, P. M., & Stuiver, M. (1997). Oxygen 18/16 variability in Greenland snow and ice with 10−3- to 105-year time resolution. *Journal of Geophysical Research: Oceans*, *102*(C12), 26455–26470. https://doi.org/10.1029/97JC00880

Hoff, U., Rasmussen, T. L., Stein, R., Ezat, M. M., & Fahl, K. (2016). Sea ice and millennial-scale climate variability in the Nordic seas 90 kyr ago to present. *Nature Communications*, *7*(1), 12247. https://doi.org/10.1038/ncomms12247

Hughes, A. G., Jones, T. R., Vinther, B. M., Gkinis, V., Stevens, C. M., Morris, V., Vaughn, B. H., Holme, C., Markle, B. R., & White, J. W. C. (2020). High-frequency climate variability in the Holocene from a coastal-dome ice core in east-central Greenland. *Climate of the Past*, *16*(4), 1369–1386. https://doi.org/10.5194/cp-16-1369-2020

Huntingford, C., Jones, P., Livina, V., Lenton, T., & Cox, P. (2013). No increase in global temperature variability despite changing regional patterns. *Nature*, *500*. https://doi.org/10.1038/nature12310

Huybers, P. (2021). pmtmPH.m (https://www.mathworks.com/matlabcentral/fileexchange/2927-pmtmph-m), MATLAB Central File Exchange. Retrieved April 13, 2021.

Johnsen, S., Clausen, H. B., Cuffey, K. M., Schwander, J., & Creyts, T. (2000). Diffusion of stable isotopes in polar firn and ice: The isotope effect in firn diffusion. *Physics of Ice Core Records*, 121–140.

Johnsen, S. J., Clausen, H. B., Dansgaard, W., Gundestrup, N. S., Hammer, C. U., Andersen, U., Andersen, K. K., Hvidberg, C. S., Dahl-Jensen, D., Steffensen, J. P., Shoji, H., Sveinbjörnsdóttir, Á. E., White, J., Jouzel, J., & Fisher, D. (1997). The δ18O record along the Greenland Ice Core Project deep ice core and the problem of possible Eemian climatic instability. *Journal of Geophysical Research: Oceans*, *102*(C12), 26397–26410. https://doi.org/10.1029/97JC00167

Johnsen, S. J., Dansgaard, W., Clausen, H. B., & Langway, C. C. (1972). Oxygen Isotope Profiles through the Antarctic and Greenland Ice Sheets. *Nature*, *235*(5339), 429–434. https://doi.org/10.1038/235429a0

Jones, T. R., Cuffey, K. M., White, J. W. C., Steig, E. J., Buizert, C., Markle, B. R., McConnell, J. R., & Sigl, M. (2017). Water isotope diffusion in the WAIS Divide ice core during the Holocene and last glacial. *Journal of Geophysical Research: Earth Surface*, *122*(1), 290–309. https://doi.org/10.1002/2016JF003938

Jones, T. R., Roberts, W. H. G., Steig, E. J., Cuffey, K. M., Markle, B. R., & White, J. W. C. (2018). Southern Hemisphere climate variability forced by Northern Hemisphere ice-sheet topography. *Nature*, *554*(7692), 351–355. https://doi.org/10.1038/nature24669

Jones, T. R., White, J. W. C., Steig, E. J., Vaughn, B. H., Morris, V., Gkinis, V., Markle, B. R., & Schoenemann, S. W. (2017). Improved methodologies for continuous-flow analysis of stable water isotopes in ice cores. *Atmospheric Measurement Techniques*, *10*(2), 617–632. https://doi.org/10.5194/amt-10-617-2017

Jouzel, J., Alley, R. B., Cuffey, K. M., Dansgaard, W., Grootes, P., Hoffmann, G., Johnsen, S. J., Koster, R. D., Peel, D., Shuman, C. A., Stievenard, M., Stuiver, M., & White, J. (1997). Validity of the temperature reconstruction from water isotopes in ice cores. *Journal of Geophysical Research: Oceans*, *102*(C12), 26471–26487. https://doi.org/10.1029/97JC01283

Kahle, E. C., (in review), "Reconstruction of Temperature, Accumulation Rate, and Layer Thinning from an Ice Core at South Pole Using a Statistical Inverse Method", *Journal of Geophysical Research*

Kahle, E. C., Holme, C., Jones, T. R., Gkinis, V., & Steig, E. J. (2018). A Generalized Approach to Estimating Diffusion Length of Stable Water Isotopes From Ice-Core Data. *Journal of Geophysical Research: Earth Surface*, *123*(10), 2377–2391. https://doi.org/10.1029/2018JF004764

Karl, T. R., Knight, R. W., & Plummer, N. (1995). Trends in high-frequency climate variability in the twentieth century. *Nature*, *377*(6546), 217–220. https://doi.org/10.1038/377217a0

Kendall, C., & Caldwell, E. A. (1998). *Fundamentals of isotope geochemistry*. 51–86. https://doi.org/10.1016/B978-0-444-81546-0.50009-4

Kindler, P., Guillevic, M., Baumgartner, M., Schwander, J., Landais, A., & Leuenberger, M. (2014). Temperature reconstruction from 10 to 120 kyr b2k from the NGRIP ice core. *Climate of the Past*, *10*, 887–902. https://doi.org/10.5194/cp-10-887-2014

Li, C., Battisti, D. S., Schrag, D. P., & Tziperman, E. (2005). Abrupt climate shifts in Greenland due to displacements of the sea ice edge: GREENLAND CLIMATE SHIFTS AND SEA ICE. *Geophysical Research Letters*, *32*(19), n/a-n/a. https://doi.org/10.1029/2005GL023492

Lorius, C., Merlivat, L., Jouzel, J., & Pourchet, M. (1979). A 30,000-yr isotope climatic record from Antarctic ice. *Nature*, *280*(5724), 644–648. https://doi.org/10.1038/280644a0

Markle, B. R., & Steig, E. J.,. "Improving temperature reconstructions from ice-core water-isotope records." Climate of the Past Discussions (2021): 1-70.

Matsumoto, K., Lynch-Stieglitz, J., & Anderson, R. F. (2001). Similar glacial and Holocene Southern Ocean hydrography. *Paleoceanography*, *16*(5), 445–454. https://doi.org/10.1029/2000PA000549

Maykut, G. A., & Untersteiner, N. (1971). Some results from a time-dependent thermodynamic model of sea ice. *Journal of Geophysical Research (1896-1977)*, *76*(6), 1550–1575. https://doi.org/10.1029/JC076i006p01550

Mazaud, A., Michel, E., Dewilde, F., & Turon, J. L. (2010). Variations of the Antarctic Circumpolar Current intensity during the past 500 ka: ACC VARIATIONS DURING THE PAST 500 KA. *Geochemistry, Geophysics, Geosystems*, *11*(8), n/a-n/a. https://doi.org/10.1029/2010GC003033

Mojtabavi, S., Wilhelms, F., Cook, E., Davies, S., Sinnl, G., Skov Jensen, M., Dahl-Jensen, D., Svensson, A., Vinther, B., Kipfstuhl, S., Jones, G., Karlsson, N. B., Faria, S. H., Gkinis, V., Kjær, H., Erhardt, T., Berben, S. M. P., Nisancioglu, K. H., Koldtoft, I., & Rasmussen, S. O. (2019). *A first chronology for the East Greenland Ice-core Project (EGRIP) over the Holocene and last glacial termination* [Preprint]. Proxy Use-Development-Validation/Ice Cores/Holocene. https://doi.org/10.5194/cp-2019-143

Pedro, J. B., Jochum, M., Buizert, C., He, F., Barker, S., & Rasmussen, S. O. (2018). Beyond the bipolar seesaw: Toward a process understanding of interhemispheric coupling. *Quaternary Science Reviews*, *192*, 27–46. https://doi.org/10.1016/j.quascirev.2018.05.005

Petersen, S. V., Schrag, D. P., & Clark, P. U. (2013). A new mechanism for Dansgaard-Oeschger cycles. *Paleoceanography*, *28*(1), 24–30. https://doi.org/10.1029/2012PA002364

Petit, J. R., Jouzel, J., Raynaud, D., Barkov, N. I., Barnola, J.-M., Basile, I., Bender, M., Chappellaz, J., Davis, M., Delaygue, G., Delmotte, M., Kotlyakov, V. M., Legrand, M., Lipenkov, V. Y., Lorius, C., PÉpin, L., Ritz, C., Saltzman, E., & Stievenard, M. (1999). Climate and atmospheric history of the past 420,000 years from the Vostok ice core, Antarctica. *Nature*, *399*(6735), 429–436. https://doi.org/10.1038/20859

Steffensen JP, Andersen KK, Bigler M, Clausen HB, Dahl-Jensen D, Fischer H, Goto-Azuma K, Hansson M, Johnsen SJ, Jouzel J, Masson-Delmotte V, Popp T, Rasmussen SO, Röthlisberger R, Ruth U, Stauffer B, Siggaard-Andersen ML, Sveinbjörnsdóttir AE, Svensson A, White JW. High-resolution Greenland ice core data show abrupt climate change happens in few years. Science. 2008 Aug 1;321(5889):680-4. doi: 10.1126/science.1157707. Epub 2008 Jun 19. PMID: 18566247.

Rankin, A. M., Wolff, E. W., & Martin, S. (2002). Frost flowers: Implications for tropospheric chemistry and ice core interpretation. *Journal of Geophysical Research: Atmospheres*, *107*(D23), AAC 4-1-AAC 4-15. https://doi.org/10.1029/2002JD002492

Rasmussen, S. O., Bigler, M., Blockley, S. P., Blunier, T., Buchardt, S. L., Clausen, H. B., Cvijanovic, I., Dahl-Jensen, D., Johnsen, S. J., Fischer, H., Gkinis, V., Guillevic, M., Hoek, W. Z., Lowe, J. J., Pedro, J. B., Popp, T., Seierstad, I. K., Steffensen, J. P., Svensson, A. M., … Winstrup, M. (2014). A stratigraphic framework for abrupt climatic changes during the Last Glacial period based on three synchronized Greenland ice-core records: Refining and extending the INTIMATE event stratigraphy. *Quaternary Science Reviews*, *106*, 14–28. https://doi.org/10.1016/j.quascirev.2014.09.007

Rayner, J. N. (2001). Spectral Analysis. In N. J. Smelser & P. B. Baltes (Eds.), *International Encyclopedia of the Social & Behavioral Sciences* (pp. 14861–14864). Pergamon. https://doi.org/10.1016/B0-08-043076-7/02514-6

Rehfeld, K., Münch, T., Ho, S. L., & Laepple, T. (2018). Global patterns of declining temperature variability from the Last Glacial Maximum to the Holocene. *Nature, 554*(7692), 356–359. https://doi.org/10.1038/nature25454

Rhodes, R. H., Yang, X., & Wolff, E. W. (2018). Sea Ice Versus Storms: What Controls Sea Salt in Arctic Ice Cores? *Geophysical Research Letters*, *45*(11), 5572–5580. https://doi.org/10.1029/2018GL077403

Rintoul, S. R., & Sokolov, S. (2001). Baroclinic transport variability of the Antarctic Circumpolar Current south of Australia (WOCE repeat section SR3). *Journal of Geophysical Research: Oceans*, *106*(C2), 2815–2832. https://doi.org/10.1029/2000JC900107

Schulz, M. (2002). On the 1470-year pacing of Dansgaard-Oeschger warm events. *Paleoceanography*, *17*(2), 4-1-4–9. https://doi.org/10.1029/2000PA000571

Schulz, M., Paul, A., & Timmermann, A. (2004). Glacial–interglacial contrast in climate variability at centennial-to-millennial timescales: Observations and conceptual model. *Quaternary Science Reviews*, *23*(20), 2219–2230. https://doi.org/10.1016/j.quascirev.2004.08.014

Sigl, M., Fudge, T. J., Winstrup, M., Cole-Dai, J., Ferris, D., McConnell, J. R., Taylor, K. C., Welten, K. C., Woodruff, T. E., Adolphi, F., Bisiaux, M., Brook, E. J., Buizert, C., Caffee, M. W., Dunbar, N. W., Edwards, R., Geng, L., Iverson, N., Koffman, B., … Sowers, T. A. (2016). The WAIS Divide deep ice core WD2014 chronology – Part 2: Annual-layer counting (0–31 ka BP). *Climate of the Past*, *12*(3), 769–786. https://doi.org/10.5194/cp-12-769-2016

Sjolte, J., Hoffmann, G., Johnsen, S. J., Vinther, B. M., Masson-Delmotte, V., & Sturm, C. (2011). Modeling the water isotopes in Greenland precipitation 1959–2001 with the meso-scale model REMO-iso. *Journal of Geophysical Research: Atmospheres*, *116*(D18). https://doi.org/10.1029/2010JD015287

Sodemann, H., & Stohl, A. (2009). Asymmetries in the moisture origin of Antarctic precipitation. *Geophysical Research Letters*, *36*(22). https://doi.org/10.1029/2009GL040242

Steffensen, J. P., Andersen, K. K., Bigler, M., Clausen, H. B., Dahl-Jensen, D., Fischer, H., Goto-Azuma, K., Hansson, M., Johnsen, S. J., Jouzel, J., Masson-Delmotte, V., Popp, T., Rasmussen, S. O., Röthlisberger, R., Ruth, U., Stauffer, B., Siggaard-Andersen, M.-L., Sveinbjörnsdóttir, Á. E., Svensson, A., & White, J. W. C. (2008). High-Resolution Greenland Ice Core Data Show Abrupt Climate Change Happens in Few Years. *Science*, *321*(5889), 680–684. https://doi.org/10.1126/science.1157707

Svensson, A., Andersen, K. K., Bigler, M., Clausen, H. B., Dahl-Jensen, D., Davies, S. M., Johnsen, S. J., Muscheler, R., Parrenin, F., Rasmussen, S. O., Rothlisberger, R., Seierstad, I., Steffensen, J. P., & Vinther, B. M. (2008). A 60 000 year Greenland stratigraphic ice core chronology. *Clim. Past*, 11.

Veres, D., Bazin, L., Landais, A., Toyé Mahamadou Kele, H., Lemieux-Dudon, B., Parrenin, F., Martinerie, P., Blayo, E., Blunier, T., Capron, E., Chappellaz, J., Rasmussen, S. O., Severi, M., Svensson, A., Vinther, B., & Wolff, E. W. (2013). The Antarctic ice core chronology (AICC2012): An optimized multi-parameter and multi-site dating approach for the last 120 thousand years. *Climate of the Past*, *9*(4), 1733–1748. https://doi.org/10.5194/cp-9-1733-2013

WAIS Divide Project Members. (2015). Precise interpolar phasing of abrupt climate change during the last ice age. *Nature*, *520*(7549), 661–665. https://doi.org/10.1038/nature14401

Whillans, I. M., & Grootes, P. M. (1985). Isotopic diffusion in cold snow and firn. *Journal of Geophysical Research: Atmospheres*, *90*(D2), 3910–3918. https://doi.org/10.1029/JD090iD02p03910

White, W. M. (2012). *Isotope Geochemistry Chapter 8: Stable Isotope Theory*.

Wilson, P., & Okunev, J. (1999). Spectral analysis of real estate and financial assets markets. *Journal of Property Investment & Finance*, *17*(1), 61–74. https://doi.org/10.1108/14635789910252909

Winski, D. A., Fudge, T. J., Ferris, D. G., Osterberg, E. C., Fegyveresi, J. M., Cole-Dai, J., Thundercloud, Z., Cox, T. S., Kreutz, K. J., Ortman, N., Buizert, C., Epifanio, J., Brook, E. J., Beaudette, R., Severinghaus, J., Sowers, T., Steig, E. J., Kahle, E. C., Jones, R., … McConnell, J. R. (2019). The SP19 chronology for the South Pole Ice Core – Part 1: Volcanic matching and annual layer counting. *Clim. Past*, 16.

Wolff, E. W., Chappellaz, J., Blunier, T., Rasmussen, S. O., & Svensson, A. (2010). Millennial-scale variability during the last glacial: The ice core record. *Quaternary Science Reviews*, *29*(21), 2828–2838. https://doi.org/10.1016/j.quascirev.2009.10.013

Yeragani, V. K., Pohl, R., Berger, R., Balon, R., Ramesh, C., Glitz, D., Srinivasan, K., & Weinberg, P. (1993). Decreased heart rate variability in panic disorder patients: A study of power-spectral analysis of heart rate. *Psychiatry Research*, *46*(1), 89–103. https://doi.org/10.1016/0165-1781(93)90011-5

Zhang, X., Knorr, G., Lohmann, G., & Barker, S. (2017). Abrupt North Atlantic circulation changes in response to gradual CO2 forcing in a glacial climate state. *Nature Geoscience*, *10*(7), 518–523. https://doi.org/10.1038/ngeo2974

Zhang, X., Lohmann, G., Knorr, G., & Purcell, C. (2014). Abrupt glacial climate shifts controlled by ice sheet changes. *Nature*, *512*(7514), 290–294. https://doi.org/10.1038/nature13592